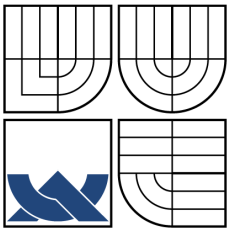

VYSOKÉ UČENÍ TECHNICKÉ V BRNĚ
BRNO UNIVERSITY OF TECHNOLOGY

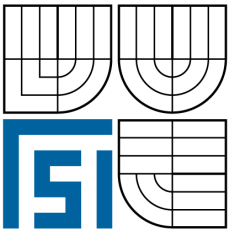

FAKULTA STROJNÍHO INŽENÝRSTVÍ
ÚSTAV FYZIKÁLNÍHO INŽENÝRSTVÍ
FACULTY OF MECHANICAL ENGINEERING
INSTITUTE OF PHYSICAL ENGINEERING

COULOMB INTERACTIONS IN ELECTRON BEAMS IN THE VICINITY OF A SCHOTTKY AND COLD FIELD SOURCE

COULOMBOVSKÉ INTERAKCE ELEKTRONŮ V BLÍZKOSTI SCHOTTKYHO A STUDENÉ KATODY

DIZERTAČNÍ PRÁCE
DOCTORAL THESIS

AUTOR PRÁCE
AUTHOR
Ing. IVO LIŠKA

VEDOUCÍ PRÁCE
SUPERVISOR
prof. RNDr. BOHUMILA LENCOVÁ, CSc.

BRNO 2010

Abstrakt
Dizertační práce se zabývá problematikou výpočtu vlivu coulombovských interakcí částic na parametry emitovaného elektronového svazku v blízkosti Schottkyho a studené katody. Práce poskytuje základní předhled o problematice, popisuje vytvořené modely emisních zdrojů a metodu simulace Monte Carlo. Představuje novou metodu generování vstupních dat, která klade větší důraz na přesnou simulaci emisního procesu. Pozornost je zde věnována zejména vlivu interakcí na energiovou šířku, velikost virtuálního zdroje a jas katody v závislosti na velikosti poloměru hrotu a emisním proudu. Sledováním vývoje energiové šířky bylo zjištěno, že naprostá většina interakcí se odehrává v prostoru do několika mikrometrů od hrotu katody. Závislost spočtené celkové energiové šířky na úhlové intenzitě je ve shodě s dostupnými experimentálními daty. Spočtené energiové rozšíření vlivem coulombovských interakcí bylo srovnáno s hodnotami vypočtenými pomocí vzorců založených na analytických přiblíženích. Bylo zjištěno, že některé z nich přijatelně předpovídají trendy ale nemohou být použity pro kvantitativní odhad.

Abstract
This thesis deals with the effects of the coulomb interactions in the vicinity of the Schottky and the cold field electron source. It provides a basic overview about the subject describes Monte Carlo simulation method and used emitter models. A new method for generating initial particle conditions has been developed, which respects in more detail than usually the physical emission process. Especially the effects of the mutual interactions on energy width, size of the virtual source and brightness in dependence on the tip radius and the angular intensity were investigated. The evolution of the energy width in the emitter region showed that the absolute majority of interactions take place within first few micrometer. The dependence of the calculated total energy width on the angular intensity was compared with available experimental data, showing a good agreement. The calculated contribution of the interaction effects to the energy width was compared with predictions based on analytical approximations. It has been shown that some of them predict reasonably the tendencies but cannot be used for quantitative estimations.

Klíčová slova
coulombovské interakce, Monte Carlo simulace, elektronová tryska, schottky emise, autoemise, energiová šířka, virtuální zdroj, jas

Keywords
Coulomb interactions, Monte Carlo simulation, Electron Gun, Schottky emission, Field emission, ZrO, energy spread, virtual source, brightness

LIŠKA, I., *Coulomb interactions in electron beamsin the vicinity of a Schottky and cold field source*, Brno, Vysoké učení technické v Brně, Fakulta strojního inženýrství, 2010, 80 s., Vedoucí prof. RNDr. Bohumila Lencová, CSc.

Prohlašuji, že jsem předloženou dizertační práci vypracoval samostatně za odborného vedení prof. RNDr. Bohumily Lencové, CSc. Dále prohlašuji, že veškeré podklady, ze kterých jsem čerpal, jsou uvedeny v seznamu použité literatury.

Ing. Ivo Liška

Na tomto místě bych rád poděkoval prof. RNDr. Bohumile Lencové, CSc., za odborné vedení a trpělivost, Dr. Pavlu Adamcovi, za četné náměty a rady během mého doktorského studia bez kterých by tato práce nikdy nevznikla, Dr. Helmutu Banzhofovi, Ing. Jakubu Zlámalovi, Ph.D. a Ing. Tomáši Radličkovi, Ph.D., za pomoc se simulačními výpočty. Dále všem kolegům z ÚFI cenné rady a za pomoc při řešení administrativních problémů. Velký dík patří hlavně mé rodině za jejich podporu a trpělivost.

Ing. Ivo Liška

Contents

1 Introduction

Charged particle beams are used in almost every segment of scientific research and modern industry. A wide spectrum of electron and ion beam devices is used in many specialized applications. Probably the most widely used device of this kind is an electron microscope. The history of electron microscopy began with the invention of the first device by E. Ruska and Max Knoll in 1932. In almost 80 years of research and development the number of practical applications has grown and the performance of this highly versatile tool improved dramatically. The size of studied objects is commonly few nanometers. Using high energies and special techniques also single atoms and molecules are visible. In some aspects are present-day devices working near their physical limits. Nevertheless, by optimizing the design or using new technologies and materials, the performance can be still improved.

For the electron microscopy is one of the most challenging technological segments the semiconductor industry. The development of devices utilizing charged particle optics is driven primarily by growing demands on their precision, speed, stability and reliability. Neither actual nor on-coming sub-micron manufacturing technologies would be possible without continuous innovation and performance improvements.

Recent trend towards high beam currents allows a higher throughput in electron-beam metrology and defect review. In this way the productivity can be increased and costs considerably reduced. The resolution is not the most important parameter anymore, as it practically was in the past decades. Also in other applications of charged particle beams like the material analysis by Auger electron spectroscopy (AES) and focused ion beam micro-machining (FIB) are higher beam currents necessary, although rather for technological reasons. To provide the beam with more current and conserving other important parameters, electron sources with higher brightness are required.

In systems like the scanning electron microscope (SEM) or the scanning ion microscopes is chromatic aberration the main limiting factor for the resolution. The total energy spread of the beam is hence a critical parameter for the performance of the device. Practically every electron-optical component of the column is contributing to the final energy spread of the beam in some way. Starting with the source, having some initial energy width, and following by subsequent beam-forming components like limiting apertures, electrostatic and magnetic lenses, deflectors, aberration correctors, filters or monochromator. The contribution of the column optics to the energy broadening can be significantly reduced by appropriate design [1]. The intrinsic energy spread of the emission source itself is a property of the emission surface, operational temperature and applied extraction field. Additional broadening is caused by coulomb interaction among emitted electrons that depends strongly on beam current density. Reducing the energy spread of the emission source is therefore a difficult task.

The effects of coulomb interactions were studied extensively. Although some theoretical work exists, see e.g. Kruit and Jansen [1], Hawkes and Kasper [2] and a lot of experimental work and Monte Carlo simulations were published, there still remain issues where further work needs to be done. Because of high complexity of the problem, analytical approximations in source region have not been derived yet [3], at least for electrons. Existing attempts are based on a large number of simplification which results into relations valid only for various special cases. A detailed Monte Carlo simulation seems to be the most suitable

evaluation method presently. The coulomb interactions in currently popular liquid metal ion sources were already successfully simulated by Radlička and Lencová [4] and expected results were achieved. There is no similar detailed Monte Carlo simulation of interactions in the source region for Schottky (TFE) or cold field (CFE) emitters, which are probably the most frequently used electron sources in today's high-tech industrial and scientific electron microscopes. This work is hence focused on those emitter types. At the beginning an evaluation of the Schottky emitter only was intended. Due to initial problems with accuracy of the simulation software an error analysis of an analytical model of the emitter was necessary. The analytical model was later used for subsidiary simulation of the cold field emitter.

Following chapter presents the actual state of the subject. Individual sections are devoted to brief description of standard TFE and CFE emitter, to the relevant basics of theory of electron emission from metals and to a brief overview of present analytical models for the evaluation of coulomb interactions effects. The numerical approach and available software tools are here also discussed. In Chapter 3 the main objectives of this thesis are defined. Chapter 4 presents software tools used in the simulations. The concrete emitter models and various procedures of initial data preparation and output data processing are presented. The simulation results are analyzed and discussed in Chapter 4.2.

2 The state of the art

Electron emission source is naturally a key component of every electron optical device. Generally two basic principles of electron emission are utilized in sources intended for charged particle optics. These are the thermionic and the field emission. Modern emitters are taking advantage of their combination. The selection of a suitable emitter with some specific properties depends on application requirements.

2.1 Schottky and cold field emission electron source

Conventional electron sources like emitters based on simple tungsten filament or lanthanum hexaboride (LaB_6) single-crystal are utilizing purely or for the most part the thermionic emission. They provide reasonable currents but suffer from broad energy spread caused by high operational temperature. Their brightness is relatively low due to large emission area or diameter of the subsequent beam crossover. Sources, where high extraction field strongly enhances the emission process, are characterized by smaller tip radii and in principle do not need such a high working temperatures. These advantages are naturally reflected in the source performance. For applications where low intrinsic energy width and high brightness is required, the thermal field Schottky emitter (TFE) or the cold field emitter (CFE) are the preferred choice.

2.2 Mechanical arrangement and basic operational parameters

A common Schottky emitter (fig. 1) is composed of a $\langle 100 \rangle$ oriented tungsten single-crystal wire spot welded to a heating filament. The filament is attached to two robust contact pins on a cylindrical ceramic base. The tip of the emitter (fig. 2) is electrochemically etched to a radius in the range of 0.2 - 2 μm. Bigger tip radii can be prepared using local Joule heat method [5]. At the shank of the tip is deposited a reservoir of zirconium oxide (ZrO).

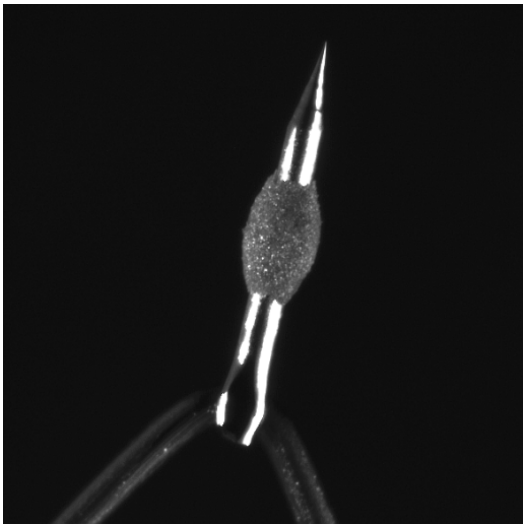

Figure 1: Schottky emitter. Field of view is about 1.25 mm

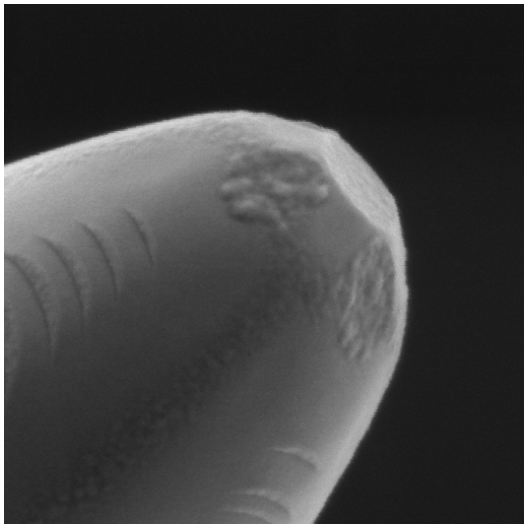

Figure 2: SEM image of the emitter apex. Field of view is 1.45 μm.

Presented images of the emitter were taken by myself using light and electron microscope in the laboratory at the site of my employer, Applied Materials - ICT GmbH.

In order to achieve an electron emission from the tip, the emitter has to be heated by current in the heating filament. The typical operational temperature of the Schottky cathode is 1800K and required heating current about 2.3 A for a tip with 0.5μm radius. Strong extraction field in the range $10^7 - 10^8$ V/m combined with a relatively high operating temperature allows a material relaxation on the apex of the tip where in optimal case a stable flat facet grows after short processing. The higher temperature also ensures a continuous diffusion of zirconium oxide to the facet where an adsorbed layer lowers the work function approximately from 4.6 to 2.8eV. This effects are very important for bright and stable emission and long lifetime of the source.

Electrons emitted from the tip surface are immediately accelerated in the direction of the first positively biased electrode (extractor) with opening about 0.4mm. Their trajectories are formed by the effect of strong extraction field into a narrow beam with half-angle about 7° [11]. The tungsten wire is usually surrounded with a suppressor, which has with respect to the cathode a slightly negative voltage. The purpose of this electrode is to suppress undesired thermionic emission from the surface of the emitter behind the apex. The protrusion of the tip is about 250μm. The mechanical arrangement and the number of electrodes surrounding the source can vary for different types of emitters. The configuration used for the Schottky emitter is generally called a triode gun. A schematic of the arrangement is in the Figure 3a.

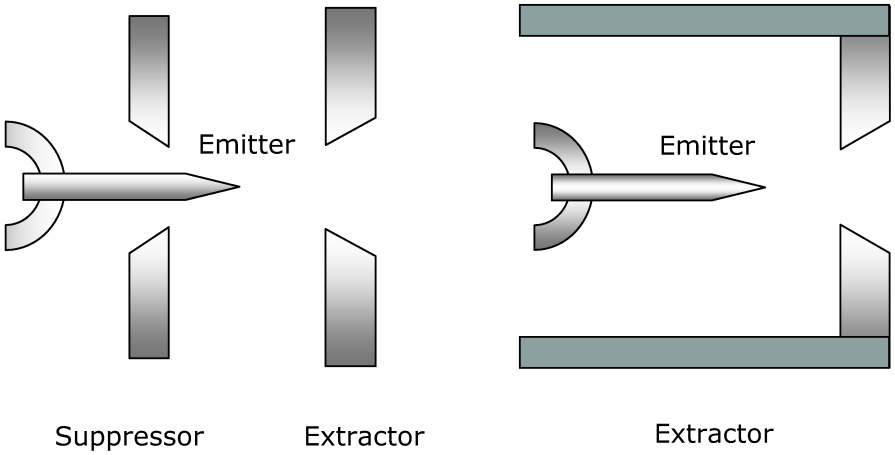

(a) Triode gun (b) Diode gun

Figure 3: Common electron gun arrangements

Total emission current of the source is usually less than 300μA. The current from the flat facet and the closest surrounding area reaches few micro-Ampere. For practical purposes is an angular intensity parameter of more interest. Typical working point of the Schottky emitter is in the range 100 - 300 μA/sr. Subsequent optics does not use the whole beam for imaging. In order to reduce the effects of source aberrations, at some distance after the plane of the extraction electrode is the beam diameter reduced by a limiting aperture.

The mechanical arrangement of cold field emitter is similar to the Schottky cathode, but it slightly differs in several points. The tungsten wire used for the tip has mostly $\langle 310 \rangle$ or $\langle 111 \rangle$ crystallographic orientation. Although these planes have a relatively high work function, no activation by supporting materials like oxygen or the zirconium oxide in the case of the Schottky emitter is used. The apex radius (fig. 4) is in the range of 50 - 200 nm. A moderate electrostatic field on the extraction electrode and the small apex radius are sufficient conditions for field emission.

Whereas the Schottky source is always used in triode configuration, the CFE in principle does not need the suppressor electrode and may be operated in so called diode configuration. A schematic of the arrangement is in the Figure 3b.

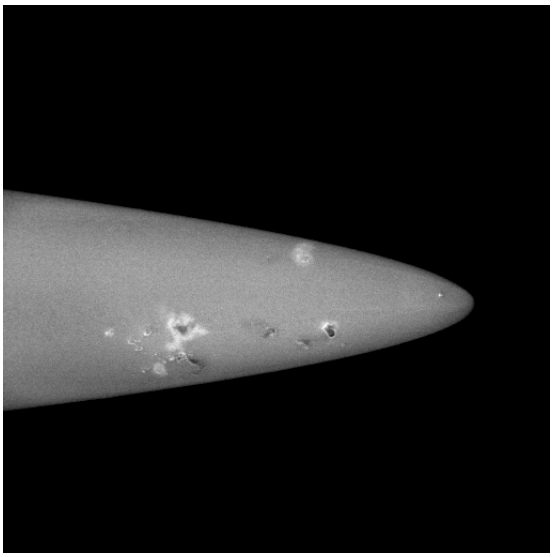

Figure 4: Tip of the cold field emitter. The image was taken before the emission process.

In principle, no additional heating of the cathode is required and the cathode can be operated at the room temperature. Unfortunately the emission current is significantly less stable compared to Schottky emitter. The very small apex radius means small emission area, which results in high sensitivity of emission process to changes in composition of atomic layers, material impurities or contamination on the emitter surface. In order to keep the emission current as stable as possible, the required vacuum background has to be at very good level (below 1×10^{-10}Torr, depending on requested emission stability) and cathode needs to be frequently flashed. To fulfill such a condition is not an easy task. The pressure level in the required range is largely dominated by the electron stimulated desorption (ESD) caused by illumination of the extractor and the anode surface by the beam emitted from the cathode. The level of the ESD cannot be effectively reduced by the baking of the vacuum system, as the thermal energy is too low to desorb chemically adsorbed species. Therefore it is necessary to desorb the critical surfaces by ESD before the normal operation of the gun. Unfortunately, the electron beam is not very effective in the desorption of this kind of contamination and the cleaning process can take very long time, e.g. several days to few weeks. We suggested in [13] a method of pre-cleaning of electron-optical parts with surfaces exposed to the electron beam during the gun operation.

Most important differences in the performance between Schottky emitter and CFE are following: Due to a smaller virtual source size CFE offers higher brightness, according to Schwind et al. [16] approximately an order of magnitude larger than Schottky emitter. On the other hand small apex area results in high emission noise. The absence of additional heating slightly lowers the energy spread to about 0.2eV; however, the sensitivity of the emission to surface contamination of the tip increases significantly vacuum requirements. Typical level of vacuum background for Schottky emitter is $p < 1 \times 10^{-8}$Torr or better. The CFE emitter needs at least $p < 1 \times 10^{-10}$Torr and has to be frequently flashed. The lifetime of Schottky cathode is under regular working conditions in average 2 years. The lifetime of the field emitter is practically unlimited until the tip is destroyed by an arc or due to improper operation. The table 1 summarizes the most important parameters. The description of this type of emitter as a "cold field emitter" is generally established but not completely correct. This type of emitter is because of its non-zero operational temperature (300K) described within the emission theory as a thermal-field emitter.

A comprehensive overview [10, 11, 8] and comparison between Schottky and CFE cathode can be found in a review paper [16].

Mode	$T(K)$	$\phi(eV)$	$I'(\mu A/sr)$	$a(nm)$	V	$F(V/nm)$	$J(A/m^2)$	m	$FW50$	$d_v(nm)$	$B_r(A/m^2srV)$
CFE	300	4.30	62	175	4300	4.33	1.8×10^9	0.50	0.27	4.0	1.14×10^9
SE	1800	2.79	500	550	5459	0.65	3.2×10^7	0.18	0.5	28	1.47×10^8

Table 1: Comparison of typical operating parameters according Schwind et al. (2006)[16].

2.3 Basic theory of emission from metals

The theory of emission from metal surfaces is complex. Like other rather complicated theories it introduces a number of simplifications and assumptions. The basic one in this scope is a free-electron approximation known as the Sommerfeld model [2] derived by Sommerfeld and Bethe in 1933. It assumes among others no band structure in the bulk metal, a finite potential barrier at the surface and the Fermi-Dirac distribution for electron energies E at temperature $T > 0$. The distribution is given by:

$$f(E,T) = \left[1 + \exp\left(\frac{E - E_F}{kT}\right)\right]^{-1}, \tag{1}$$

where E_F is a Fermi level and k Boltzmans's constant.

The whole emission process is influenced by many parameters and cannot be therefore described with one simple analytical expression. Most important (and freely adjustable) quantities are the temperature (T) and the field on the emitter surface (F). With respect to the T/F ratio is the spontaneous emission process divided into few categories. The thermionic emission (TE), the field emission (FE or TFE) and transitions between them (Schottky and extended Schottky emission). The principal differences among them can be better understood from the simple schematic in the Figure 5.

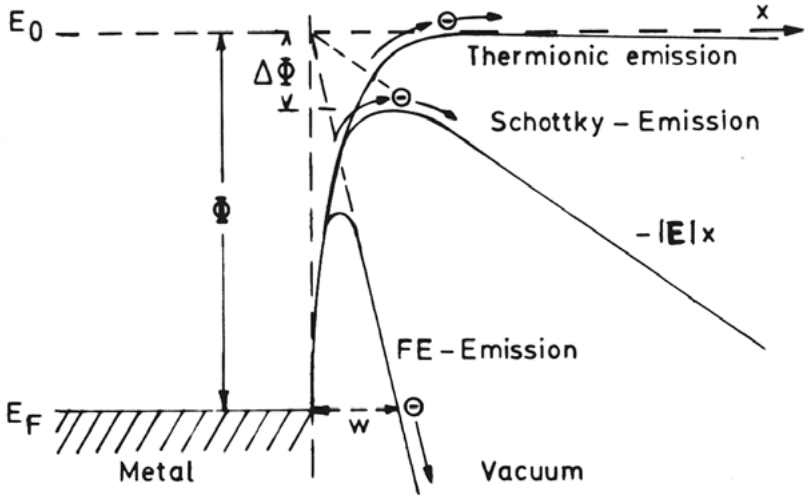

Figure 5: Emission model [18]

The hatched area on the left side are energy levels in the metal. At $T = 0$ electrons have energies only up to E_F level. On the right side is a vacuum potential E_0. In the case of *thermionic emission* (high temperature - low field) only electrons which are thermally excited according to Fermi-Dirac distribution have enough energy. They are able to overcome the potential barrier and leave the surface. The following equations are for the most part derived and in detail described in [2].

In the case of the thermionic emission can be the barrier defined by simple step function as follows:

$$V(z) = \begin{cases} -(E_F + \phi) & \text{for } z < 0, \\ 0 & \text{for } z \geq 0, \end{cases} , \tag{2}$$

where ϕ is the work function. The value of the work function is a characteristic material property and represents a minimum energy needed for relocation of an electron from the material to outside.

From the simulation point of view is the first important information provided by the theory of emission the relation for calculation of current density on the surface of the emitter. The saturated current density for thermionic emission is given by the well known Richardson-Duschman equation:

$$j_T = \frac{4\pi me}{h^3}(kT^2) \exp\left(-\frac{\phi}{kT}\right). \tag{3}$$

Knowing the field and appropriate current density distribution at the surface of the emitter, the starting positions of the electrons can be calculated. Their angular distribution follows in the case of the thermionic emission known Lambert's cosine law:

$$\tilde{B}(\gamma) := \frac{1}{\pi} j_T \cos\gamma. \tag{4}$$

Another important information is the total energy distribution. With the help of this function initial energies of emitted electron can be generated. By the means of the distribution function an intrinsic energy width is given. The total energy distribution for the thermionic emission is given by:

$$dj_T(E) = \frac{4\pi me}{h^3} E \exp\left(-\frac{E + \phi}{kT}\right) dE. \tag{5}$$

The work function $\phi = E_0 - E_F$ can be significantly lowered by application of some suitable surface layer (e.g. ZrO) or also by application of electrostatic field to the cathode surface. The second possibility is known as the Schottky effect and the emission process, where the effect is involved, is called the *Schottky emission*. The potential barrier lowered by the effect of electrostatic field is defined as:

$$V(z) = \begin{cases} 0 & \text{for } z < 0, \\ \phi - eFz - e^2/16\pi\varepsilon_0 z & \text{for } z \geq 0, \end{cases} \tag{6}$$

where F is the field on the surface and z is the position on axis normal to the surface. As a reference point for the energy is taken the Fermi level E_f. The position of the top of the barrier is then calculated from:

$$z_m = \sqrt{\frac{e}{16\pi\varepsilon_0 F}}, \tag{7}$$

The emission current density for Schottky emission given by:

$$j_S = j_T \ \exp\left(\frac{\Delta\phi}{kT}\right), \tag{8}$$

where j_T is the thermionic current density mentioned above and $\Delta\phi$ gives the difference between the work function and the maximum of the lowered barrier:

$$\Delta\phi = \sqrt{\frac{e^3 F}{4\pi\varepsilon_0}}. \tag{9}$$

The respective total energy distribution function is:

$$dj_S(E) = \frac{4\pi me}{h^3} E \exp\left(-\frac{E + V_m}{kT}\right) dE, \tag{10}$$

with the potential at the top of the barrier V_m defined as :

$$V_m = V(z_m) = \phi - \Delta\phi. \tag{11}$$

If a very strong field is applied to the surface, the potential barrier is not only lower but also thinner. At the top, where the barrier is thin enough, the quantum mechanical tunneling occurs. The emission process making use of this tunneling effect is described as *Extended Schottky emission*. A precise analytical representation of the barrier is not trivial and an approximation function is used. The barrier is approximated with second order polynomial [2]:

$$V(z) \approx V_m - \frac{e^2}{16\pi\varepsilon_0 z_m^3}(z - z_m)^2. \tag{12}$$

The current density for extended Schottky mode is given by:

$$j_{ES} = j_S \ \frac{\sin \pi q}{\pi q}, \tag{13}$$

where j_{ES} is the Schottky current density given by eq.(8) and the parameter q is:

$$q = \frac{c}{kT} \qquad \text{and } c \text{ is} \qquad c = \frac{\hbar}{\pi\sqrt{m}} \left(4\pi\varepsilon_0 F^3\right)^{\frac{1}{3}}. \tag{14}$$

The total energy distribution of the extended Schottky emission model is given by eq.(30) in [10]:

$$dj_{ES}(E) = \frac{4\pi me}{h^3} \frac{\kappa}{1 + \exp\left(\frac{E+\phi-\Delta\phi}{kT}\right)} ln\left[1 + \exp\left(\frac{E}{\kappa}\right)\right] dE, \tag{15}$$

where the parameter κ is:

$$\kappa = cF^{\frac{3}{4}}. \tag{16}$$

The respective origin of the energy scale is in this case set to the top of the potential barrier. The appropriate angular emission distribution is also affected by strong extraction field. The distribution function for the extended Schottky model given by eq.(44.35) in [2]:

$$R(\vartheta) = j_T \frac{(E_F - E)}{\pi d} cos(\vartheta) \cdot \exp\left[-\frac{(E_F - E) sin^2(\vartheta)}{d}\right], \tag{17}$$

where ϑ is the polar angle and E is the energy of the particle.

The last case is the *thermal-field emission*, which occurs at elevated temperature and high field on the emitter surface. Under these conditions the thermal excitation of electrons is very low and electrons are escaping from a metal only by the quantum mechanical tunneling through the field thinned barrier. The respective current density can be calculated with formula known as Murphy-Good equation:

$$j_{TF} = j_F \, \frac{\sin \pi p}{\pi p}, \tag{18}$$

where j_F is also known Fowler-Nordheim equation for field emission at T=0:

$$j_F = \frac{4\pi me}{h^3} d^2 \exp\left(b\frac{\phi}{d}\right). \tag{19}$$

The last term in the eq.(18) represents a contribution of the tunneling process to the total emission. The parameter p is defined as $p = kT/b$, with b given by:

$$b := \frac{2v(y_0)}{3t(y_0)} \qquad \text{and} \qquad d := \frac{e\hbar F}{2t(y_0)\sqrt{2m\phi}} = \frac{1}{2}eF. \tag{20}$$

The special field emission functions $v(y)$ and $t(y)$ contains complex elliptic integrals. They have been earlier tabulated by Good and Müller [19], but they can be also calculated using approximate formulas published in Kasper and Hawkes[2]:

$$v(y) = 1 - y^{1.69}, \quad t(y) = 1 + 0.1107y^{1.33}, \tag{21}$$

or using approximations published by Forbes [20]:

$$v(f) \approx 1 - f + \frac{1}{6} f \ln f \qquad \text{and} \qquad t(y) \approx 1 + \frac{1}{9}\left(y^2 - y^2 \ln y\right), \tag{22}$$

with $f = y^2 = F/F_b$, where F_b is the field needed to suppress the barrier of unreduced high to zero:

$$F_b = \frac{4\pi\varepsilon_0 h^2}{e^3}. \tag{23}$$

The variable y_0 needed in equations (20) is defined by:

$$y_0 = \frac{\Delta\phi}{\phi}. \tag{24}$$

And finally the total energy distribution for the field emission model:

$$dj_{TF}(E) = \frac{4\pi me}{h^3} \, d \, \exp\left(\frac{b\phi}{d}\right) \frac{\exp(E/d)}{1 + \exp(E/d)} dE. \tag{25}$$

The above mentioned equations are not covering all combinations of temperature, field and work function. A complete analytical theory unfortunately does not exist. Especially current densities j_{SE} and j_{TF} are accurate enough only for small values of q and p (in eq.(13) and (18)) up to the value of 0.7. If the parameter q exceeds this limit, the current density should be calculated numerically following the procedure in [32]. According to very recent overview [11], the accuracy of the analytical equation (13) is in question already for q >0.3.

2.4 Virtual source and brightness

The main task of the optical system of any SEM microscope or a similar device is to focus the beam into the smallest possible spot on the target. From optical point of view is the probe on the target a demagnified image of the source. The final size of the spot is hence defined by the size of the source itself, magnitude of demagnification and also by the aberrations inherent to any real optical component. The spot size and consequently the size of the source are important parameters, because they are directly connected to resolution and brightness.

The Schottky and the field emitter in configuration described above are operating in virtual source mode. It means that the projected source image is not an image of the emission surface itself but of the virtual source, which is created at some position behind the apex of the emitter tip. The concept of the virtual source is shown in Figure 6. The tip and the extractor are acting as a weak lens with diverging field. Trajectories of emitted electrons are, despite of their initial angular distribution and energy, almost immediately bent due to strong action of the extraction field. By reverse projection of the individual particles from the plane of the extraction electrode along their velocity tangents an image of the virtual source is created. In the simulation is the position of the image found in the plane with the smallest diameter of the projected spot. From the standpoint of theory is the position given by crossover created by backtracking of electrons with zero tangential energy, whereas the size is given by electrons with nonzero tangential energy [9].

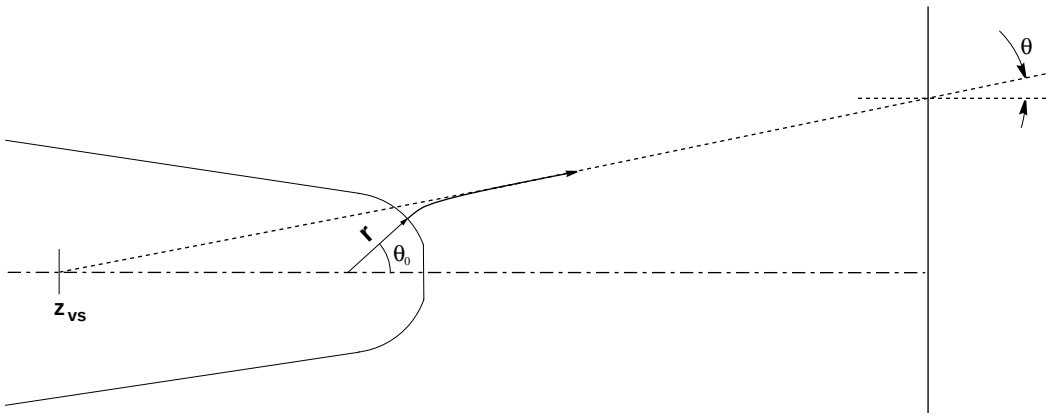

Figure 6: koncept VS - bude tu jiny obrazek

The size and the position of the virtual source are not invariant. Their values are related to the location of the backtracking plane and also to the diameter of the analyzed beam. Also other effects can alter these parameters. In particular coulomb interactions due to their stochastic effects on particle trajectories are responsible for the growth of the virtual source size, mainly in beams with higher current density.

For the design of an electron-optical device is the knowledge of the virtual source size important. The value can be either measured, obtained from simulation or on the assumption that interactions can be neglected also analytically calculated. Experimental evaluation of the virtual source size is due to it's very small dimensions not an easy task. However, several measurement have been published earlier[15, 16]. The expected size of the virtual source is in

the range of 15 - 30nm for Schottky emitter and 1 - 5nm for cold field emitter in dependence on tip radius.

For thermionic, Schottky and field sources are the effects of coulomb interactions neglected in absolute majority of available publications. The diameter of the virtual source is then calculated using following equation derived from geometrical and emission properties of the source [9]

$$d_{v50} = 1.67\frac{r}{m}\sqrt{\frac{\langle E_t \rangle}{eV_{ext}}}. \tag{26}$$

The angular magnification m is a function of emitter radius r. It represents thethe ratio of final trajectory angle θ given by angle in the extraction plane to initial trajectory angle θ_0 given by the starting position of electron

$$m = \frac{\theta}{\theta_0}. \tag{27}$$

The parameter V_{ext} in equation (26) is the potential at the extractor and $\langle E_t \rangle$ is an average initial transverse energy of electrons. In case of thermionic and Schottky emitters is for this energy selected mean transversal energy of Maxwell-Boltzmann distribution kT, where k is the Boltzmann constant and T is the temperature. For cold field emitters is for this energy chosen parameter d given by equation

$$d = \frac{e\hbar F}{\sqrt{8m\phi}}, \tag{28}$$

where the $\hbar$ is the reduced Planck constant, F is field at the tip surface and the ϕ is the work function [41]. The subscript "50" in eq.(26) signifies the diameter containing 50% of the probe current. Bronsgeest in her article picked up a several good reasons for use of full width at 50% of current (FW50) instead of full width at half maximum measure (FWHM). The equation (26) was derived for virtual sources with gaussian intensity profile. In this work are diameter values obtained by reverse tracing and also measured using the FW50. Contrary to the analytical approach is besides the effect of coulomb interactions also influence of the flat facet simulated, at least for the Schottky emitter. The effect of the facet on the virtual source in dependence on the analyzed beam half-opening angle was already evaluated by Tuggle [7], however on a simplified cathode model without coulomb interaction.

Brightness is a very important beam characterizing parameter in electron optics. It help us to measure and compare the performance of electron or ion sources. An average brightness is a function of beam current ΔI over emission angle $\Delta\Omega$ from an emission area ΔA

$$\langle B \rangle = \frac{\Delta I}{\Delta A \Delta \Omega}. \tag{29}$$

The dependence on the selection of particular values of the emission angle and the size of the emission area makes the beam brightness sensitive to field gradients, beam limiting apertures and other effects of active column components. For practical purposes is generally used more convenient reduced brightness, i.e. the brightness divided by the value of the

beam potential. Incorporating angular intensity and the virtual source size, the reduced brightness is given by

$$B_r = \frac{4I'}{\pi d_v^2 V_{ext}}, \tag{30}$$

where I' is the angular current density at the extractor and d_v the virtual source size. An important property of the practical brightness is that it remains constant along the optical axis from the source down to the target, unless coulomb interaction starts to play a role. It allows quantification of current in the probe

$$I_p = B_r \frac{\pi^2}{4} d_v^2 \alpha^2 V_{ext}. \tag{31}$$

with α the aperture angle at the target.

Bronsgeest et al. [9], assuming Gaussian distribution of the current in the virtual source, derived from the electron emission theory for infinite planes relations for practical brightness of thermionic and Schotky emitter

$$B_{pract} = 1.44 \frac{e j_{t,es}}{\pi k T}, \tag{32}$$

and also for field emitter

$$B_{pract} = 1.44 \frac{e j_f}{\pi d}. \tag{33}$$

The parameter j is respective current density on the emitter surface. Other parameters are known from section 2.4.

2.5 Coulomb interactions - overview of theoretical models

The effect of coulomb interactions grows with the current density in the beam. The average distance among emitted electrons is getting shorter and the influence of coulomb repulsive forces starts to play a significant role. It is most critical in the source area, in the beam crossovers and long parallel beam segments, which are created by optical components. It is also strengthened for the lower beam energies. Slower particles have more time to interact.

Coulomb interactions can affect the beam in several ways. The first and also the most pronounced way is a space charge. In the case of very high emission current density, the electrons that were not accelerated enough to escape the emitter area are creating a particle cloud in front of the tip. Their negative charge is lowering the extraction field on the emitter surface and so it acts against the emission process. This is generally typical for thermionic emitters at higher operational temperatures. Schottky and CFE emitter do not suffer from space charge in normal working mode due to their lower temperature. This effect will be therefore omitted in this work.

The second manifestation of CI is known as the Boersch effect, described in 1954. It is a statistical effect where a broadening of the particle energy distribution is caused by the stochastic coulomb interactions (after subtraction of space charge). If the chromatic aberration is dominant, it is the energy spread, which is a very important parameter. The third manifestation is the Loeffler effect (trajectory displacement effect). In this case the stochastic coulomb interactions are broadening the beam diameter and thus reducing the brightness and affecting the resolution.

Several theoretical studies were published on these subjects [21, 22, 23, 24]. Unfortunately they do not provide any comprehensive solution. The physics of stochastic coulomb interactions is complicated and majority of offered models are, in general, restricted to several special cases. Following description of approximative methods is only a brief summary, a more extensive overview was published in [1, 24].

Zimmerman [21] developed a method for evaluation of Boersch effect in a cylindrical beam. His thermodynamic approach to electron energy and the beam propagation greatly increased the understanding of the effect. He described the Boersch effect as a thermodynamic relaxation process of particle internal energy which is represented by local beam temperature [1]. The particles are during the emission process accelerated by the extraction field into one direction. The longitudinal energy spread is then decreased rapidly while the lateral energy spread remains unaffected. The beam energy and consequently the beam temperature have to be distinguished for these directions. The longitudinal and the lateral beam temperature are defined [1] as:

$$T_{||} = \frac{m}{k} < \Delta v_{||}^2 >, \quad T_{\perp} = \frac{m}{2k} < \Delta v_{\perp}^2 > . \tag{34}$$

After acceleration are the internal energies no longer in the equilibrium. The relaxation process occurs, where the coulomb interactions are reducing the temperature differences by relaxing toward more isotropic one. According to Zimmerman, the rms energy spread increases with the square root of the current density. This approach is however based on conditions which are not fulfilled in our case. It can provide a reasonable results in case of a crossover for very dense beams.

Knauer extended Zimmerman's work for converging and diverging beam and found a two-third power dependence of energy broadening on the current density. He also derived equations [22] for prediction of the energy broadening and virtual source growth in acceleration field region of the field emitter. The energy broadening is expressed as:

$$\Delta \bar{E}_z \approx 7.43 \, \frac{I^{2/3}}{V_0^{1/3} \alpha^{4/3} R_s^{1/3}}, \tag{35}$$

where V_0 is the beam potential, I is the beam current, R_s is an effective source radius and α is the beam half-opening angle. The broadened virtual source can be calculated from:

$$d_v^{'} \approx 15.6 \, \pi \, e^{4/3} \frac{m^{1/6}}{(eV_0)^{7/6}} \, R_s^2 \, j_s^{2/3}. \tag{36}$$

Basic presumption of his approximation is that steady Coulomb repulsions among particles are converting potential energy into kinetic energy. Rapidly diverging beam in the emitter area is considered as "collision free". As will be shown later, trajectories of emitted electrons are due to their initial angular distribution frequently crossing each other and mutual collisions cannot be excluded.

A different approach is used in the first-order perturbation model developed by Loeffler and Hudgin [23]. In contrast to previous model, weak interactions and narrow crossover are assumed. The interactions are calculated among a single test particle and all other (field) particles in the surrounding area, which are following their unperturbed trajectories. The respective quantities for evaluation of the Boersch and the Loeffler effects are obtained from integration over all possible trajectories of the field particles relative to the test particle. By the approximation a N-particle problem is reduced to a sum of two-particle problems. The calculated dependence of the energy width on the current density is linear for low current densities and square root dependent for higher beam currents.

Another method, the closest encounter approximation, is assuming that the dominant contribution to the total interaction effect is given by a single interaction of the test particle with a nearest-neighbour particle. Analogous to Loeffler's approach is here the N-particle problem reduced to a two-particle problem. The Models based on the closest encounter approximation are used in simulations performed by Read [37].

The most comprehensive method was developed by Jansen [24]. His method reduces the full N-body problem to a sum of 2-particle interactions as well. The displacement of single test particle is also evaluated but the interactions with all field particles are calculated. Then the probability and finally the distribution of various configurations of surrounding field particles is computed, in order to obtain a statistical distribution of particle displacements. The most interesting outcome of analysis of various displacement distributions is that in dependence on the particle density and the beam geometry four major beam regimes are distinguished: Gaussian for very dense beams, Holtsmark for beams with moderate particle density, Lorentzian for low current densities but weak and complete collisions and a Pencil beam where the average axial distance of particles is much larger than their lateral distances.

Jansen and Kruit [1] derived from Jansen's two-particle approximation [24] a set of analytical expressions, which are covering the Boersch and Loeffler effects for a wide range of beam geometries and operating conditions. Generally are this approximations limited

to monochromatic beams with uniform current distribution propagated in the field free drift space. They do not apply to accelerating source region and the deflector areas which are treated as infinitely thin or at least the particles in the acceleration field are gaining full energy immediately after they left the emission surface or object plane. However, equations for the energy broadening and virtual spot size growth are used for this purpose also in simulations, see eg.[33, 3]. Fransen [10] used these equations for comparison with his experimental results. He divided all terms for individual regimes by 2 in order to take only half of the crossover and the diverging part of the beam into account. The tip of the emitter is then represented by the crossover. For FW50 measure are those equations given by:

$$\Delta E_{FW50\,G} = 208.1\,\frac{I^{1/2}}{V^{1/4}} \qquad \text{for} \qquad r_c \leq \frac{e}{8\varepsilon_0}\frac{1}{\alpha^2 V}, \tag{37}$$

$$\Delta E_{FW50\,H} = 4.877\frac{I^{2/3}}{r_c^{1/3}\,\alpha V^{1/3}}, \tag{38}$$

$$\Delta E_{FW50\,L} = 1.899\cdot 10^5\frac{I}{\alpha\, V^{3/2}}, \tag{39}$$

$$\Delta E_{FW50\,P} = 1.287\cdot 10^{18}\frac{I^2 L}{V}, \tag{40}$$

where the last index letter remarks particular regime, I is total current in the beam, V is beam potential. The r_c is the radius of the crossover, α is half-opening angle and L length of the conical beam segment as shown in figure 7. The FWHM values are obtained with use of following prefactors - 363.3, 7.23, $1.90\cdot 10^5$ and $2.25\cdot 10^{17}$.

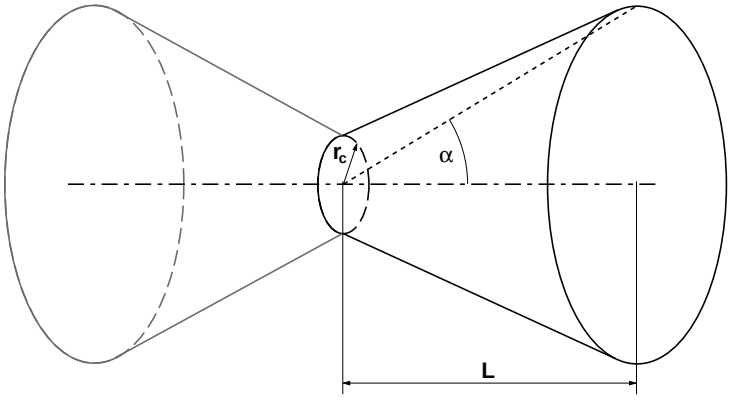

Figure 7: The Jansen's crossover model truncated to one segment for calculation of the interaction effects in the emitter region.

It is not necessary to classify the beam into any of the four regimes. The resulting broadening is obtained from following expression which combines their individual contributions.

$$\frac{1}{\Delta E_{FW50}} = \left[\frac{1}{\Delta E_{FW50\,G}} + \frac{1}{\Delta E_{FW50\,H}} + \frac{1}{\Delta E_{FW50\,L}} + \frac{1}{\Delta E_{FW50\,P}}\right]^{1/4} \tag{41}$$

Jiang [25] developed the slice-method for calculation of coulomb interaction effects. The method is based on Jansen's work and is applicable for regions with potential gradients. In such regions is the beam divided into sections where the potential is assumed to be constant. The trajectory displacements and energy broadening within the section are calculated using Jansen's analytical equations for cylindrical beam segment. The total effect is calculated as a sum of individual contributions. He used this method also for evaluation of the interaction effects in the source area.
The presented list of contributors is surely not complete. Various works with diverse modifications of above mentioned methods or also completely different theories for even more special cases were published till now. Please see the Jansen's monograph [24] or Jansen - Kruit article [1] for details.

2.6 The numerical approach

The numerical approach is frequently used in situations where stochastic effects are taking place. Coulomb interactions in charged particle beams are surely the case. The Monte Carlo is perhaps the most popular and also the most suitable numerical method for computer simulations of this kind of problems.

Several Monte Carlo simulations of coulomb interactions in the electron source region were already published. They were elaborated with a diverse level of complexity. Generally a lot of approximations were introduced in the definition of initial conditions and also in the calculation method of discrete coulomb interactions. The computational performance at that time did not allow more comprehensive models.

Shimoyama et al.(1993)[35] developed a software for calculation of the Boersch effect in the diode region of the field emission gun. He used for his simulation an approximate analytical solution for the potential between the emitter tip and the anode. The simulated tip radius was in the range of 0.05 - 0.4μm with relatively big spacing to anode (5 - 10mm). The tip of the cathode was modeled with a hyperboloid of revolution. Electrons were emitted with a simple cosine angular distribution and a monochromatic energy distribution in total emission current from 5 to 20μA. Coulomb interactions were calculated in every step of numerical integration of equation of motion using Taylor series expansion. He found following dependencies for total energy spread:

$$\Delta E = \sqrt{\Delta E_0^2 + \Delta E_B^2}, \tag{42}$$

where E_0 is the intristic energy width of electrons and E_B is the broadened energy width of monochromatically emitted electrons. Shimoyama also investigated the dependence of the broadened energy on other emitter parameters like the emission current I_E, tip radius R and the distance of the extraction electrode d. Following relation was found:

$$E_B \propto I_E^{-0.75} \times R^{-0.5} \times d^0. \tag{43}$$

The article does not contain any comparison to experimental data or at least to theoretical expectations.

Thomson (1994) [36] performed a Monte Carlo simulation of electron-electron scattering effects for an electron-optical system using field and Schottky emitter with tip radii

10, 100 and 1000nm. He used two different approaches in the model. The gun region were approximated by a spherical cathode with a concentric spherical anode for both emitter types. The interactions of particles in this region were calculated separately as the full N-body problem. Unfortunately, the emission model is not described in a detail. Interactions in the rest of the system were calculated using the formulation of Jansen [24]. The energy broadening obtained from the simulation in the emitter area is compared to expected theoretical values, i.e. without interaction effects, calculated from the available emission theory. He describes the simulation results as "consistent with earlier results" of Swanson [14] without any further comparison.

In the work from Elswijk et al.(1995)[34] a broadening of an electron beam emitted from a single atom source is simulated. Monochromatic electrons are emitted in a random direction with Gaussian angular distribution from a point source. The ray-tracing of the particles is performed in a drift space between the source and the detector. The basic approach in the Monte Carlo simulation is similar to the Jansen's approach. The main difference is a correction of the error in velocities of border particles caused by the limited size of the simulated particle bunch. An analytical approximation, similar to that of Loeffler [23], is derived. The results of the simulation are compared to the new analytical model. A linear dependence of the FWHM of the energy distribution on the current and an inverse square root dependence on energy was found.

Also Read [37], Jansen [24] and others evaluated effects of coulomb interactions with the help of analytical approximations.

2.7 Available software for the Monte Carlo method

Recent rapid growth of computational performance allows us to use "brute force" methods in cases where formerly a lot of limiting simplifications were required in order to reduce the calculation time. However, a simulation of coulomb effects in charged particle beams with large sets of particles is still a very demanding task. Such a complex calculations are possible only with the help of specialized software and powerful hardware. Several commercial applications are available on the market. In general, they are usually based on the finite element method (FEM), the boundary element method (BEM) or the finite difference method (FDM) which are known also from other scientific fields. Here is a brief overview on few most relevant products:

Software package CPO (Charged Particle Optics) [27] is available in several versions. For calculations of emission sources a special 3DS version can be obtained. Although discrete coulomb interactions can be with 3DS calculated, the software makes use of some approximations that should be avoided in this work. For complete evaluation of interactions a separate code would have to be written by the user.

Munro's Electron Beam Software (MEBS) [26] is an application package which consists of several individual tools. OPTICS is calculating the optical properties of any combination of electrostatic and magnetic lenses and deflectors using first order finite element method for their design. The program SOURCE was directly designed for calculations of electron/ion source properties. Unfortunately none of these programs is able to take coulomb interactions into account. BOERSCH and IMAGE are already intended to compute these effects but either only in a drift space between a set of thin lenses or in the electrostatic field, which

is obtained by expansion of the axial potential. Because of nonhomogenous field with very strong gradients in the vicinity of the source, the accuracy of this approach is insufficient.

EOD (Electron Optical Design) [28] is a complex, modern and user-friendly tool for design and analysis of electron-optical components. The field calculation is based on the first order finite element method (FOFEM). The easy CAD-like mesh design is supported by automatic fine mesh generation and a routine for error estimation. Particle raytracing can be performed using various methods with selectable precision. Output data can be easily graphically presented and combined in well-arranged plots. Also different add-inn modules can be used for the solution of special problems. The coulomb interactions are not yet supported.

Monte Carlo simulation program (formerly MONTEC) and INTERAC are software components of Jansen's The MonTec Particle Optics Simulation Tools package [30]. The package is intended for design and optimization of systems impacted by coulomb interactions effects. The program INTERAC provides an interactive user interface for the Monte Carlo simulation routine. Required initial data, selection of processing method and evaluation of simulation output can be here provided. Coulomb interactions can be calculated numerically in full N-body system using method DRIFT1, however lenses and other beam forming components are modeled only with thin-lens approximation. The trajectories of particles are integrated in "drift space" in between them.

Other software packages exist but they are either not suitable for the purpose of this work, very expensive or not accessible at all. A set of software tools for initial data preparation and analysis of simulation results inclusive separate ray-tracing routine was therefore written (following Munro [29]) in order to meet all important requirements.

3 The aim of the thesis

Theoretical and practical emission characteristics of the Schottky TFE and CFE cathodes were studied frequently. An extensive part of the published work is focused on the experimental evaluation of variations of the cathode operational parameters. The influence of the temperature, the extraction field or the size of the tip on the performance of the emitter was investigated for the purpose of further optimization [6, 5]. At higher emission currents a broader energy spreads were measured than predicted in the theory. The effects of the mutual interactions among emitted particles on the energy spread and the virtual source size broadening were widely accepted as the root cause [1, 14, 8, 5, 11]. Due to the stochastic nature of the interactions, it is impossible to measure their contribution separately. A precise Monte Carlo simulation of the emission process with the calculation of the interaction effects seems to be the most suitable tool for such a task. Several simulations focused on the coulomb interaction effects have been already performed. Some of them were focused on the effect of electron-electron interactions in general beams [24, 33, 37]. The most relevant simulations concerned to the source area were addressed in section 2.5 and 2.6. As mentioned in the previous section, they are were elaborated with a diverse level of complexity, using a number of approximations.

Up to now I did not find any distinctively more detailed simulation focused on the coulomb interaction effects in the emitter region. I believe that properly defined initial conditions like the geometrically precise mesh model, the energy and the angular distribution or an extensively calculated interaction effects have a significant influence on simulation results. The aim of this thesis is to evaluate the stochastic effects of the coulomb interactions in the vicinity of the emission source using Monte Carlo simulation. The effects on the energy spread, the virtual source size and brightness will be evaluated. Dependences obtained from the simulation results will be compared to selected experimental data and predicted values from the relevant analytical approximations. A practical usability of the equations for prediction of the broadening effects will be evaluated.

4 Methods

4.1 Software tools and procedures used in the simulation

4.1.1 The field calculation in the emitter model

In order to simulate the source region of the Schottky emitter with real-like fields, surrounding electrodes and shapes of the tip, a model based on FEM, BEM or FDM method is required. Such a model is usually created with help of a specialized software. Although a variety of free tools can be found in Internet, it is hard to find a suitable one for the purpose of this work. Common problems are mainly in restrictions for mesh size, mesh form or portability and suitability for further processing. Programing of some complex model-designing software with required ability to calculate precise field distributions would be tedious. Therefore the mesh design system and the field calculation routine SOELENS from the MEBS software package was used (licensed to Applied Materials - ICT GmbH München). The mesh design method used in this tool is the second order finite element method (SOFEM). The main advantage of the method is the possibility of implementation of curved shapes into the mesh. It allows to model more realistic shapes of the emitter, which is usefull especially at the apex of the tip.

The potential distribution in the mesh is calculated by minimizing of energy functional. The general form of the functional is given by:

$$U_{tot} = \frac{1}{2}\varepsilon \int\int\int \nabla\Phi \cdot \nabla\Phi \, \mathrm{d}v \tag{44}$$

where ε is the permitivity and Φ is the potential at a general point in the mesh.

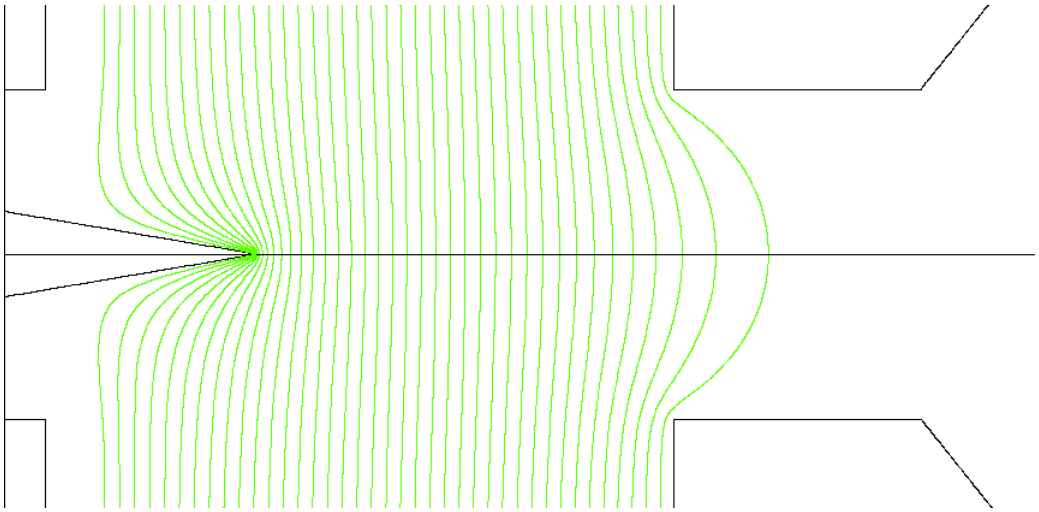

Figure 8: An example of the calculated field distribution in the emitter area. The single vertical lines represents the electrostatic field equipotentials.

The quality of the calculated field is important. The accuracy can be controlled relatively easily. One way is the method used in the EOD software package [28]. To the evaluated mesh is an equivalent mesh created. This mesh has doubled density, i.e. double number

of mesh lines in the horizontal and the vertical direction. The appropriate electrostatic fields are calculated. The potential values in consonant mesh points are compared. If the potential at the mesh points vary significantly, the original mesh has to be refined. The main advantage of this method is a possibility of a graphical visualization of the location and extent of errors. The other approach is to test the quality of the mesh model by tracing of test particles. A few test particles are traced through the field of the first model and landing coordinates are noted. In the next step is the mesh of the model refined and the electrostatic field recalculated. The ray-tracing is repeated and values of landing positions are compared to results of the first run. Again, if differences are significant, the mesh model has to be refined and evaluated again. In this simulation were used both methods for tests of the emitter model. The final maximal error in the position of the traced particle using the second method was in the range of few nanometers.

The calculation of the electrostatic field within the analytical model used for the simulation of the cold field emitter model is performed in different way. A set of analytical equations is derived from the the analytical potential distribution of the model. The complete description is in section 4.3.

4.1.2 Ray-tracing routine

The another step was to program a new ray-tracing routine. Existing programs could not be used from reasons mentioned in the previous subsection. Also specialized program SOURCE from the MEBS package, intended for calculation of emitter properties, is calculating trajectories of particles only sequentially. The calculation of the trajectory of the second particle is not started until the first particle pass the final screen plane. This method eliminates a realistic simulation of the emission process and eventual evaluation of coulomb interactions. The majority of the programs also do not support more then one screen plane, which is important for the analysis of evolution of interaction effects on various beam parameters. Also data provided in output files are insufficient for complete data analysis and fine-tunning of the simulation process. In general, the new ray-tracing program has to meet several requirements.

- Ability to read and process prepared input data
- Trace particles simultaneously
- Ability to calculate coulomb forces among particles
- Store relevant data from multiple screen planes

The development of the input interface for the simulation program was done with the help of the MEBS package documentation (part of the license).

The core of the ray-tracing program is the solver for equation of the particle motion, which is given by:

$$m\frac{\mathrm{d}^2}{\mathrm{d}t^2}\vec{r_i} = e\vec{E} + \frac{1}{4\pi\varepsilon_0}e^2\sum_{i\neq j}\frac{\vec{r_i}-\vec{r_j}}{|\vec{r_i}-\vec{r_j}|^3}, \tag{45}$$

where m is the mass of electron, $\vec{r}$ is the position vector, $e\vec{E}$ expresses the influence of the field and the second term on the right side of the equation is accounting for the coulomb

interactions. The interactions are calculated directly, so the mutual coulomb repulsion forces between each pair of particles are evaluated. This is the most time-consuming part of the simulation. A system with N particles requires N(N+1)/2 force evaluations for each time step. The fields generated by interactions are within the integration added to the global field of the mesh. For the numerical integration was selected the fifth order Runge-Kutta method with with Cash-Karp parameters and the adaptive step size [31]. The length of the integration time step is automatically adapted so, that the local integration error does not exceed some predefined value. The step has to be small enough for accurate calculation of interactions, but not too small because of rapidly growing integration time which is directly dependent on the number of integration steps. The value of the maximal time step was optimized in a test on a two-particle collision example.

It looks like the numerical integration of multiple particles is a good example of problem that could be solved with use of parallel processing on a multiprocessor system, but unfortunately, it is not the case. The fifth order Runge-Kutta method evaluates five estimating "half" steps in one regular time step. The coulomb interaction are in our case calculated in every estimation step. The positions of all emitted particles in system has to be "frozen" until the calculation of their reciprocal forces is completed, so the particle trajectories cannot be integrated completely independently and at some level a data synchronization is needed. The calculation of coulomb forces can be also reduced to one evaluation after the regular time step, but it is at the costs of the precision. Another possibility seems to be a reduction of the problem to parallel calculation of mutual forces only instead of the whole integration. I followed mainly this approach. The calculation of coulomb forces was parallelized and the performance tested on a modern multiprocessor system. The testing conditions were adjusted to a standard simulation conditions. For 1000 - 5000 testing particles in a bunch was the parallel code 4 - 1.5 times slower than serial code. The reason is that the system overhead (time needed for a creation of multiple calculation threads) is too high for such a small bunch of particles. The maximal number of integrated particles in the emitter area depends mainly on simulated total current. In the model of a Schottky emitter with tip radius about 0.5μm and at angular intensity of 400μA/sr is at the distance of 1mm about 5500 particles. The parallel computing up to date could be an advantage in simulation of interactions in beams with much higher number of particles.

4.1.3 Initial data

If the emitter model and the ray-tracing routine are prepared, the initial conditions for the simulation have to be generated. Following data are needed:

- the suppressor and the extractor potentials
- basic ray-tracing settings
- the particle data
  - starting positions
  - initial energy
  - starting angle
  - time of the start

Preparation of initial data is a complex procedure. In practice is the emission current adjusted by variable operational parameters to some particular value of the angular intensity. The angular intensity is a relatively easily measurable parameter. It can be obtained by measuring the emission current I of the beam in â solid angle Ω delimited by a small aperture behind the extractor electrode:

$$I' = \frac{I}{\Omega} \tag{46}$$

It is thus reasonable to simulate the electron-electron interactions also in relation to the angular intensity, which can be easily calculated. An emitter with given tip diameter, shape, work function and temperature needs a particular value of the voltage at the suppressor and the extractor electrode, in order to achieve a concrete value of the angular intensity. A real emitter is usually supplied with a data sheet containing all requested parameters for several emission working points, i.e. angular intensity values. The parameters usually vary also for emitters with the same tip radius due to manufacturing tolerances and cannot be therefore used for the simulation of the emitter model directly. Some of these parameters like the work function and the temperature are frequently considered as an invariant physical which value is known from the theoretical approximations or various experiments. Other parameters like the value of the suppressor voltage are operational characteristic with an empirically determined value from the practical emitter operation. These parameters will be set as a constant also in our simulations. The remaining variables like the extractor voltage for a particular angular intensity value have to be calculated.

The following procedure is used for calculation of dependence of the angular intensity on extractor voltage: The simulation of the electron emission (a bunch of 20000 particles without accounting of interactions) is performed for several values of the extractor voltage from the range $2000 - 5000V$. From simulation results is the emission current at given extractor voltage under half-opening angle of $1°$ after the plane of the extractor electrode measured and the angular intensity subsequently calculated. An extractor voltage for an arbitrary value of the angular intensity is then interpolated from the previously calculated dependence. In this manner are defined working points for the simulation. The calculated dependence is due to relatively low number of particles under the limiting half-opening angle and missing effect of the coulomb interactions not very accurate, but good enough for a basic orientation.

The generation of initial particle data like the starting position, initial energy and starting angle is bundled with previously presented theoretical approximations, partially emitter specific and therefore described in more detail in particular sections.

The requested amount of initial data needed for various simulation conditions is huge. A special program was written for this purpose. The created software routine is generating and preparing the complete input for the ray-tracing routine. The individual settings and conditions for every simulation run can be stored, and if needed later, reused for generation of new initial particle data.

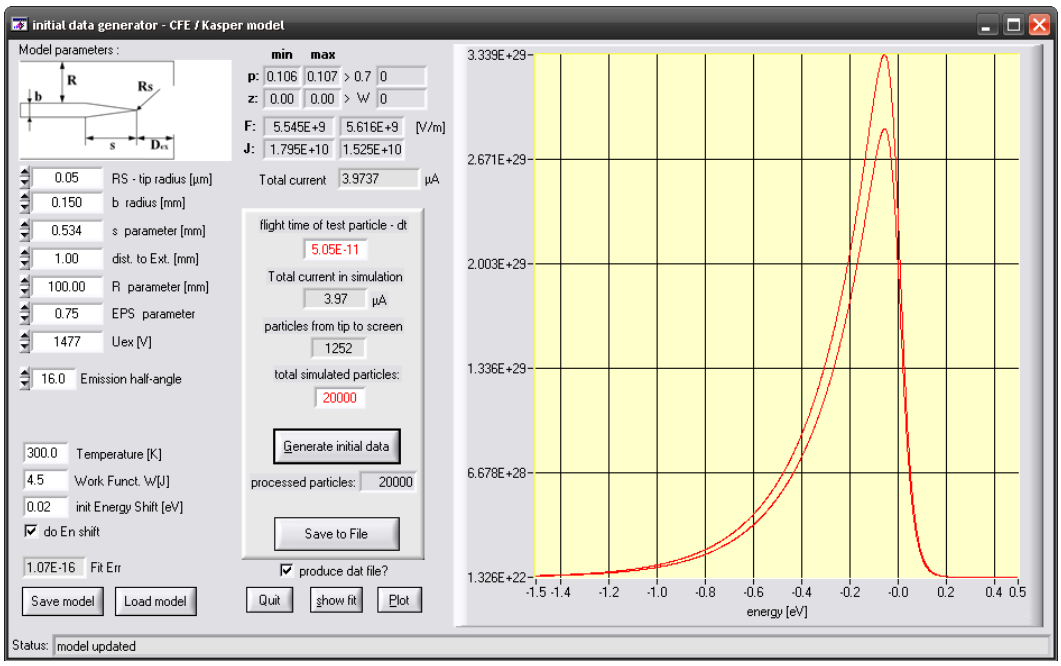

Figure 9: Screen-shot of the initial data generator for the simulation of the cold field emitter

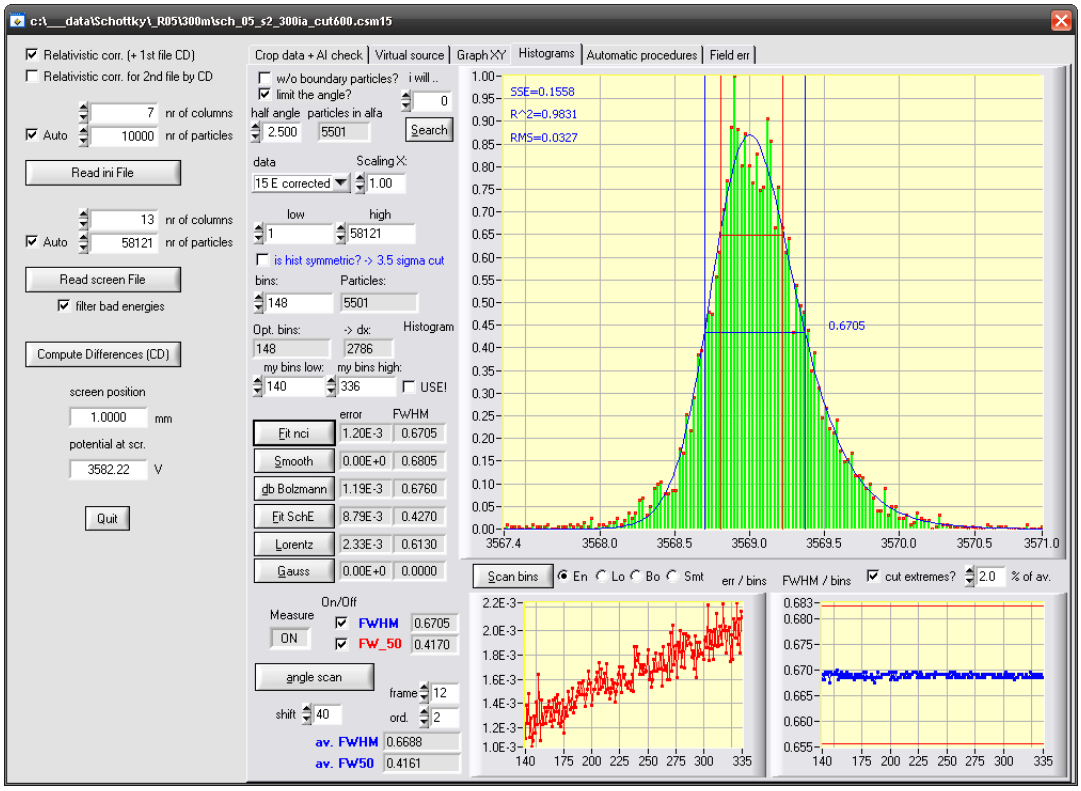

Figure 10: Screen-shot of the data analysis program.

4.1.4 Data processing and analysis

Before the data acquired from the simulations can be analyzed, they have to be processed. As a first step, it is necessary to clean the data from systematic errors, which are caused by the limitations of the simulation process.

Particles at the front and at the end of the emitted bunch do not have enough neighbors and the forces acting on them are unbalanced. It results practically in the acceleration of particles at the front of the emission sample and slowing those at the end. Affected particles have to be excluded, which reduces the total amount of particles available for the subsequent data analysis. This effect is significant especially at higher emission currents, which are unfortunately also more time consuming in the simulation. It can be partially suppressed for the particles at the end of the simulated bunch by prolongated ray-tracing of the particles beyond the last screen plane. Figure 11 shows the deviation of the energy distribution of particles in dependence on the landing time at the front and at the end of the emission bunch. The number of eliminated border particles can be determined empirically

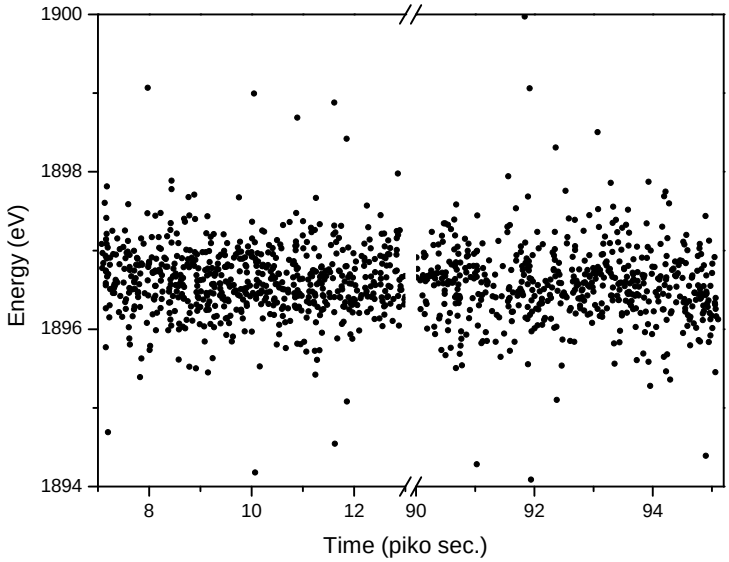

Figure 11: Energy deviations at the front and at the end of the particle packet.

from the visualized dependence similar to the one in figure 11, use some statistical method like the box plot or with the help of method used by Radlička in [4].

The energy distribution of the beam is obtained from recorded energy values in the screen plane. The potential distribution in the planar virtual screen does not conform to rounded equipotential field surface especially near the emitter tip. The mean energy of electrons recorded further away from the axis is then higher than the energy of axial electrons. This difference has to be corrected and the energy is recalculated using formula [4]:

$$E_{corr} = E - q\left(\varphi(z) - \varphi(z,r)\right), \tag{47}$$

with E the recorded energy, q the charge, $\varphi(z)$ the axial potential in the plane of the screen and $\varphi(z,r)$ the potential in the place where the electron was recorded. For the evaluation

of energy width is used FWHM (full width at half maximum) and also FW50 measure on histogram of particle energies.

The major part of traced particles is usually not interesting for the final evaluation of the cathode emission parameters or the evaluation of the interaction effects. As already mentioned, in a real electron-optical systems is the beam diameter at some point after the extractor electrode limited by an aperture in order to reduce the effects of source aberrations. Also in the special purpose experiments like measurements of the energy width of the source [3, 5, 10] was used an energy analyzer, where electron beam is limited by several apertures.

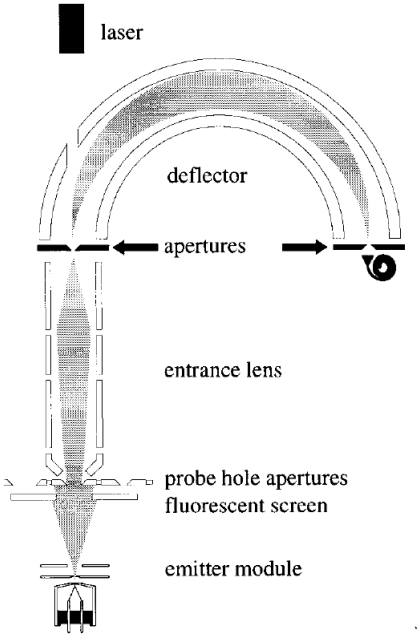

Figure 12: Experimental setup used by Fransen et al. for Total energy distribution measurements [10]

The beam parameters are changing with the distance from the axis. For comparison with an experimental data acquired under particular condition, for example after very small aperture, only particles under a carefully selected half-opening angle after the extractor plane have to be analyzed. The evaluated parameter should not show variation in the lateral direction. This step again reduces the number of particles available for the analysis. It obviously significantly increases amount of required initial particles in the simulation and thus also the computational time, in order to provide enough data for evaluation.

The last program developed for the purposes of this work was a data analysis program. Beam parameters like the angular intensity, the virtual source size and the energy width can be easily measured in this application. The program is able to perform full processing of the simulated data as described in this section and also make some basic statistic calculations, fit functions to histograms and measure their relevant parameters.

4.1.5 The simulation process

The whole simulation process is composed of several steps. Figure 13 shows the schematics of the basic procedure.

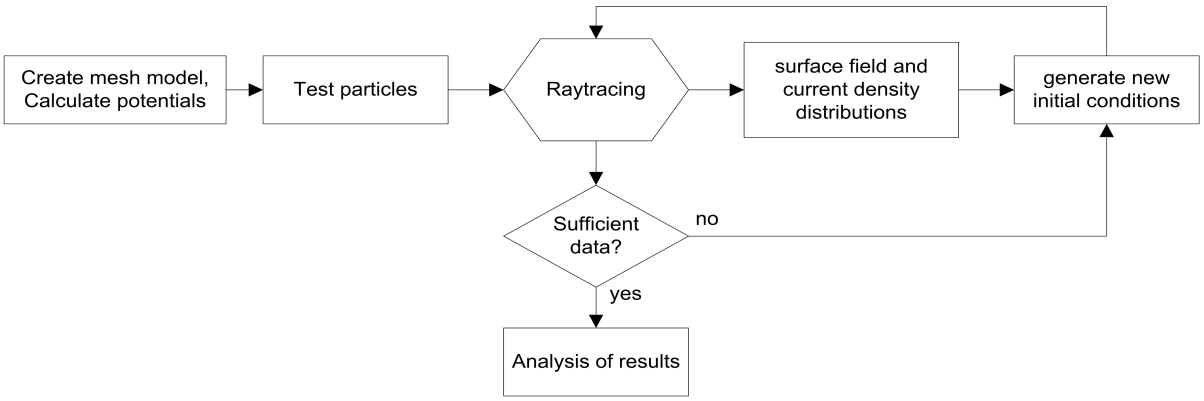

Figure 13: The simulation process

At the beginning a suitable model of the emitter with predefined parameters has to be made. In this work an analytical model for the field emitter and a numerical mesh model based on FEM method for the Schottky emitter is used.

First ray-tracing run with special test particles is done in order to calculate the electrostatic field distribution on the emitter surface and also to detect the average flight time of the particles under this particular condition. In the case of the field emitter is the field distribution given analytically, but the average flight time is obtained in the same manner. Subsequently the current density distribution and total emission current are calculated using equations from the section 2.3. These parameters are used for the preparation of regular initial data like starting positions, energy and angular distribution of particles.

The time distribution of an arbitrarily large set of particles in the emission process can be obtained from:

$$\Delta t = \frac{qN}{I} \tag{48}$$

where Δt is total emission time for the set of N particles, q is the charge of the electron and I the total emission current. Randomly generated emission time has a uniform distribution. With use of the special software written for this purpose complete input data are generated.

In the next step are particle trajectories calculated using the ray-tracing routine. If some particle reaches the screen plane, the actual position, slope and final energy is recorded into an output file. Up to 100 additional recording planes can be defined in the space between the surface of the cathode and the output screening plane. Particles that leaved the region of the mesh model and have not reached the requested screen plane or simply collided with an electrode are automatically excluded. The simulations are performed with several bunches of particles for every working point, i.e. emitter radius and value of the angular intensity. The size of the simulated particle bunch was in our simulations about 30 - 40 thousand particles. The output data are processed and if sufficient data are collected the analysis can begin, otherwise a new bunch of particles has to be generated and ray-traced.

4.2 Simulation of the Schottky emitter

4.2.1 Emitter model of Schottky TFE

Suitable emitter model is the basic condition for the simulation. A variety of cathode models were formerly proposed in published papers. Some of them were approximating the tip of the cathode by different basic shapes, that especially in the case of Schottky emitter, lead due to the absence of the flat facet to inaccurate results. Later also advanced models of the tip, already with the facet, the suppressor and the extractor electrode, were investigated in detail by Tuggle and Swanson [7], but without accounting for the interaction effects. For the purpose of this work a mesh model of a real Schottky emitter in triode configuration was created. Figure 14 shows full scale outline of simulated Schottky emitter with marked bore dimensions and distances between the emitter tip, the suppressor and the extractor electrode. The presented configuration is in general a standard, commercially obtainable emitter mini-module. The 2D model is rotationally symmetric along the z axis represented by the dot-dashed line.

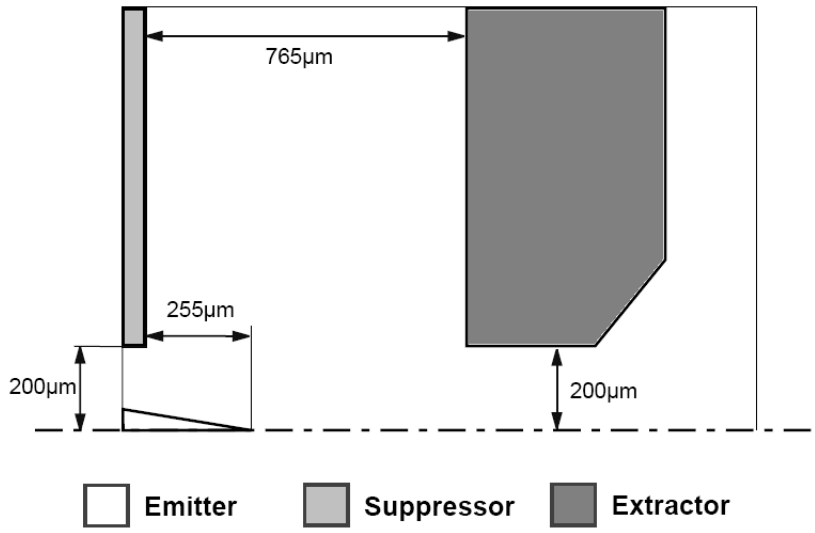

Figure 14: Sketch of the simulated Schottky emitter. The border of the whole mesh area is indicated with thin line at the top and also both sides. Total dimensions are 1mm height and 1.32mm width.

The simulation was performed for emitters with the tip radii 0.5, 1.0 and 1.5μm. The potential of the tip was set to zero. The voltage at the suppressor is fixed on -300 V and the extractor voltage was adjusted to value on which the angular intensity of the beam reached approximately 50, 100, 200, 300 and 400 μA/sr. The right border of the mesh was set to the potential of the extraction electrode. Accordingly, the area behind the extractor is considered as field free. The temperature was for all radii set to 1800K and the work function to 2.8 eV.

The shape of the emitter tip was directly replicated into the mesh model from an emitter micrograph. Figure 15 shows a typical micrograph from a standard datasheet delivered with

an emitter. The radius of the tip is about 0.5μm and the diameter of the flat facet is 0.3μm. The ratio of the facet diameter to the tip radius is 0.6, which is typical for an stabilized faceted emitter operating at normal angular intensity in the range of 0.5 – 1.0μA/sr [1].

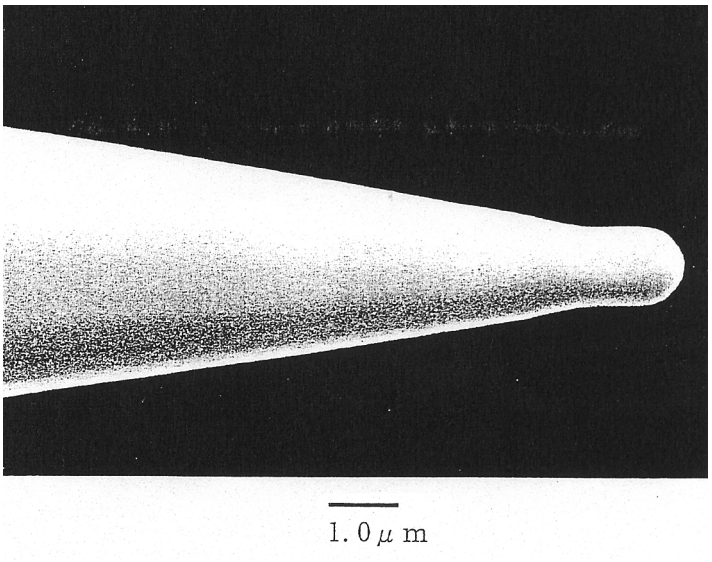

Figure 15: An example of the emitter tip micrograph.

In Figure 16 is a detail of the emitter tip within the rotationally symmetric mesh model with principal mesh lines. Although the mesh model matches one concrete real emitter with specific shape and radius, it is relatively easy to scale it and so to get another model with different tip radii. In this way were also mesh models with tip radii 1.0 and 1.5μm generated. The scaled models were compared to micrographs of real emitters with appropriate tip radius size (originated from the same supplier). Differences in the tip shape were negligible. The evaluation of the coulomb interactions and other beam parameters in dependence on the emitter radius based on the scaled mesh model is therefore feasible. There are, of course, emitters with significantly different shape of the tip, but the influence of changes in shape on coulomb interactions are not studied in this work.

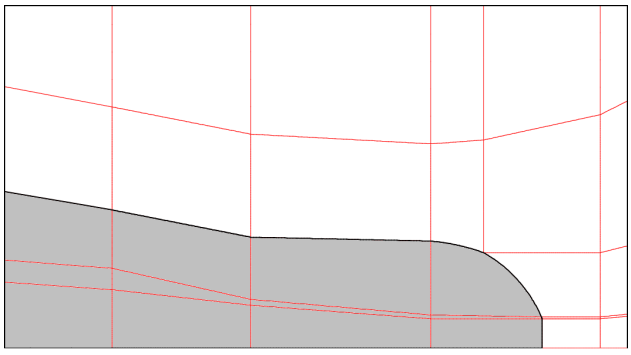

Figure 16: Detail of apex of the emitter model with principal mesh lines. The facet diameter is 0.3μm.

As already mentioned, the quality of the mesh in crucial for the calculation of the field distribution. In order to minimize possible errors, the mesh model has to be very fine. Especially locations with strong field gradient, where the emitter or the electrode shape is changing dramatically, are common source of errors, if the mesh is not generated properly. The critical places have to be carefully examined. In our case is the area near the flat facet and it's edge such a place. The TFE model used in this work has cca. 9 million fine-mesh points. The distances among the fine mesh lines near the flat facet are about 5nm. The time needed for computation of the potential distribution on computer with a 2.33GHz Intel(R) XEON(TM) 5140 processor is about 5 hours (single core process on a 64 bit linux system).

Figure 17 shows calculated axial potential along the z axis for one particular value of the extraction voltage. An expected result is the lower axial field values for emitters with higher tip radii. The almost flat end of the curve corresponds to the course of the potential in the area of the extractor bore.

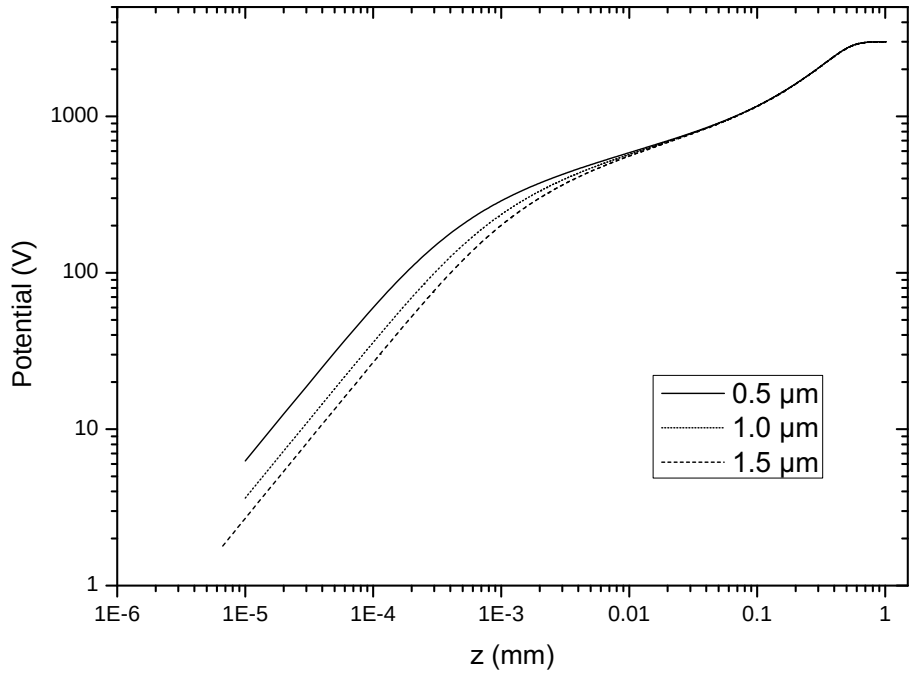

Figure 17: The axial potential distribution for all three radii of emitter at extractor potential $U_{EX} = 3000V$.

4.2.2 Field on the surface and current density

For correct evaluation of the emission current density is the knowledge of the value of electrostatic field on the emitter surface crucial. The intensity of the field at the emitter surface depends mainly on the potential of the extractor and the suppressor electrode, but also on several geometrical factors, like the tip radius, tip shape, the electrode spacing and bore sizes. The presence of the flat facet on the emitter apex has a significant impact on the local field distribution. Tuggle and Swanson [7] found that the effect of the facet is to compress the trajectories and it is also decreasing the surface field and herewith the current

density on the emitter near its axis. In the first mesh model version [38] was the edge of the facet modeled by a simple acute angle. The surface field in the vicinity of the facet edge was analyzed. The consequence of the sharp edge of the facet in the mesh model was an overestimation of the electrostatic field on the edge with relatively strong oscillations in the field value. In order to avoid this error, the edge was slightly rounded and the mesh refined. The program used by Tuggle did not allow any curvature on edge of the flat facet and the field values near the edge had to be extrapolated. In Figure 18 is shown the calculated distribution of the electrostatic field along the emitter facet and above. The field in the middle of the rounded edge ($r = 0.025\mu m$) is over 1.7 times higher than on the emitter axis.

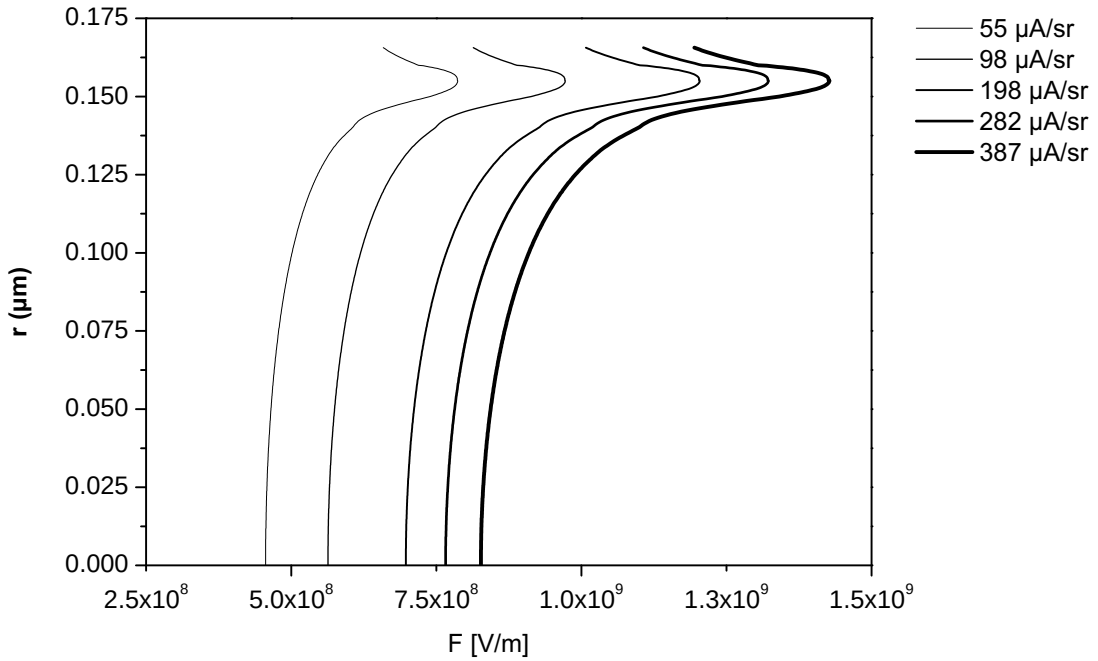

Figure 18: Surface field on emitter facet of radius $0.15\mu m$ for several values of angular intesity.

Knowing the field distribution at the emitter surface, the current density distribution can be calculated. The Schottky emitter is operating in the extended Schottky mode. Accordingly was the equation (13) used for the calculation of the emission current density. The possible changes of the temperature and the work function along the profile of the facet were assumed as negligible and therefore neglected. Figure 19 shows the current density distribution along the flat facet radius, again with values calculated also behind the edge. If the varying electrostatic field is taken into account, the current density value at the facet edge is about 11 times higher than on the axis. The total current from the flat facet area is for the $0.5\ \mu m$ tip radius at the extractor voltage $U_{ex} = 3290\,kV$, i.e. for angular intensity $200\mu A/sr$ about $6.63\mu A$. If the axial value of the electrostatic field would be used as a constant for the whole facet, the resulting total current would be only $3.34\mu A$. The interaction effects depend strongly on the current density in the beam. From this point of view is such a difference in emission current significant and the effect of the flat facet on the electrostatic field and consequently the current density distribution has to be taken into account in the simulation.

In practically all published simulations of coulomb interactions in the source area was the effect of the flat facet ignored (see section 2.6).

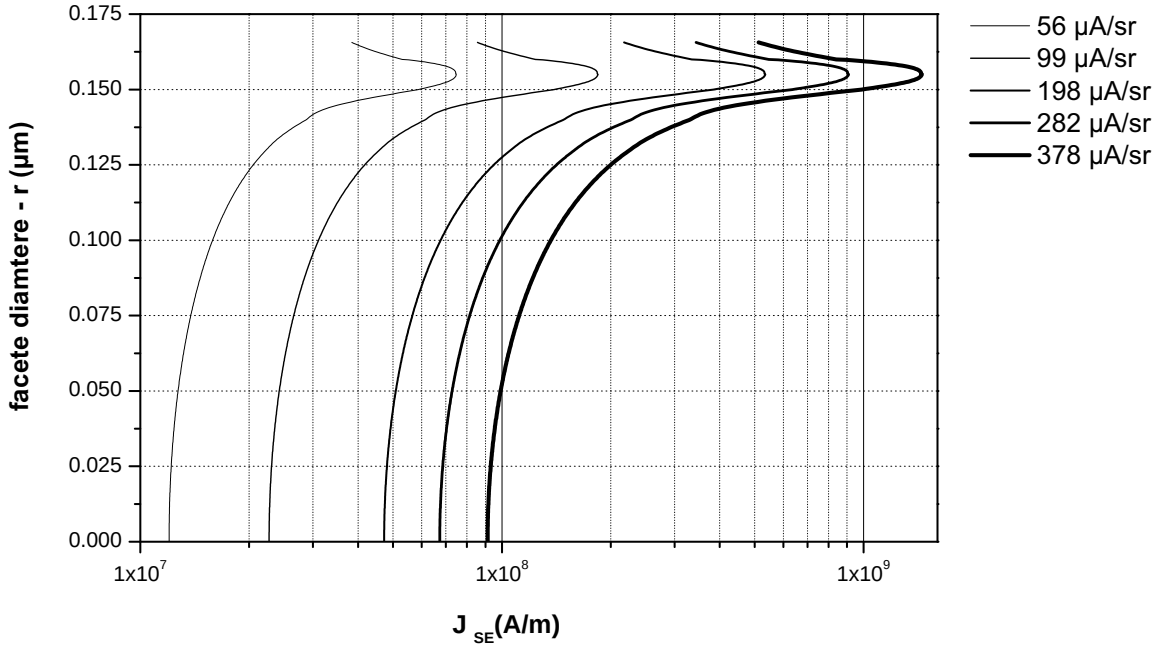

Figure 19: Current density distribution on emitter facet for r=0.5 μm.

From the calculated current density the appropriate distribution function for the generator of random initial positions can be derived. An important decision point is the selection of the size of the emission area which will be used in the simulation. In published calculations was frequently selected for the simulation of the beam properties, whenever the mutual interactions were evaluated or not, only a very small emission area near the emitter axis. The main justification in such a case is that for practical purposes is usually the absolute majority of the emitted electrons shielded by some distant beam limiting aperture. The particles that pass the aperture are coming from the small emission area near the axis. However, it is to a certain extent correct, such a simplification of the emission model cannot be employed in our case. For the evaluation of the interaction effects in the vicinity of the emitter tip are also electrons coming from the larger emission area important.

The longitudinal and the lateral distances among electrons near the apex of the tip are relatively small due to their low velocity, immediately after the emission. The electron emitted from the center of the facet interacts with another one, which was emitted from the facet edge or behind a little while after the first one. The most realistic simulation would take into account also electrons emitted from parts far from the apex of the tip, with current density according to the surface electrostatic field distribution. The main problem in such an approach is the total number of electrons in the simulation. The computational effort grows with N^2 particles. The direct calculation of mutual interactions in such a case with almost all possible electrons is not manageable yet and some approximation method has to take place. In order to preserve the possibility of the direct calculation of interactions, the size of the simulated emission area has to be reduced.

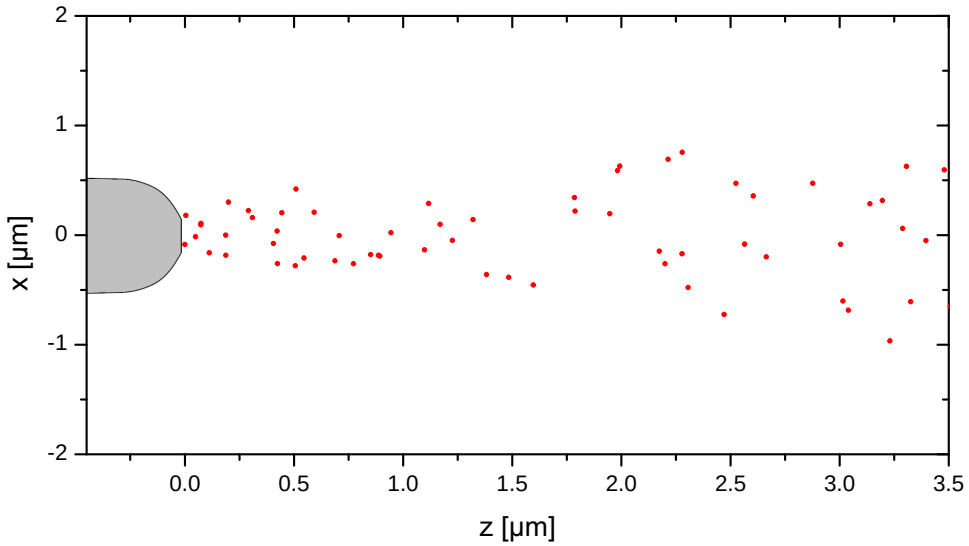

Figure 20: An example of the density of emitted electrons near the tip ($r = 0.5\mu m$ at $I' = 387\mu A/sr$).

The emission current density behind the facet edge falls quickly due to significant weakening of the electrostatic field. The trajectories of electrons which are starting from that area have much larger angles with respect to the optical axis, see Figure 21. The distance of particles from the optical axis is quickly growing. These two effects are reducing the contribution of electrons emitted from this area to the effects of the coulomb interactions. For the purpose of this simulation were used electrons emitted from the whole flat facet, the rounded edge and an additional thin stripe behind the edge in the length of 5% of the facet radius.

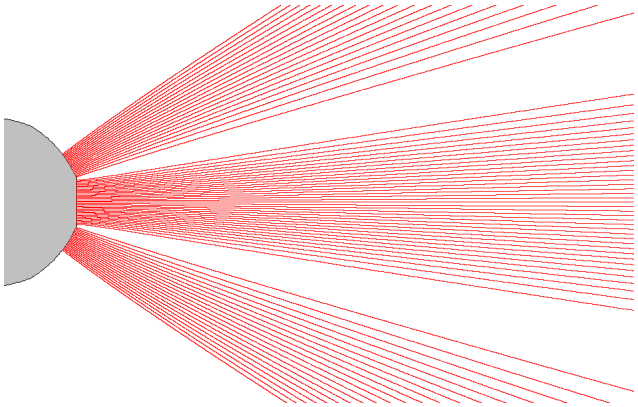

Figure 21: The trajectories calculated with zero start angle from the apex of the tip. The emission from the edge of the flat facet was suppressed, resulting into two spreading white gaps. ($r = 0.5\mu m$ at $I' = 387\mu A/sr$)

In summary, the following procedure is used for the generation of the starting positions of electrons. In the mesh model we determine from several values of the electrostatic field along the shape of the emission area the electrostatic field distribution and subsequently the current density distribution calculated. The appropriate distribution function for the generator of random initial positions is derived. The starting positions of electrons are generated using random number generator with the derived distribution function. Figure 22 shows randomly generated initial positions for 3000 particles from the emission area defined above.

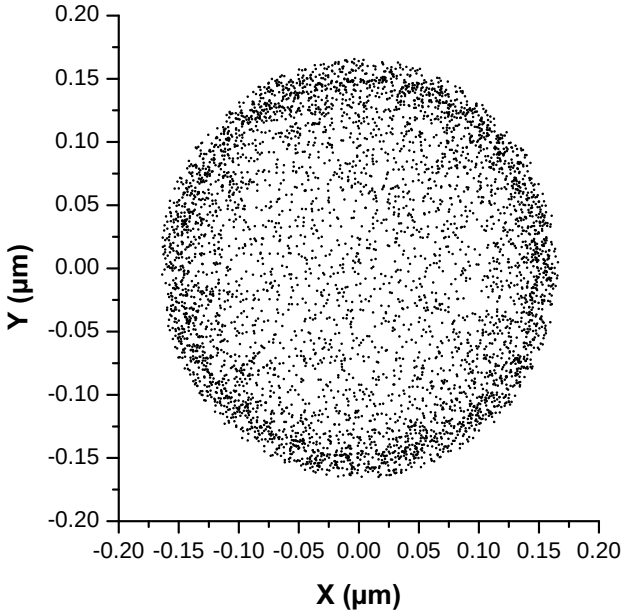

Figure 22: Randomly generated initial particle positions ($r = 0.5\mu$m at $I' = 200\mu$A/sr).

4.2.3 Initial energy distribution

Electrons emitted from the cathode surface have some specific energy distribution. This distribution strongly depends on the emission mode, i.e. on temperature, work function and field strength. The Schottky emitter is operating with a higher extraction field. According to the extended Schottky emission model with a parabolic-barrier approximation, the tunneling of electrons occurs at the top of the potential barrier already during the normal operation of the emitter. The analytical expression for the total energy distribution (TED) can be derived from the emission theory together with the equation for the current density (13), which was previously used for the generation of the particle starting positions. The energy distribution is then given by eq.(15). It applies to the whole operational range of the emitter used in practical applications.

In the previous section has been shown, that the electrostatic field on the emission surface of a real emitter is varying with the distance from the emitter axis. It defines not only the resulting current distribution of the emission, but it also affects the local energy distribution. Figure 23 shows the generated energy distribution for axial and facet edge field values. The particular values of the energy width measured with FWHM are for the tip with 0.5μm

radius 0.462 and 0.595eV, for the tip with 1.0μm radius 0.423 and 0.491eV and finally for the tip with 1.5μm radius 0.408 and 0.461eV, respectively. The first value is always related to the axial and the second one to the edge field value.

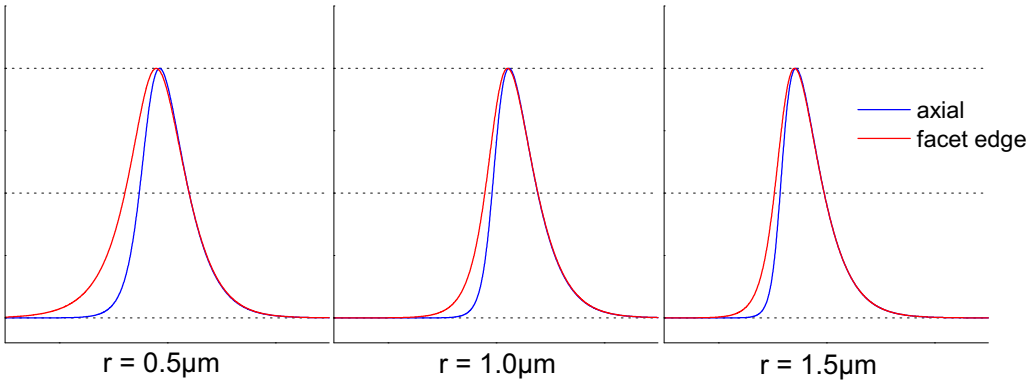

Figure 23: Generated initial total energy distributions for all three emitter radii at angular intensity I' of 200μA/sr. The distribution curves were normalized and shifted along the energy axis for better comparison.

For an arbitrary particle according to its location on the emission surface a field value F is determined. Subsequently the corresponding energy distribution is calculated. A random energy value from the distribution is selected and assigned to the particle. The electron-optical model of the emitter tip does not include coulomb potential. Therefore the slope of the barrier was approximated by a triangle.

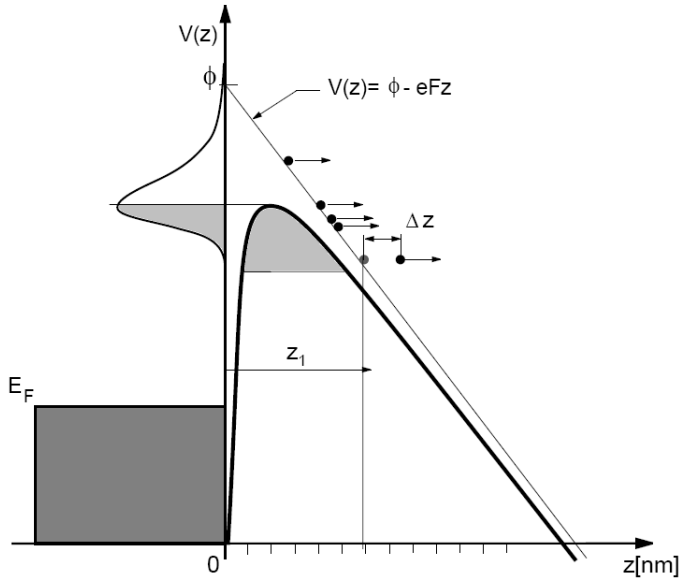

Figure 24: Barrier model

The slope of the barrier approximation is defined by:

$$V(z) = \phi - eFz \tag{49}$$

In order to model the emission process as accurately as possible, the following approach has been applied. The electrons in the metal have certain energy measured with respect to the bottom of the conduction band. If they travel towards the potential barrier (see Fig. 24), they can tunnel through and appear on the other side at the position z_1 which depends on their energy. This position would be the starting position for further simulation. Just behind the barrier the electrons would have the kinetic energy close to zero. This is problematic for the initial calculation of the electron starting angle. Therefore some small shift Δz to the initial position is introduced, which brings to the electron a corresponding shift in the energy and initial angular distribution can be calculated. The same approach is applied also for electrons with higher energy, which would normally pass above the barrier without tunneling.

4.2.4 Initial angular distribution

In the case of thermionic emission the polar angular distribution of emitted electrons is given by a simple Lambert's cosine law. If a strong field is applied to the cathode surface like in the case of the Schottky and the cold field emitter, the angular distribution is also affected. For every emitted particle a random polar angle is generated according to the Equation (17).

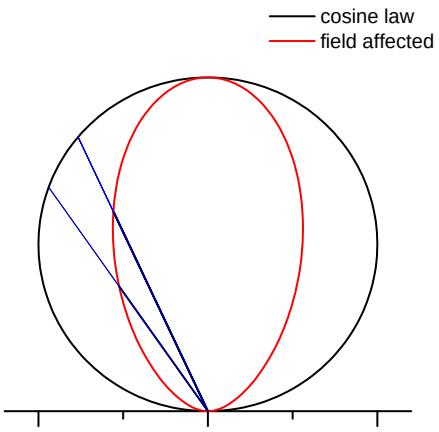

Figure 25: Comparison of the cosine and the field affected angular distributions.

The "shape" of the distribution is changing with the position of the electron with respect to the Fermi level and also with parameter d, which is strongly dependent on the field (see [2] page 927). The Equation (17) can be used for the whole energy range of emitted particles. Electrons at the potential barrier have the distribution influenced by the strong electrostatic field. At the top of the barrier and above is the distribution changed to simple cosine law. The azimuthal angle is randomly generated between 0 and 2π radians. In order to make the model as accurate as possible, we implemented the field-sensitive angular distribution into our emission model. In our opinion, the angular distribution has a significant effect mainly on the virtual source size of the emitter.

4.3 Simulation of the Field emitter

4.3.1 The model of field emitter

As already mentioned in previous sections, an analytical emitter model was used to support the development of the software tools used in the simulations. On that model we could check the basic functionality and the precision of the ray-tracing routine and the evaluation of coulomb interaction effects. This model was subsequently used also for the cold field emitter. Although the simple analytical model might not be suitable to calculate all emitter properties, it is a relatively simple and precise tool to study the effect of the coulomb interactions within the electron gun.

First of all, it has to be noticed that, in the case of the cold field emitter, the apex of the tip during the emission process does not have an exactly defined shape. Dimensions of the tip radius are in the range of tens to maximum few hundred nanometers and thus it is extremely small. Strong extraction field in combination with the high emission current can change the shape of the tip significantly, compared to its condition before the emission. Analogous to Schottky cathode, some kind of facet is growing up willfully or by controlled pre-processing during the emission under appropriate conditions [39]. Unfortunately there is a variety of possible shape configurations and one of the the most used crystallographic orientation, the $\langle 310 \rangle$, is not even axisymmetric. Generally, the absence of the full rotational symmetry makes the creation of a precise model very complicated. Nevertheless, for a basic evaluation of the stochastic effects of coulomb interactions in the vicinity of the source, a simplified model is surely sufficient.

A simple analytical model of pointed emitter, more precisely a diode field model, was developed by Kasper in 1978 [2]. Unlike other simple analytic approximations like the point source and the sphere model [40], this concept allows us to calculate a quite realistic field distribution near the tip apex and so simulate most important properties of the cathode. It also includes the effect of the emitter shank and the wehnelt tube on the field distribution near the tip. There are, of course, also other analytical models of similar quality like the SOC (Sphere on Orthogonal Cone) model, which was used and closely evaluated in Monte Carlo simulation [41]. Compared to the Kasper's approach is the SOC model much more complex and requires considerably more computational effort without any significant advantage. Next part of this section, in general, follows briefly the Kasper's model description in [2]. The model consists of two parts. The narrowing part of the tip is simulated by a wire represented by half-line charge with charge per unit q, defined on $(-\inf < z < 0\rangle$ and a point charge Q_S at its end, i.e. $z = 0$. Figure 26 shows the cross-section of the tip model.

Spherical (r, θ, φ) and cylindrical (ρ, ω, z) coordinates are used here simultaneously. Conversion relations between the coordinates are:

$$\begin{aligned} z &= r\ \cos\vartheta, \\ \rho &= r\ \sin\vartheta, \\ r &= \sqrt{\rho^2 + z^2}, \\ \varphi &= \omega. \end{aligned} \tag{50}$$

The relation for potential of this model is written for simplicity in CGS-units:

$$P(\rho, z) = q \ln\left(\frac{r+z}{C_1}\right) + \frac{Q_S}{r} + C_2, \tag{51}$$

where charge q is given in V, point charge Q_S in Vm. The dimensionless constants C_1 and C_2 are determined by the boundary condition $P(a, 0) = 0$, i.e. the potential at the emitter surface is set to zero as it is usual in the electron optics. The point charge Q_S is always

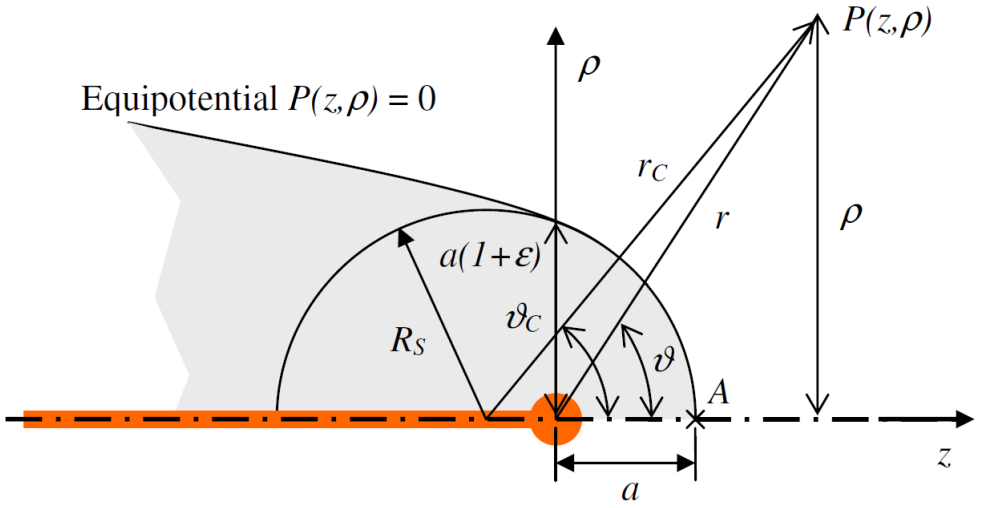

Figure 26: The cross section of the emitter tip model.

negative. These boundary conditions are leading to:

$$P(\rho, z) = q \left[\ln\left(\frac{r+z}{2a}\right) + \eta\left(1 - \frac{a}{r}\right)\right]. \tag{52}$$

The parameter a represents the axial distance between the emitter surface and the point charge Q_S. It depends on the parameter η, tip radius R_S and the value is calculated from:

$$a = R_S \frac{\eta + 0.5}{\eta + 1}, \tag{53}$$

where η is given by:

$$\eta = \left(1 + \frac{1}{\varepsilon}\right) \ln\left(\frac{2}{1+\varepsilon}\right). \tag{54}$$

The dimensionless parameter ε defines the geometrical shape of the equipotential line $P(\rho, z) = 0$ and so the shape of the tip surface. The value of the parameter ε can vary in the range $(0, 1\rangle$. The equipotential line for arbitrary value of potential P =const. is given by relation:

$$\cos^2\left(\frac{\vartheta}{2}\right) = \frac{a}{r}\left[\frac{P}{q} - \eta\left(1 - \frac{a}{r}\right)\right].$$

Shapes of the surface boundary lines in the vicinity of the tip for several values of ε are shown in Figure 26. The dark area in the image background encloses the shape of the commercially available $\langle 100\rangle$ Denka field emitter with radius R_S = 105nm. The best fit is obtained for $\varepsilon = 0.75$. A few equipotential lines for the same ε value are shown in Figure 28.

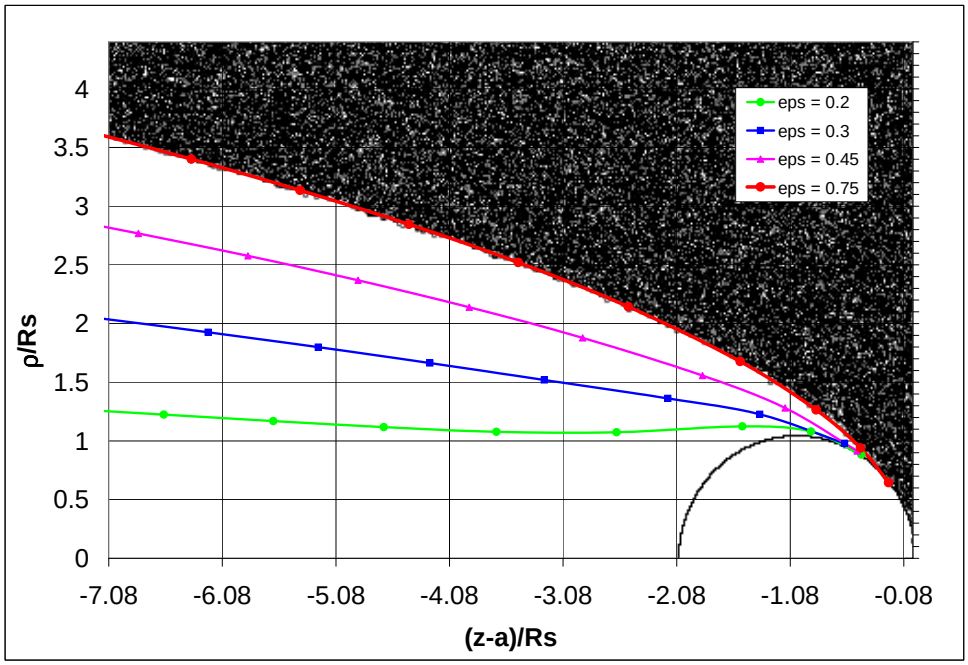

Figure 27: The surface boundary lines for several values of epsilon drawn on a part of the cold field emitter micro graph.

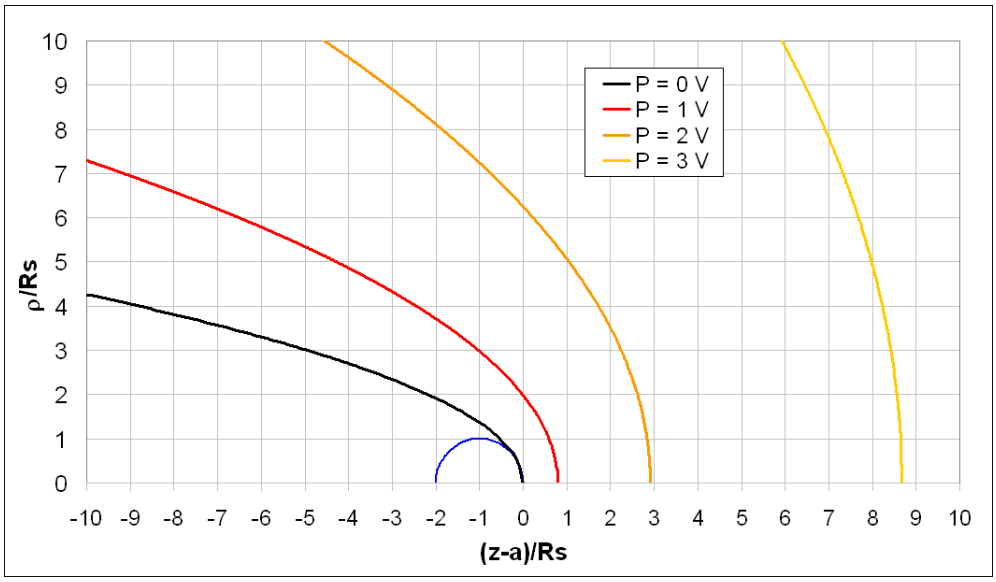

Figure 28: Equipotential lines for an emiter with shape parameter $\varepsilon = 0.75$.

Although the fit of the model to the tip shape is sufficient, the effect of the farther part of the emitter shank on the potential distribution is oversimplified and no extracting electrode is implemented yet. This shortcoming is corrected in the next step.

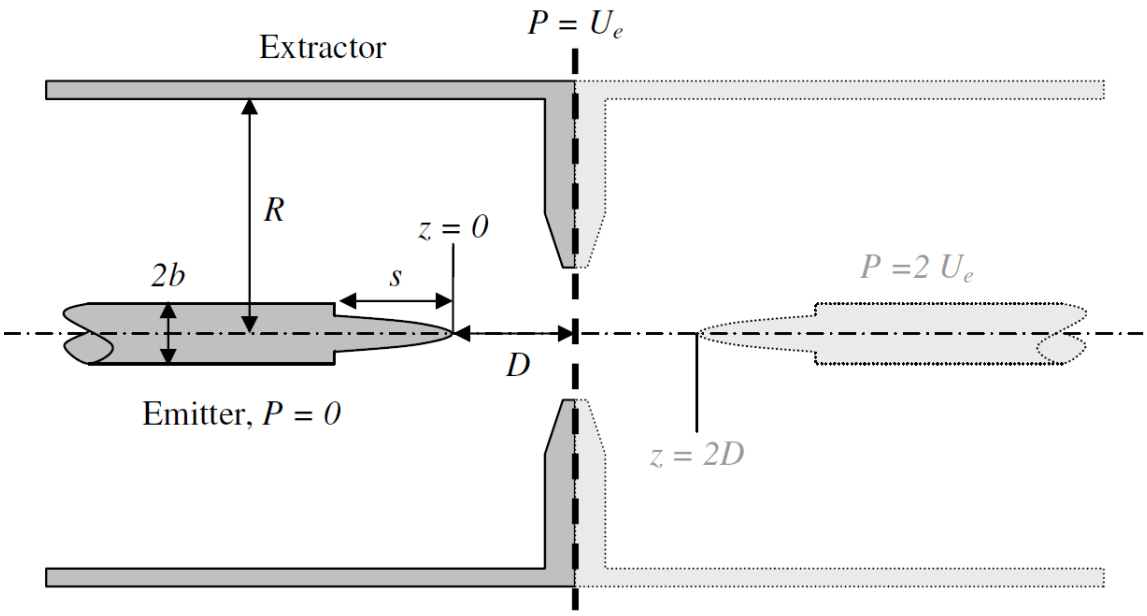

Figure 29: The diode model using the method of mirror charges.

A simple diode configuration is shown in Figure 29. A cylindrical tube of radius b, with the charge per unit q', substitutes the emitter shank. The tube extends the above defined model of the tip apex. The extraction electrode is implemented as another coaxial screening tube of radius R with a flat side cap, which is defined by the boundary condition $P(\rho, z_{ex}) = U_{ex}$. The potential $P(\rho, z \to -\infty)$ has to be equal to the potential of the cylinder capacitor defined by the emitter shank and the extractor tubes.
The model makes use of the following charges:

- A point charge Q_S at $z = 0$ and its mirror image at $z = 2D$
- A line charge q extending from $z = -s$ to $z = -\infty$ and its mirror image
- A line charge q' between $z = -s$ and $z = 0$ and its mirror image
- A charged tube with charge per unit length of $-q$ and its mirror image

The diode-like field distribution is achieved by creating of a mirror image of the model charges, using the extractor as the mirror plane. In order to get the full analytical expression for the potential, the extractor bore has to be neglected. if D is the distance of the extractor plane to the point charge Q_S in the origin of coordinate system, the potential is obtained from the following equation:

$$P\left(z,\rho\right) = P_0\left(z,\rho\right) + U_{ex} - P_0\left(2D - z,\rho\right), \tag{55}$$

with the potential distribution P_0 given by:

$$\begin{aligned} P_0(z,\rho) = q\,\ln\frac{z+\sqrt{z^2+\rho^2}}{R} + (q'-q)\ln\frac{(z+s)+\sqrt{(z+s)^2+\rho^2}}{R} \\ - q'\,\ln\frac{(z+s)+\sqrt{(z+s)^2+R^2}}{R} + \frac{Q_S}{\sqrt{z^2+\rho^2}} \end{aligned} \tag{56}$$

The charges Q_S, q and q' are determined from the boundary conditions:

$$q' = \frac{U_{ex}}{2\ln(\frac{R}{b})}, \tag{57}$$

$$q = \frac{U_{ex}}{g}\left[1 - \frac{g'}{2ln(\frac{R}{b})}\right], \tag{58}$$

$$g \approx \eta + \ln\left(\frac{2D\,s}{(2D+s)\,a}\right), \tag{59}$$

$$g' = ln\frac{1+\sqrt{1+R^2/s^2}}{1+\sqrt{1+R^2/(2D+s)^2}}. \tag{60}$$

$$Q_s = -\eta\, q\, a \tag{61}$$

The line charge densities q, q' and the factors g, g' satisfy the relation:

$$U_{ex} = q \cdot g + q' \cdot g' \tag{62}$$

The value of electrostatic field $\vec{E}$ required by the equation of motion at any point of the model is given by:

$$\vec{E} = -\nabla\vec{P} \tag{63}$$

The particular field components required in the equation of motion (45) are given by the partial derivative of the potential function $\vec{P}(z,\rho)$ with respect to z and ρ:

$$\begin{aligned}\frac{\partial}{\partial z}\vec{P} = &-\frac{q'}{\sqrt{R^2+(2D+s-z)^2}} + \frac{-q+q'}{\sqrt{\rho^2+(2D+s-z)^2}} - \frac{Q_s z}{(\rho^2+z^2)^{3/2}} + \frac{q}{\sqrt{\rho^2+z^2}} \\ &+ \frac{Q_s(-2D+z)}{(\rho^2+(-2D+z)^2)^{3/2}} + \frac{q}{\sqrt{\rho^2+(-2D+z)^2}} - \frac{q'}{\sqrt{R^2+(s+z)^2}} + \frac{-q+q'}{\sqrt{\rho^2+(s+z)^2}},\end{aligned} \tag{64}$$

$$\begin{aligned}\frac{\partial}{\partial \rho}\vec{P} = &\frac{(q-q')\rho}{\sqrt{\rho^2+(2D+s-z)^2}\,(2D+s+\sqrt{\rho^2+(2D+s-z)^2}-z)} - \frac{Q_s\rho}{(\rho^2+z^2)^{3/2}} \\ &+ \frac{Q_s\rho}{(\rho^2+(-2D+z)^2)^{3/2}} - \frac{q\rho}{\sqrt{\rho^2+(-2D+z)^2}\,(2D-z+\sqrt{\rho^2+(-2D+z)^2})} \\ &+ \frac{(-q+q')\rho}{\sqrt{\rho^2+(s+z)^2}\,(s+z+\sqrt{\rho^2+(s+z)^2})} + \frac{q\rho}{\rho^2+z(z+\sqrt{\rho^2+z^2})}.\end{aligned} \tag{65}$$

The big advantage of this model are significantly lower computational demands and very smooth potential distribution in comparison with a FEM model. As a major drawback the model can describe the diode system only, i.e. the suppressor electrode is not included. According to [2], the absence of the extractor bore is not critical. This analytical model was compared with a numerically simulated "exact" mesh model. The error in trajectories was only a few percent. This is explained as follows: Close to the tip, where the electrons are

slow and the trajectories are bended strongly is the electrostatic filed precise, because the effect of the extractor bore is small here. Although the field around the (non-existing) bore is not very precise, the effect on the trajectories is small there, because the electrons are already quite fast.

Three models with tip radius 50, 100 and 200nm were prepared. The simulations were performed for angular intensity values of 50, 100, 200, 300 and 400 μA/s for all three tip radii with following configuration: The shape parameter ε was adjusted on a micrograph of a typical Denka field emitter to $\varepsilon = 0.75$. The thickness of the emitter shaft was set to $b = 0.15$mm. The tip length $s = 0.534$mm was measured using a microscope. The parameter R was set to 100mm and the distance to the extractor plane was set to 1mm. The emitter was virtually operated at 300K with work function of 4.5eV.

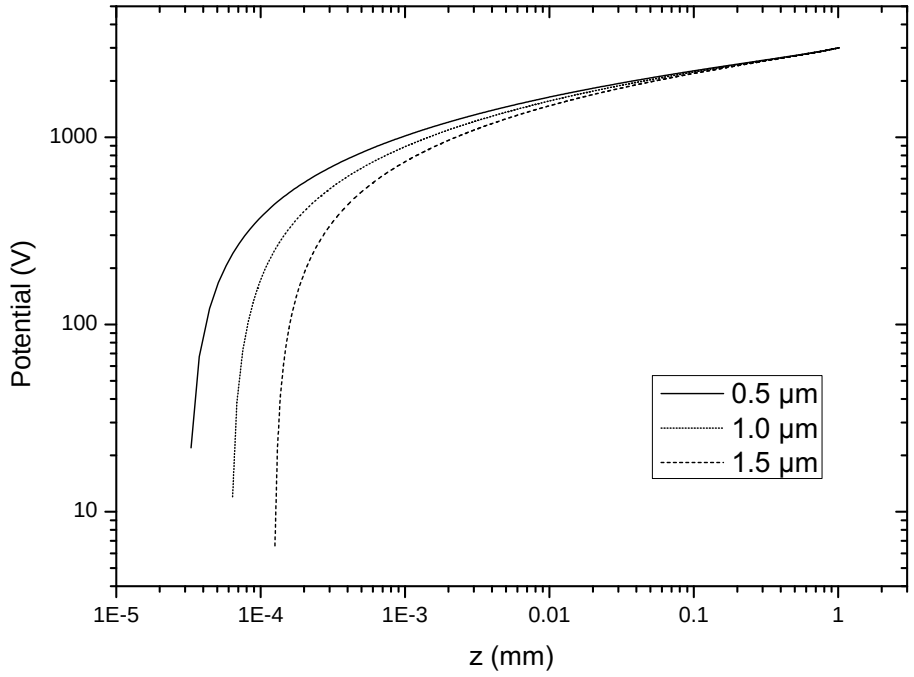

Figure 30: The axial potential distribution for all three radii of emitter at extractor potential $U_{EX} = 3000V$.

4.3.2 The field on the surface and the current density

Although the calculation of the electrostatic field is much simpler and accordingly faster, the evaluation of the interaction effects is equally time-consuming and fills up about 90% of the computing time. The size of the emission area and herewith the number of ray-traced particles for individual emission currents has to be carefully selected. Due to the almost spherical end of the tip is for the further generation of particle initial data more convenient to define the emission area in terms of the angle of the area edge with respect to the emitter axis. We estimated the angle roughly to 16° from an emission pattern of the Denka emiter which was operated in similar configuration as defined in the model description.

Also in the case of the rounded tip is the strength of the field at the surface changing with the distance from the apex center, but the differences are due to the absence of the faceting

small. Contrary to the faceted emitter is the maximal value of the electrostatic field on the axis of the tip. The electrostatic field strength can be easily obtained from equations (64) and (65). The respective current density is calculated with equation (18). The difference between the maximal and the minimal electrostatic field value of the emission area limited by 16° half-angle is in the worst case, i.e. the smallest radius and the highest simulated emission current, only 1.28%. It results in the difference of the current density of 21%. Nevertheless, the change in the energy distribution of emitted electrons is negligible and the current density distribution on the emission area is only slightly affected. The appropriate distribution function for the generator of random initial positions is derived in the same manner like in the case of the Schottky emitter.

4.3.3 The initial energy and angular distribution

The emission of the electrons in the case of the cold field emitter is driven mainly by the high electrostatic field. According to the emission theory in section 2.3, the initial energy distribution calculated is given by equation (25). It applies to the whole range of simulated emission currents. The procedure for the generation of the TED for initial data is almost identical to the procedure used for the Schottky emitter, except the analytical method of calculation of the electrostatic field value. It takes into account the differences in the field strength on the emitter surface and uses the barrier model proposed for the generation of the initial data for the Schottky emitter simulation, as described in section 4.2.3.

The strong extraction field affects the initial angular distribution of electrons significantly. The emission angles are generated using an identical procedure as in the case of the Schottky emitter. The polar angular distribution is calculated with the use of the equation (17) and the azimuthal angle is randomly generated between 0 and 2π radians.

5 Results

5.1 The Schottky emitter

Although some initial data were partially described above, all important parameters are summarized here.

The simulation was performed for three tip radii of the Schottky TFE emitter: $0.5, 1.0$ and $1.5\mu m$. The radius of the flat facet was 0.6 of the tip radius. The operational temperature was set to 1800K. The work function was 2.8eV. Used potential at the suppressor was -300V and the initial beam energy was set to 0V. These values were preserved in all configurations of the simulations.

5.1.1 Angular intensity and half-opening angle

The voltage at the extractor electrode was adjusted to values on which the five particular beam angular intensities should be achieved: 50, 100, 200, 300 and 400 $\mu A/sr$. A precise adjustment of the extractor voltage is not trivial. Although it has been done according to the procedure described in section 4.1.3, the variance of the estimated points and electron loses caused by the effect of the coulomb interactions resulted in slightly lower angular intensity values, especially at higher current densities. The Figure 31 shows the pre-calculated dependence of the angular intensity on the potential at the extractor.

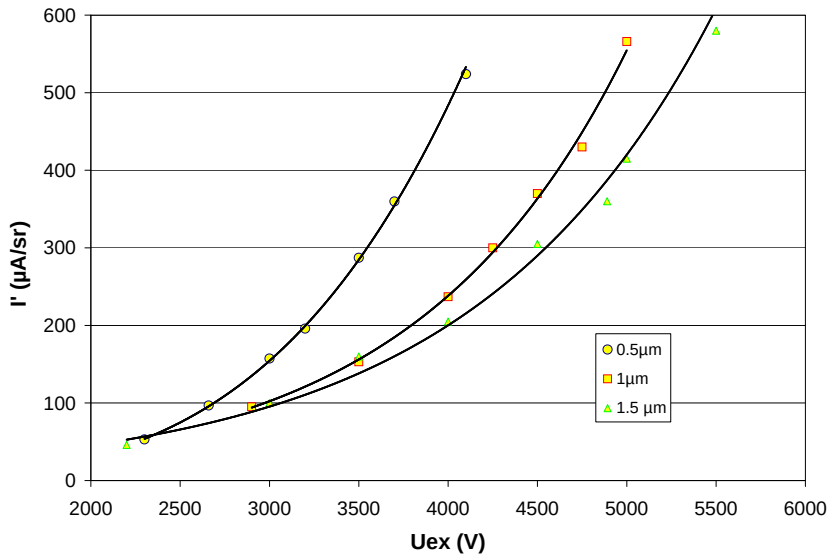

Figure 31: The dependence of the angular intensity on the potential at the extractor electrode for all three radii. The required values of angular intensity were interpolated from the black trend line.

As already mentioned, for practical reasons, not all emitted electrons passing through the extractor hole are interesting for the analysis of the beam properties. The beam is at a distance about few millimeter after the extractor usually limited by a small aperture. The

size of the opening is in the range of ten up to few tens of micrometers. By an introduction of such an aperture into simulation we would lose an absolute majority of the electrons for the evaluation of the results. The number of remaining electrons would be insufficient for a meaningful analysis. Fortunately the slow variation of the beam parameters near the axis allows the selection of a more reasonable half-opening angle for the evaluation. The Figure 32 shows a dependence of the angular intensity on the half-opening angle in a screen plane at the distance 1mm from the tip of the emitter, i.e. few micrometers behind the extractor.

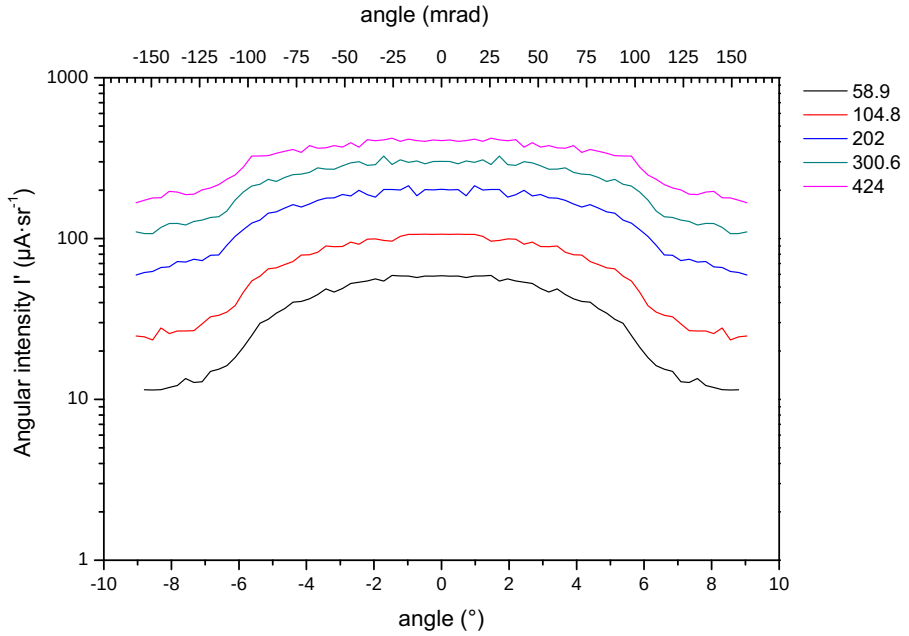

Figure 32: The dependence of the angular intensity on the distance from the axis defined by the varying half-opening angle in the screen plane $z = 1mm$ for the emitter with radius $1\mu m$.

The values are near the optical axis sufficiently stable up to 1.5° for lower angular intensities and up to 2° for higher angular intensities. The half-opening angle limiting the beam diameter for the analysis of the simulated beam energy spread and also the size of the virtual source was within this range.

5.1.2 The energy spread

The energy spread is measured as FWHM of a curve fitted to the histogram of particle energies. The calculated number of particles was not sufficient for construction of a smooth histogram. Histograms were frequently noisy, particularly near their maximum. The FWHM value strongly depends on the position of the fitted maximum. A small difference in the maximum value is directly translated as a change of the measured width. In some cases, it was necessary to use an averaging over a number of histogram fit functions with a varying histogram bin size or use a completely different fit method. The simultaneously calculated FW50 measure gave us more reliable results than the FWHM, especially for a lower number of

particles in the analyzed sample. However, the FWHM is more suitable for direct comparison with the experimental data.

The first interesting information is the initial energy spread of emitted electrons. The effect of the higher field at the edge of the flat facet on the current density and partially on the initial energy distribution has been already shown, see fig. 23. In particular, the differences in the energy width of the electrons starting from the center of the flat facet and its edge in the calculated example at 200μA/sr are 0.13, 0.07 and 0.05eV (FWHM) for radii 0.5, 1.0 and 1.5μm, respectively. But the difference in the width of those energy distributions alone is not the main contribution to the total initial energy width of all starting electrons. The distributions show, beyond the changed energy width, also a significant shift in energy with respect to the origin of the energy scale. The resulting width of TED for all emitted electrons is almost 0.66eV compared to 0.42eV FWHM width of distribution calculated with axial field value only.

Operating the emitter at various angular intensities is naturally reflected into different initial TED. The Figure 33 shows an example of initial TED for emitter with radius 0.5μm at several values of angular intensity and the Figure 34 shows initial TED of all emitted electrons for all three simulated emitter radii over several angular intensity values. The energy width is higher for emitters with smaller radii due to the higher field differences on the facet, which are related to the emitter radius.

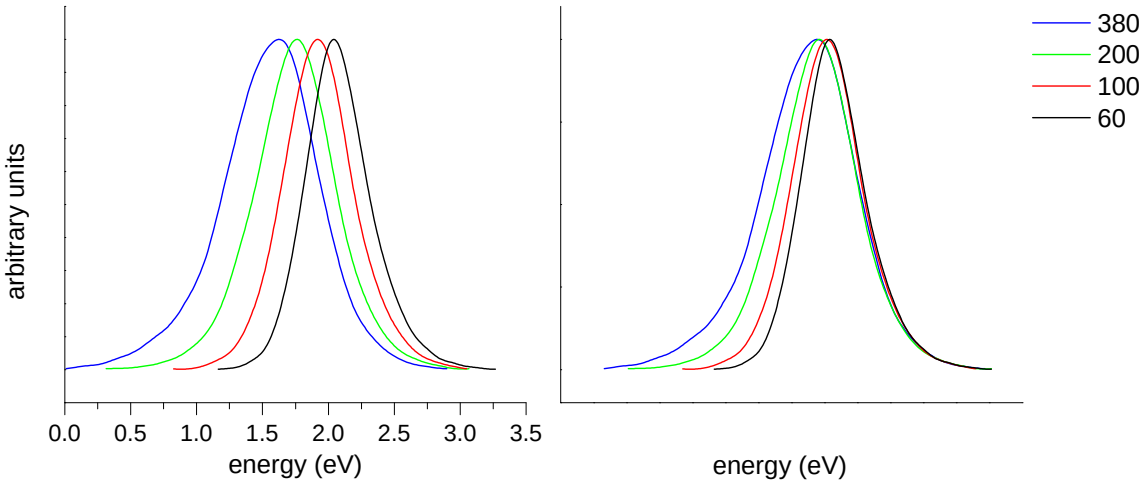

Figure 33: Generated initial total energy distributions for emitter with $r = 0.5\mu$m at I' in the range of 60 – 380μA/sr. The distribution curves were normalized. The left graph shows their shift in energy scale. The right graph shows the distributions shifted for better comparison of their shape.

The initial TED of all emitted electrons does not tell us much about the TED of electrons selected by an aperture behind the extractor plane. This information can be obtained from the simulation. Every simulation was performed 2 times. The first ray-tracing was done without taking the interactions into account. In this mode also the time distribution of the emission could be omitted, which makes the calculation significantly faster. In the second run were simulated identical initial data with the regular emission in time, accounting the coulomb interaction effects. Sixteen screen planes were defined at fixed positions from 0.5 to

1010μm along the z axis, with the origin at the apex of the tip. During the ray-tracing were for every particle crossing a screen plane recorded their actual parameters like the position, the velocity, the energy, the local field value, the total flight time and the trajectory slope. For every screen plane a separate log file was created. The Figure 35 shows three dependencies

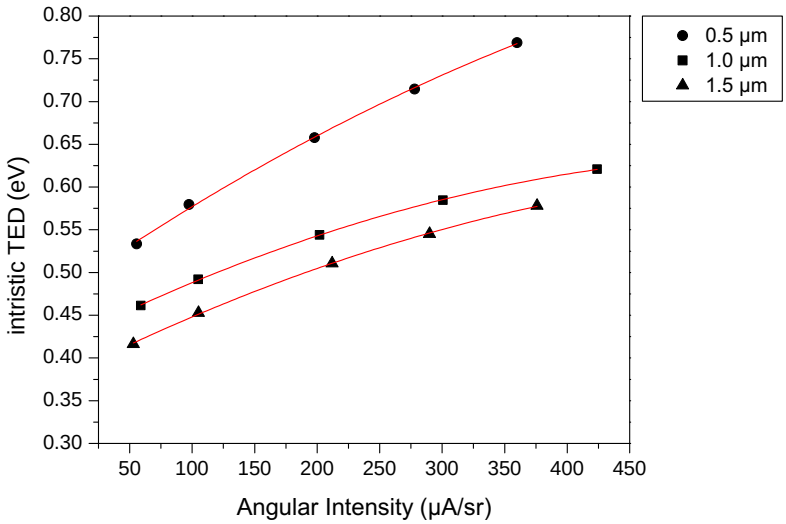

Figure 34: The dependence of calculated energy width of all emitted electrons for emitter radius 0.5, 1.0 and 1.5μm on angular intensity.

of calculated energy width for the emitter with radius 0.5μm. The black line is the initial TED of all generated electrons. The blue line is the energy width of axial electrons only and the red line is the energy width of electrons selected under 1° half angle at the screen plane $z = 1mm$.

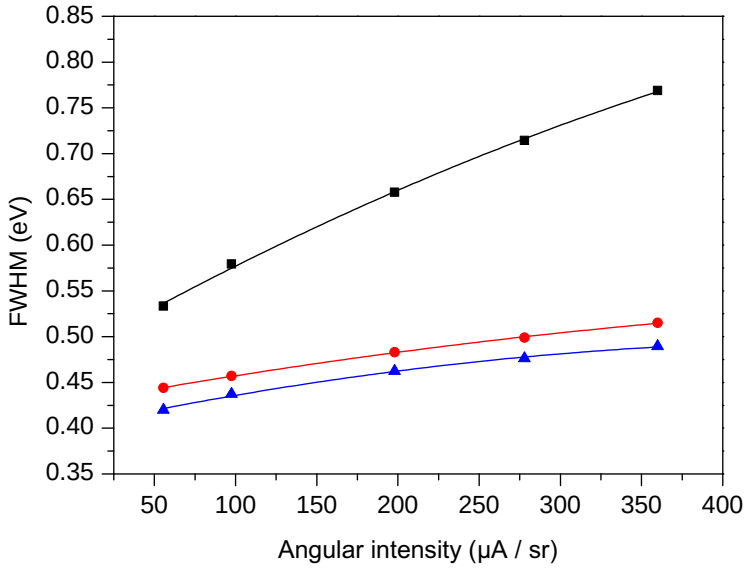

Figure 35: The dependence of calculated energy width on angular intensity for emitter radius 0.5μm. The individual curves are related to different selection of analyzed electrons.

The difference between the initial energy width of axial electrons and the energy width of ray-traced electrons (without interaction effects) when it was recorded under the selected half-opening angle is only 0.025eV in average. Compared to the presented high initial energy spread of all emitter electrons it does not look significant. Nevertheless, also such a relatively small difference heps us later to evaluate the relation among the initial energy spread, the total energy spread and the energy broadening more precisely. The electrons starting from the area near the edge of the facet apparently do not contribute directly to the total current and therefore to the energy width of the beam limited by the aperture. The map of the initial positions of the captured electrons is shown on Figure 36. The electrons passing through the aperture are coming only from a relatively small area near the axis.

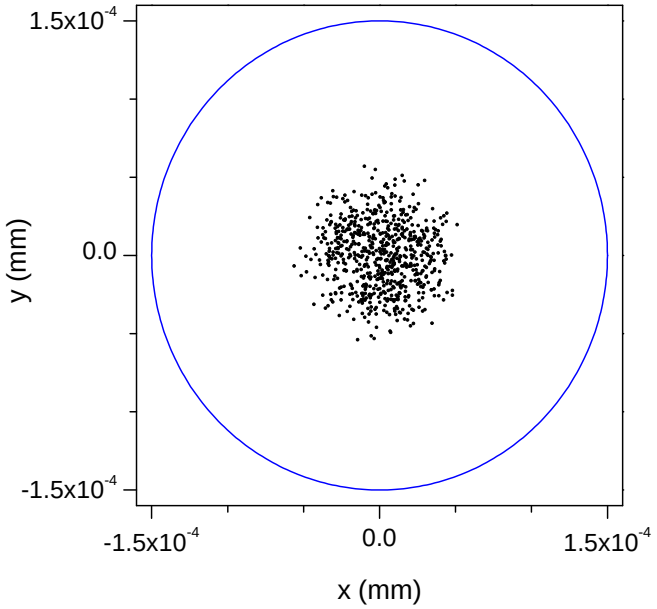

Figure 36: The initial positions of electrons traced through the system without calculation of mutual interactions. Tip radius is 0.5μm and angular intensity 200μA/sr. The blue circle represents the edge of the flat facet.

The following figures show the evolution of the energy width measured as FWHM and FW50 along the z axis for several values of the angular intensity. The individual points in the graph represents measured values in a particular screen plane. An imaginary aperture behind the extractor plane defines a reference half-opening angle for the analysis. The limiting angle was in every screen plane individually adjusted in order to achieve equal number of electrons in the evaluated sample.

In Figure 37 and 38 are shown results from simulations performed without and also with the calculation of mutual interactions among ray-traced electrons. The data are for the tip radius 0.5μm. In the first case remains the intrinsic value of the beam energy width practically unchanged along the whole trajectory length. In the second case is a gradual growth of the energy width due to the electron-electron interactions effects clearly visible. It is naturally more pronounced at higher emission currents, but already at the lowest simulated angular intensities is a weak energy broadening observable. Although the logarithmic scale of the horizontal axis does not display the rapid growth of the energy spread in the first

50μm so dramatically, it can be seen that the most of the broadening already took place there and further growth of the energy width is very slow.

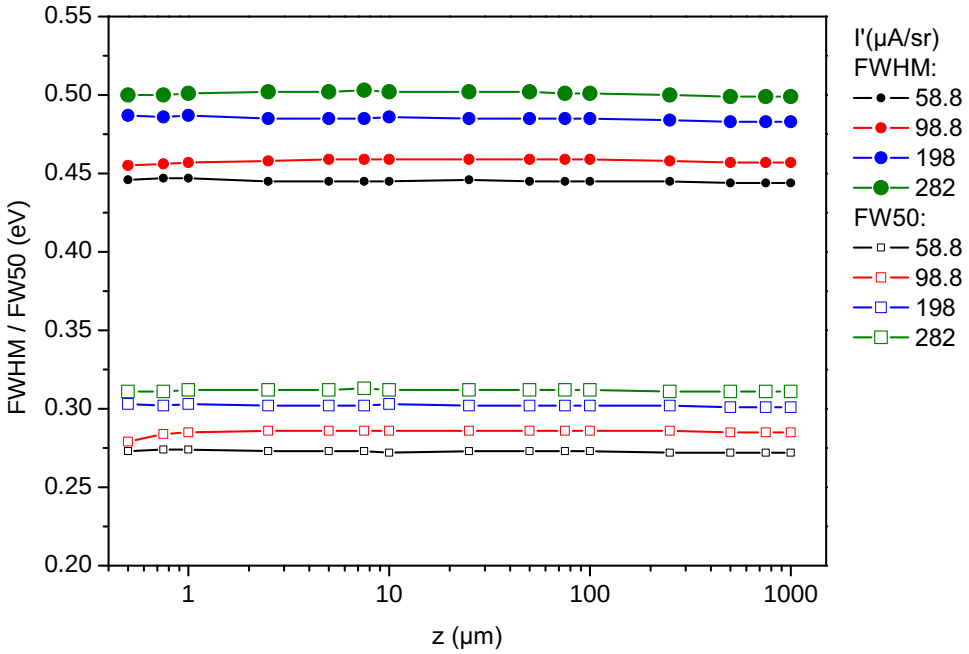

Figure 37: The evolution of the energy width for the tip with radius 0.5μm without accounting of mutual interactions.

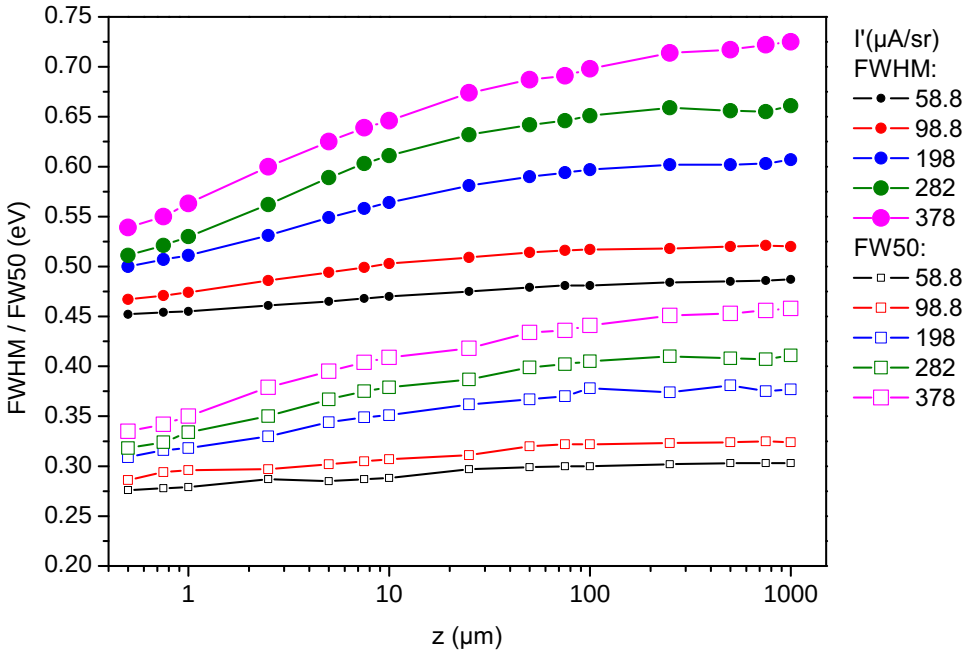

Figure 38: The evolution of the energy width for the tip with radius 0.5μm with accounting of mutual interactions

Similar procedure was repeated also for the other two tip sizes. The comparison of absolute values of the TED among simulated emitters with different tip radii shows in Figure 39 that the larger emitters have lower total energy spread at the same angular intensity.

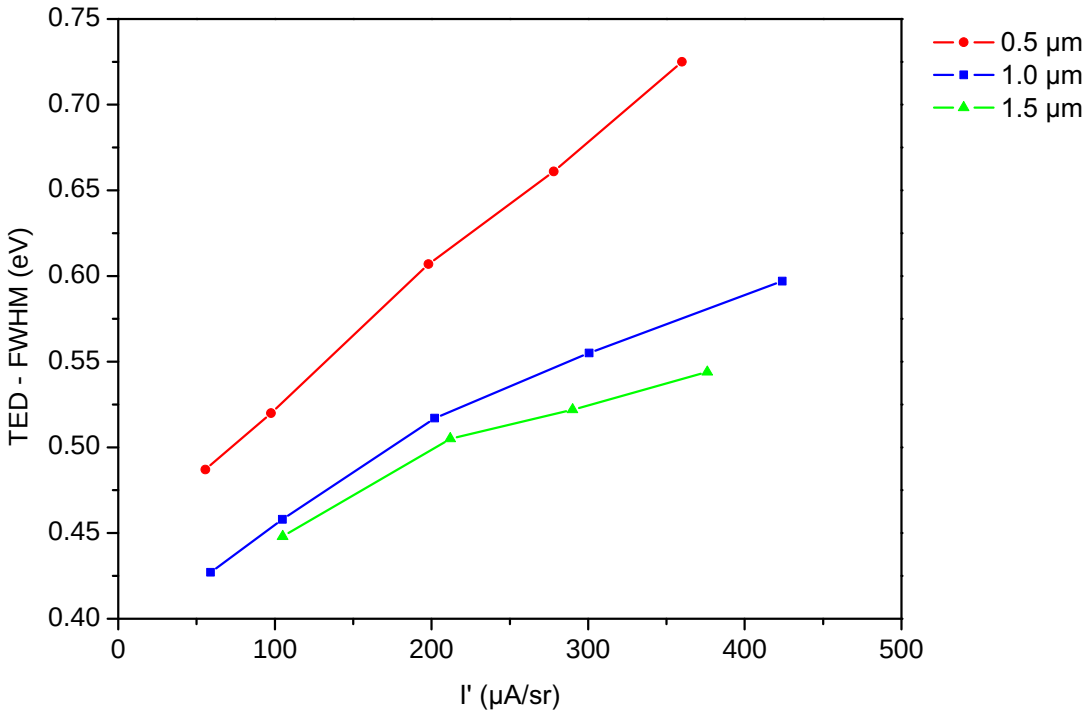

Figure 39: The resulting FWHM energy width versus angular intensity for all three tip radii at z = 1mm.

5.1.3 The comparison of calculated energy width with the experimental data.

A comparison of the simulation results with the published experimental data is not at all straightforward. Among the number of available papers about the Schottky emitter one has to find experiments with similar aims and useful results. The papers are usually focused on the evaluation of the practical emitter performance and only occasionally also on the coulomb interaction effects. Frequently emitters are studied with different chemical activation, mechanical configuration or with very special parameters like significantly higher or lower operational temperature than it is usual; often very high emission currents are used. Even the most similar cases have some minor variations in the the configuration of surrounding electrodes and the tip radius. The best experimental data for the comparison with the simulation would be from the measurements with the emitter, which served as a model for the simulation, but in order to achieve the required precision a special equipment would be needed. An inverse approach, i.e. the creation of a simulation model in line with already published experiments is due to incomplete informations about the emitter dimensions or operational parameters impossible.

Comparable experimental data for the Schottky emitter with similar parameters were published in the the paper by Sakawa et al. [5], by Schwind et al.[16], by Fransen et al.[10]

and by Kim et al.[12]. In their studies a practical performance of the Schottky emitter is examined and energy broadening effects are briefly discussed. The used tip radii are not identical with the radii in the simulation, but they are close enough for a reasonable comparison. Other operational parameters and also the mechanical arrangement of the suppressor and the extractor are also very similar, since the evaluated emitters actually are or were based on commercially available sources, mostly produced by FEI. The experimental results as well as the simulation results have a limited accuracy, but present trends should correspond to each other in general. In this work is the comparison confined to the results published in [5] and [16].

Sakawa et al. [5] evaluated electron energy spreads of emitters with tip radii of 0.43, 0.68, 1.1, 2.8 and 4.2μm. The parameters of the emitter mechanical configuration were similar, except for the size of the extractor hole, which was 0.6 mm - contrary to 0.4 mm - and the extractor distance of 0.6mm contrary to 0.76 mm used in our case. The energy width of the analyzed beam was measured with an energy analyzer. The half-opening angle was typically 5 mrad (0.3°). The measured data for relevant tip radii were extrapolated from the published figure and combined with appropriate simulation results into Figure 40.

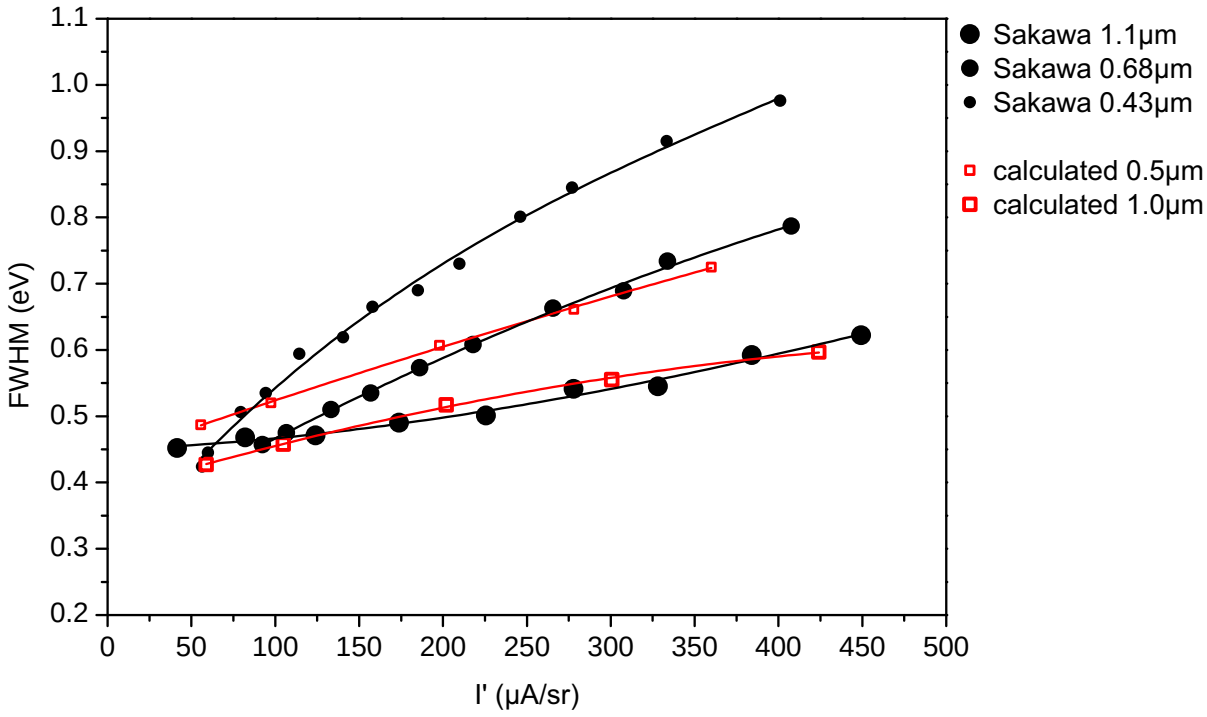

Figure 40: The comparison of calculated and measured FWHM values of the total energy distribution for tip radius 0.5 and 1.0μm. The measured values were extracted from [5].

Schwind et al. performed similar measurements of the FWHM energy width for the Schottky emitter with several tip radii. The hard-copy of the image presenting their results was used for the comparison with performed simulations for the tip radius 0.5 and 1.0μm. Figure 41 shows the dependence of the energy spread on the reduced angular intensity. The calculated data fits the measured values of the total energy spread in both comparisons reasonably well. The trend lines across the simulated values have slightly different slopes.

The measured energy width of the beam at lower angular intensity is narrower. The difference between the simulation results and the experimental data is roughly 0.05eV. The data for 1.1μm tip by Sakawa et al. [5] are an exception, but their trend clearly crosses the measured values for lower tip diameters, which does not look very probable. The presented

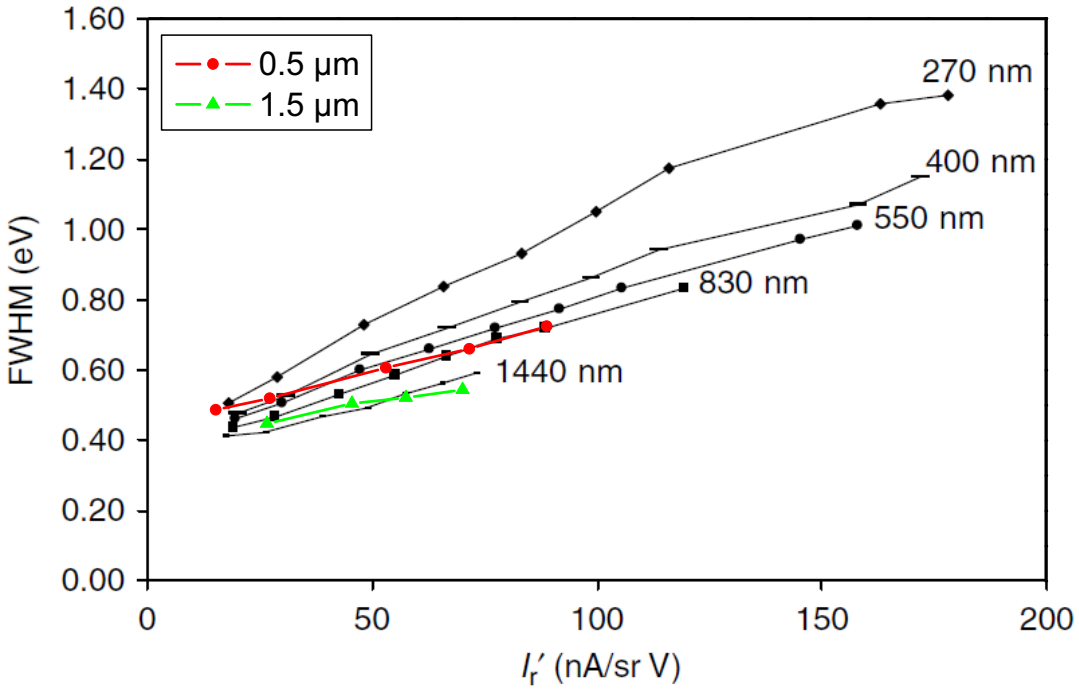

Figure 41: The comparison of calculated and measured FWHM values of the total energy distribution for tip radius 0.5 and 1.0μm. The original figure was published in [16].

experimental data perform at the lowest angular intensity partly better than theoretically expected. The similar inconsistency can be found also in Figure 42 published in [10] where Fransen et al. compared the experimental energy distributions published by Kim et al. [12] with theoretical expectations. The energy width of the distribution calculated with use of eq.(15) is at lower extraction fields broader than the measured spread. They did not pay attention to this difference. The same effect was observed also by Ohshima and Nishiyama [17]. In order to avoid the contribution of the field emission and the coulomb interaction effects, they measured the energy distributions of various Schottky emitters at very low operational currents. The measured difference in the FWHM of the measured and the theoretically expected energy spread was for the ZrO/W Schottky emitter 0.08eV. A new model using an effective mass approximation was introduced and the accordingly calculated energy width agreed with the experimental data. The effects affecting the emission process, discussed in [17], seem to be a reasonable explanation for the narrower energy distribution at low angular intensity also in our case.

The calculated FWHM values at high angular intensity are showing the opposite trends. They are lower than observed in experiment. The difference is roughly in the same range as at the lower I'. The reasons for this discrepancy in this case is partly the underestimation of the current density of the analytical emission model at higher extraction field values, recently

presented in [11], and probably for the most part the significantly shorter beam length in comparison with the experiment. In all experiments was the TED of the electron beam measured at the distance of several millimeters contrary to 1 mm screen distance in our simulation. The evolution of the calculated energy FWHM close to the screen plane shows a weak, but continuous increase. Hence, one can expect a further growth of the energy width also behind the extractor.

The electrons analyzed at more distant screen plane had more time to interact and the resulting energy width is consequently broader.

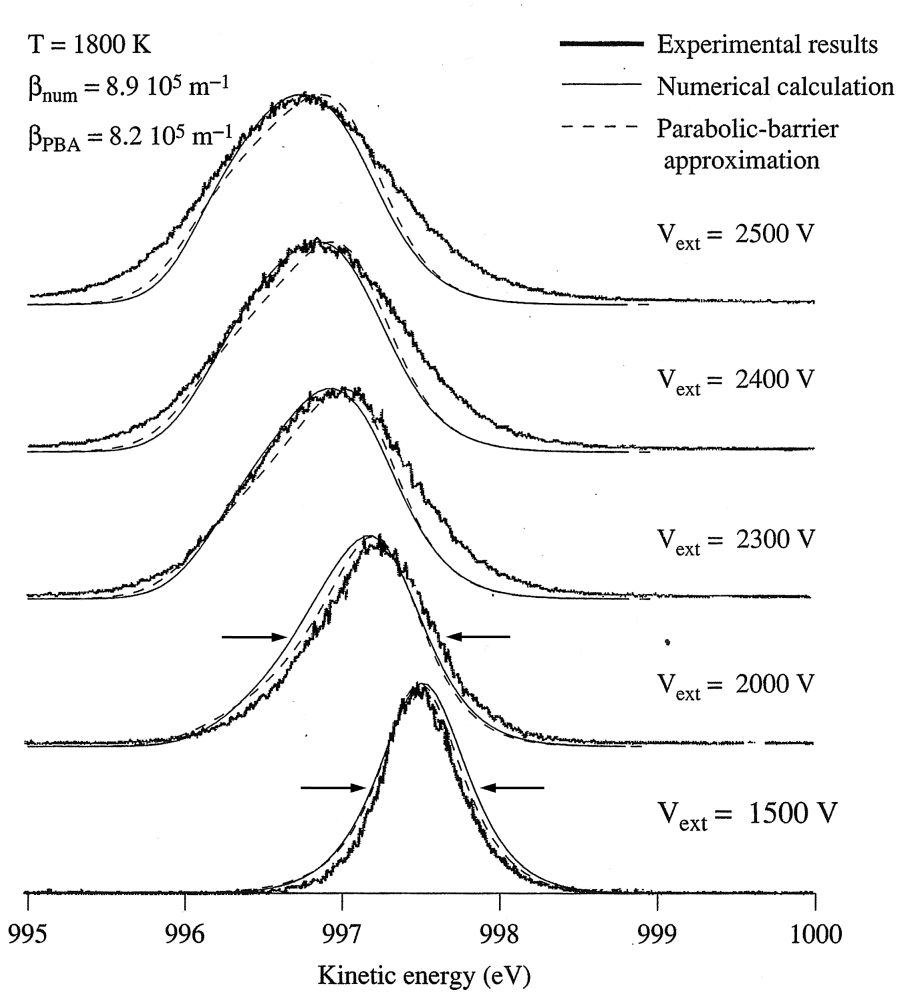

Figure 42: Energy distribution of a Schottky emitter with tip radius 0.3μm taken from the paper by Fransen et al. [10], Fig. 22. The emission theory predicts at lower extraction voltages a broader energy distribution than observed in the experiment.

5.1.4 The energy broadening and comparison with analytical models

Simulations on identical initial datasets allow us to extract the exact contribution of coulomb interaction effects to the energy broadening directly from the calculated output. From both simulation runs can the actual energy E of every corresponding particle pair under desired half-opening angle be compared and the difference dE can be recorded as the contribution from the interaction effects. A histogram of recorded energies discloses the energy distribution of the broadening. The spread of this distribution is measured using the same measures and methods as before.

The dependence of the energy broadening (FWHM) on the angular intensity for all three simulated tip radii is shown in Figure 45. Moreover, the higher energy spread for the emitter with the smallest radius gives also the strongest energy broadening, compared with other tip radii at the same angular intensity. The plots indicate less energy broadening for emitters with larger tip radius, but it is not completely correct. The larger emitters can achieve the same angular intensity values with lower current density just due to their larger emission surface. At the same current density level would an emitter with larger radius, according to the results in Fig. 43, suffer more from the interaction effects than the smaller one. To the same result came recently Bronsgeest et al. [3] after extracting the contribution of the energy broadening from their experimental measurements of the energy spread.

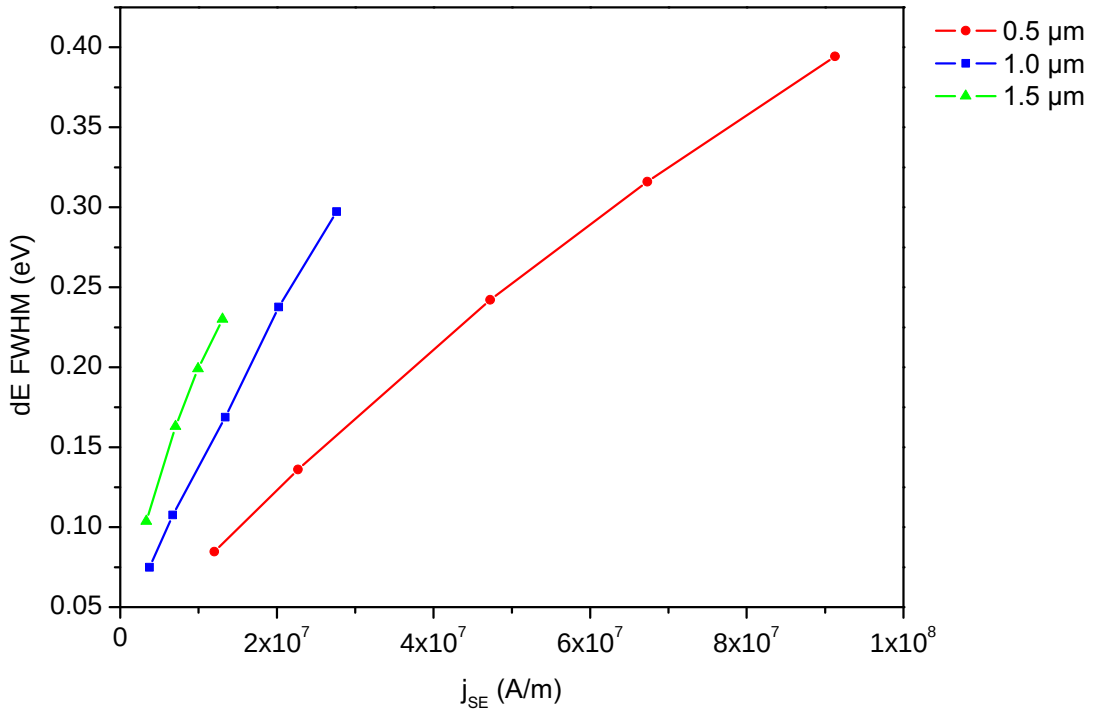

Figure 43: The dependence of calculated emitter energy broadening on the emission current density for all three emitter sizes.

Also Schwind et al. [16] attempted to extract from the experimental data the contribution of the Boersch effect to the total energy spread. They used a convolution of the initial energy distribution with a distribution function representing the contribution of the Boersch effect

and found the best fit to the experimental data. The convolution function for FW50 measure has following form [24]:

$$FW50_{Exp.} = (FW50^{\gamma}_{Int.} + FW50^{\gamma}_{Boersch})^{1/\gamma} \tag{66}$$

The best fit was obtained for the parameter $\gamma \approx 1.56$. The dependence of the measured total energy width, the theoretical intrinsic energy width and the extracted contribution of the coulomb interactions on the reduced angular intensity is shown in Figure 44. The original data were extrapolated from [16] and they are relevant for Schottky emitter with tip radius 0.55μm. Following the Schwind's approach, the exponent γ was recalculated from the extrapolated data presented in Figure 44. The indicated value of 1.56 could not be achieved. The calculated value was $\gamma \approx$0.76. Obviously some of the plots are wrong (also in [11]). Supposing that the experimental data, the intrinsic energy width and the calculated parameter γ are correct, new values corresponding to the coulomb interaction contribution were calculated. The corrected plot is outlined in the same figure with dashed line.

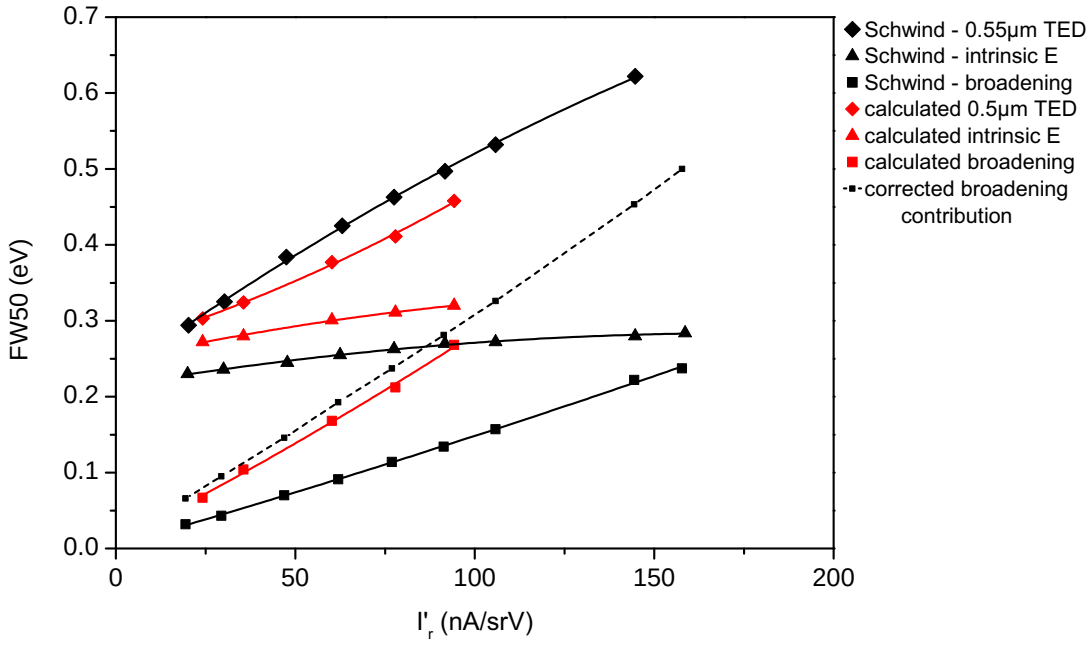

Figure 44: The extrapolated data from [16] with corrected plot for Boersch effect contribution in comparison with the simulation results.

Data in Figure 44 shown in red are the results from our simulations for emitter with tip radius 0.5μm. In our case was the resulting energy spread and the contribution of the coulomb interactions obtained directly from the simulation. The TED values are slightly lower than the experimental data, most likely due to the significantly shorter distance between the emitter tip and the plane of the detection. The intrinsic energy width was calculated using the procedure described in section 4.2.3. The initial energy width presented in [16] was apparently calculated using only the axial electrostatic field value. It was shown in section 5.1.2 that the electrons detected under particular beam half-opening angle originate from a small spot with nonzero radius on the emitter facete (see Fig.36). Their energy spread

is slightly higher, by 0.05eV, due to the increasing electrostatic field with the distance from the emitter axis. The difference is in practice negligible, but it clearly corresponds to the difference in Figure 44 and helps us to calculate the parameter γ more precisely. The contribution of the coulomb interactions corresponds well to the corrected plot. From the simulations results the parameter $\gamma \approx 1.655$ was evaluated.

In the overview of theoretical models in section 2.5 a set of analytical equations for calculating the FW50 and FWHM of the energy broadening was shown. The equations (37)–(40) derived by Jansen and Kruit [1] distinguish four individual beam regimes. For the calculation of energy broadening in a beam in an unknown regime is used equation (41), which combines the contributions of all individual regimes together. The evaluation of equations show that Gaussian and pencil beam regimes do not contribute to the final FWHM/FW50 value at all and that the addition of the contribution of Lorentzian regime deteriorate the resulting fit. Hence, for the purpose of the comparison with our simulation results, only the equation representing the Holtsmark regime was used. All values obtained from the equation were divided by a factor of two in order to adapt the equation for the emitter model according to the procedure of Fransen [10]. The dependence of calculated and simulated FWHM energy broadening on angular intensity is shown in Figure 45.

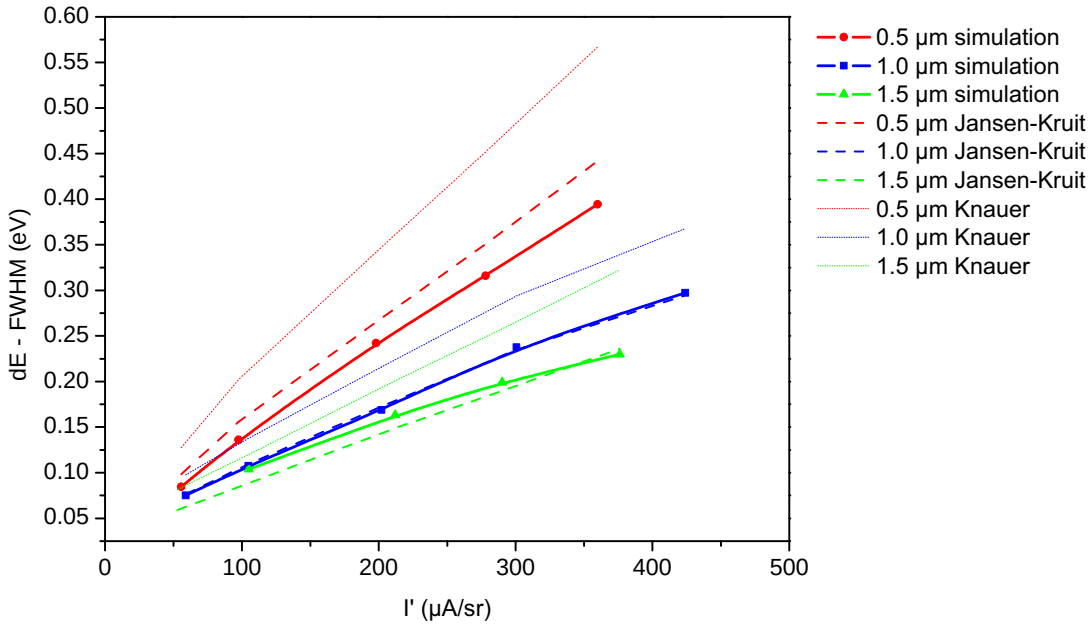

Figure 45: The comparison of the results from the simulations versus predicted values calculated from analytical approximations.

For the calculation of the analytical curves the following parameters were used: the total emitted current I according to the particular working point, the beam half-opening angle α in the range of 9.5° – 11.5° and for the crossover radius r_c, the radius of the whole emission area in case of theory of Jansen and the emitter tip radius for the formula by Knauer were selected.

Although the Fransen's approach is just a simple modification of the theoretical approximation, which is in general not suitable for the emitter area, the calculated curves

are in a relatively good agreement with the simulation results. The results are consistent with the 2/3 dependence of the energy broadening on the beam current (i.e. Holtsmark regime). The best fit is obtained for the tip with radius 1.0μm. The equation (38) could be used for the estimation of the Boersch effect contribution in this particular case. The differences for other radii are in the range of 0.02 – 0.05eV (FWHM). If the numerical factor in the equation and the exponents for crossover radius r_c and extraction voltage V are modified, a perfect fit to the simulation results of all three tip radii can be obtained. The modified equation is:

$$\Delta E_{FWHM\,H} = 675.6\,\frac{I^{2/3}}{r_c^{1/10}\,\alpha\,V^{1/2}}, \tag{67}$$

The values predicted by equation (35) proposed by Knauer are clearly overestimated. A simple adjustment of the numerical factor in the equation does not improve the situation. The strong dependence on the beam half-angle results in high differences among fit results for individual tip radii.

Schwind et al. determined that the dependence of the energy broadening contribution (FW50) on I' and form factor β, where $\beta = F/V_{ex}$, obey a simple power law function. In terms of tip radius r (since $\beta \propto r^{-0{,}67}$) was the function determined as:

$$\mathrm{FW50(Boersch)} \propto {I'}^{0.84}/r^{0.64}. \tag{68}$$

For the evaluation of the Boersch effect in the source region is such a dependence more relevant than analytical approximations presented in section 2.5. The equations (37)-(41) were derived for general beams where parameters like the total current, the beam potential, the beam half-opening angle and the size of the crossover are arbitrary, i.e. independent. In the case of a real emitter are the parameters always related to each other and consequently, they may be represented by single one in the evaluated dependence.

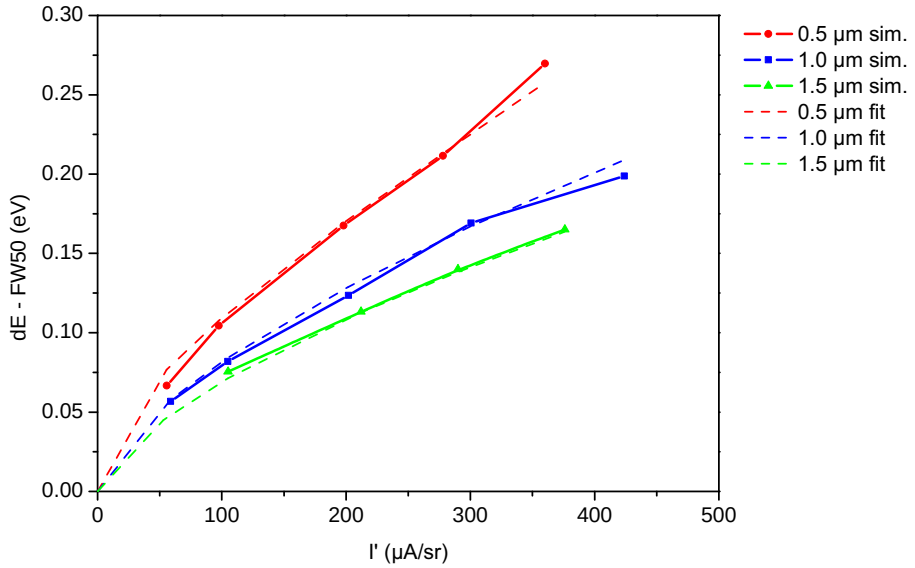

Figure 46: Fit of the simple power function (69) to the dependence of Boersch FW50 on I'.

Figure 46 shows the dependence of the simulated FW50 energy broadening on I'. The function fitted to the simulated data has the same form as function 68. The best fit was obtained for:

$$\mathrm{FW50(Boersch)} \propto I'^{\,0.65}/r^{0.4}. \tag{69}$$

The clear linear dependence of the Boersch FW50 to the fitted function is shown in Figure 47. The difference among the exponent values may have several reasons: The Boersch FW50 contribution calculated in [16] was extracted from the experimental data using other fit function, which may add some small error. The flat facet at the apex does not have necessarily the same size to the tip radius ratio. The determination of the tip radius has a limited precision. Also a slightly different dimensions and positions of surrounding electrodes and the total length of the beam may play some role.

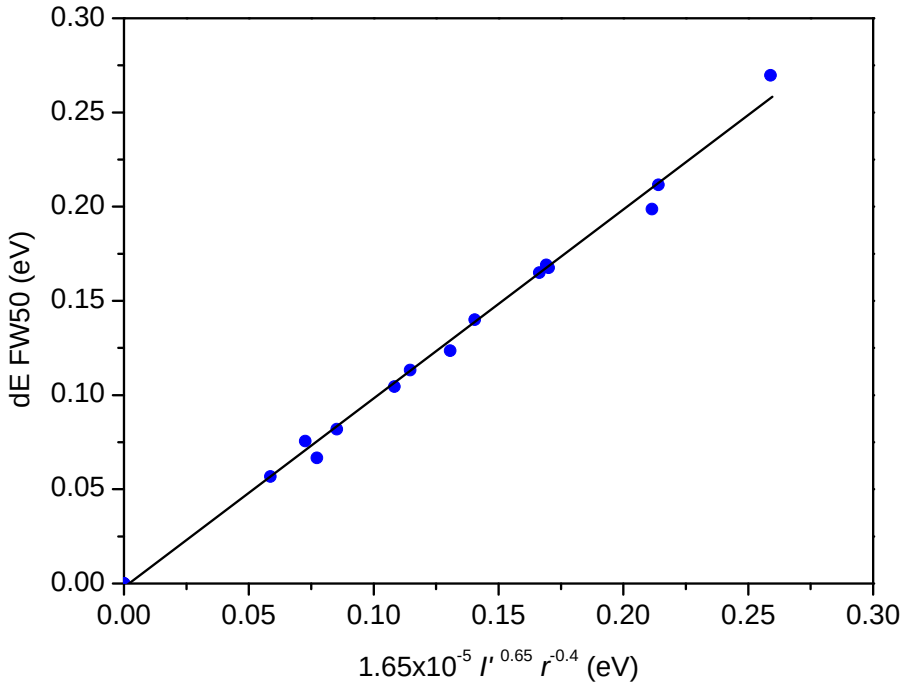

Figure 47: The Boersch FW50 versus the power function 69 shows a linear dependence.

5.1.5 The emitter brightness and the virtual source size

The reduced brightness of the source can be calculated using equation (30). The required parameters are the reduced angular intensity I'_r, i.e. the angular intensity divided by the beam potential, and the respective virtual source size d_v. All these parameters can be easily obtained from the simulation results.

The angular intensity values are known from the previous analysis. The size of the virtual source d_{v50} can be calculated using the procedure previously described in section 2.4. By the simple backtracking of electrons selected under specific half-opening angle from an arbitrary screen plane, a crossover is created near the emitter tip. With the help of an automatic evaluation routine for each emitter radius and working point was a plane of the smallest spot size found. The size of the spot was determined by the diameter containing the 50% of the current (FW50). This procedure was performed in every screen plane, in order to record the development of the virtual spot size of the beam along the distance from the tip. An example of such an evolution for emitters with all simulated radii at angular intensity 200μA/sr is shown in Figure 48. The calculated results are relatively noisy, because the beam limiting half-opening angle had to be a quite small, due to it's strong impact on the calculated source size d_{v50}. The analyzed angles were at the distance $z = 1$mm in the range of 0.6° – 1°, containing 1000 – 2000 particles. The figure shows an increase of the virtual

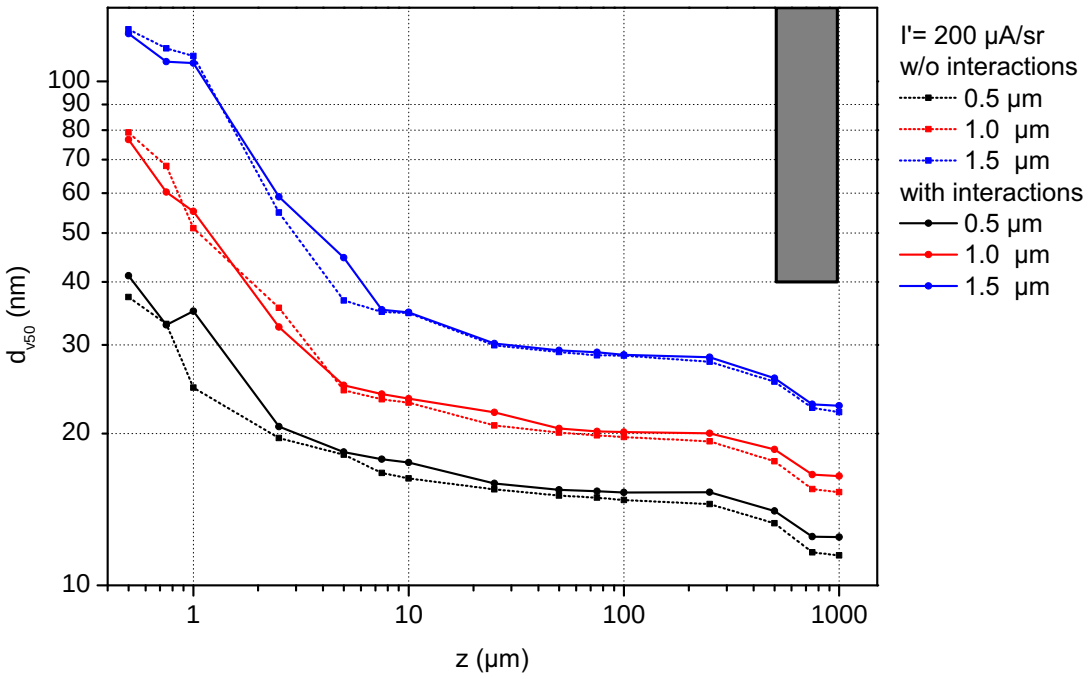

Figure 48: The evolution of the virtual source size with the distance from the tip at the angular intensity 200μA/sr. The gray rectangle represents the position and the thickness of the extractor.

source size with larger emitter radius. The size is substantially changing with the distance from the tip. The calculated values near the tip are very high, but they are rapidly reduced within few micrometers as the trajectories of emitted electrons are bended by the effect of

strong acceleration field. After 100μm are the values almost stabilized, but they are above 200μm again reduced by the effect of the electrostatic field of the extractor bore.

Also in the case of the virtual source are the results from the simulation runs with and without interaction effects directly comparable. The source size d_{v50} from each simulation run can be compared and the difference Δd_{v50} considered as the contribution of the interaction effects. Although the noise in the calculated data complicates the evaluation, a weak trend of the lateral, i.e. the size broadening can be noticed in the dependence presented in Figure 49 and right part of Figure 50.

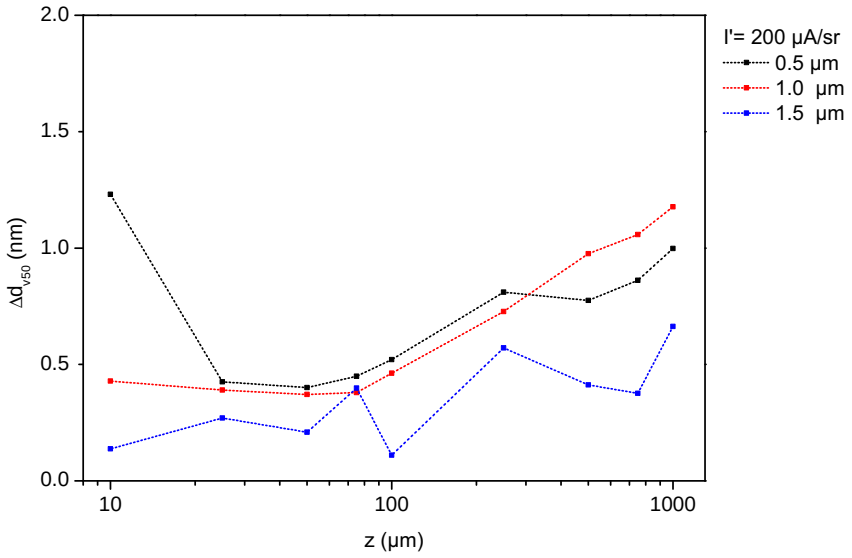

Figure 49: A possible broadening of the virtual source Δd_{v50} with the distance from the tip. $I' = 200\mu$A/sr.

The calculated dependence of the virtual source size on the angular intensity is presented in Figure 50. The variations of the source size are rather small. The simulation results provide a clear trend only for the emitter with tip radius 1.0μm, where the growing angular intensity shows lowering of the virtual source size.

In most publications is for the calculation of the virtual source size used Eq. (26). Comparing the calculated values provided by this equation with presented simulation results, one would find that the virtual source size expected from the analytical approximation is 2 – 3 times higher. This difference is surely the consequence of the oversimplified analytical approximation. The equation does not takes into account the impact of the flat facet at the tip apex, the suppressor lens and the extractor bore on the electrostatic field distribution in the emitter region.

A direct measurements of the virtual source size are rather seldom. A comparable experimental data can be found in paper by Beck [15]. He measured the virtual source size and the brightness of an emitter module with similar mechanical configuration and operational parameters. For the emitter with the tip radius 1.0μm he measured 17nm virtual source at 200 and 380μA/sr. This value corresponds with our simulation result.

In other papers [16] with similar measurements of the d_v one can be found results which are closer to the analytically predicted values. It does not mean that the simulation

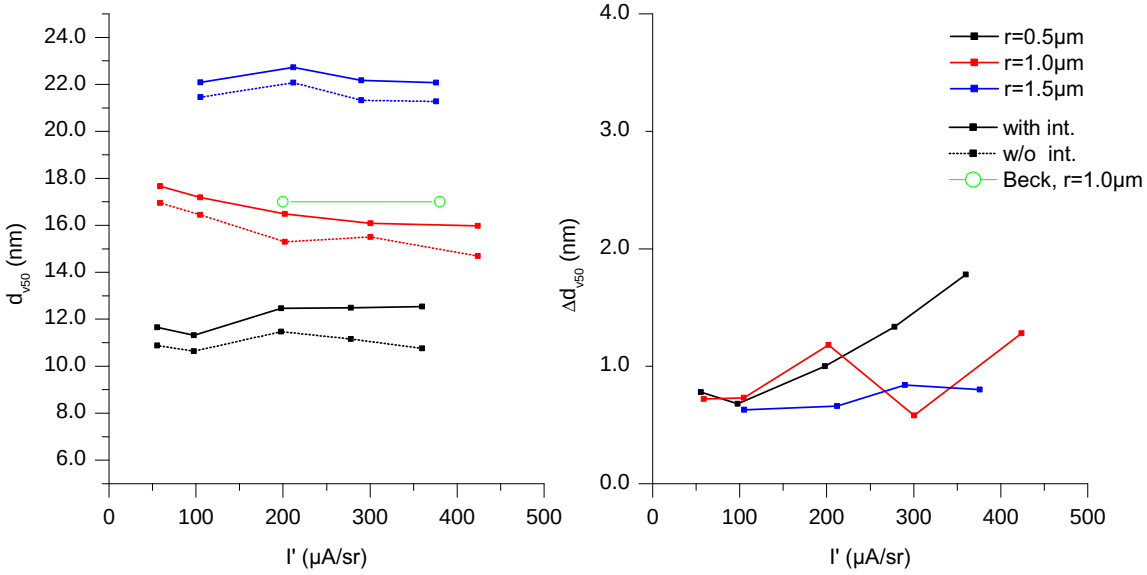

Figure 50: The resulting virtual source size and the broadening measured in the screen plane at $z = 1$mm in dependence on the angular intensity.

results are wrong. The virtual source size is a source parameter, which is sensitive to the mechanical configuration and the excitation of all electron-optic components. In our case is the screen plane defined directly above the extractor electrode in the field free area. Under that conditions works the extractor as a diverging lens. The size of the virtual source is compressed. In a real electron optical device like the electron microscope or the test set-up with the energy analyzer is the beam after the extractor plane again accelerated or decelerated. Both affects the virtual source size.

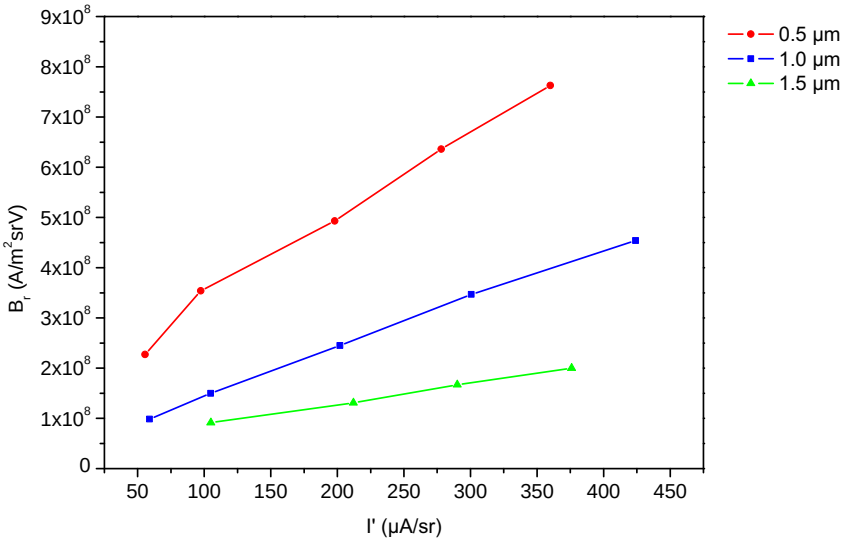

Figure 51: The reduced brightness B_r versus the angular intensity I' in the screen plane at $z = 1$mm.

All parameters required for the calculation of the reduced brightness are available now. Following Figure 51 plots the reduced brightness B_r on the angular intensity I'. The smaller emitter by the virtue of smaller d_{v50} provides naturally higher brightness at the same angular intensity than larger emitters.

The difference in achieved brightness values is even growing with higher values of I'. The plot in Figure 52 shows that, if the brightness is the most important parameter, the relatively lower energy spread does not provide the large emitters an advantage in the performance over the smaller one. The effect of the lateral broadening on the virtual source size and herewith on brightness is due to high noise in the simulation results still in question. In general, it is small. Some of the calculated results are summarized in the Table 2, 3 and 4.

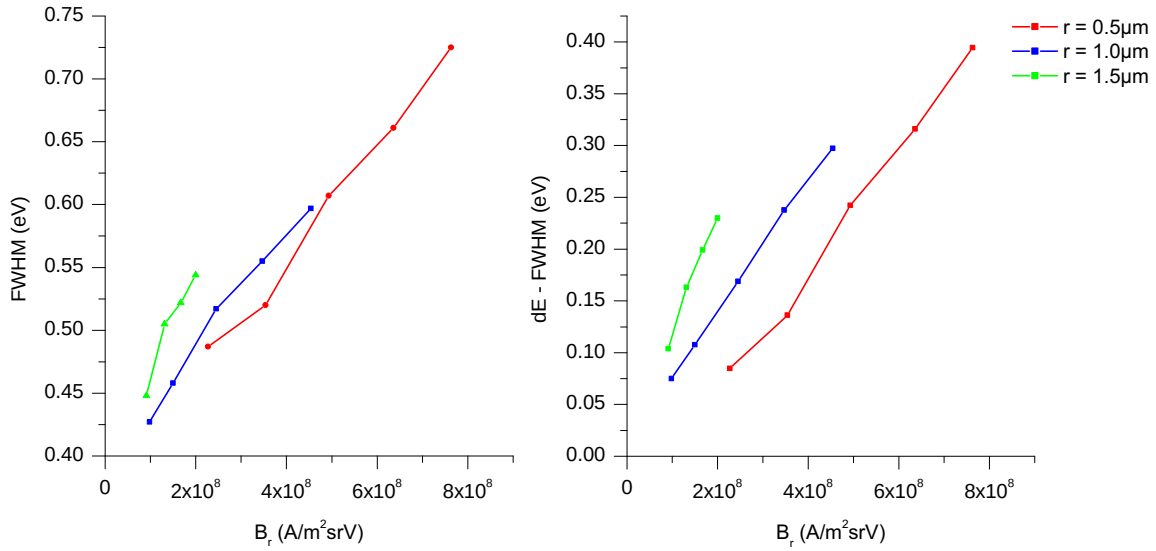

Figure 52: The energy width E and energy broadening dE measured in the screen plane at $z = 1$mm as a function of the reduced brightness B_r.

Table 2: Calculated operating parameters for the emitter radius 0.5μm.

I' $(\mu A/sr)$	F_{axial} (V/nm)	j (A/m^2)	U_{ex} (V)	$FWHM$ (eV)	$\Delta FWHM$ (eV)	d_{sim} (nm)	B_r (A/m^2srV)
59	0.456	1.20×10^7	2300	0.487	0.085	11.66	2.27×10^8
99	0.563	2.27×10^7	2740	0.520	0.136	11.32	3.54×10^8
198	0.697	4.72×10^7	3290	0.607	0.242	12.47	4.93×10^8
292	0.766	6.73×10^7	3570	0.661	0.316	12.49	6.36×10^8
378	0.827	9.13×10^7	3820	0.725	0.394	12.54	7.63×10^8

Table 3: Calculated operating parameters for the emitter radius 1.0μm.

I' ($\mu A/sr$)	F_{axial} (V/nm)	j (A/m^2)	U_{ex} (V)	$FWHM$ (eV)	$\Delta FWHM$ (eV)	d_{sim} (nm)	B_r (A/m^2srV)
59	0.284	3.73×10^6	2440	0.427	0.075	17.66	9.84×10^7
105	0.366	6.72×10^6	3020	0.458	0.108	17.18	1.50×10^8
202	0.474	1.34×10^7	3870	0.517	0.169	16.48	2.45×10^8
301	0.543	2.02×10^7	4270	0.555	0.238	16.08	3.47×10^8
424	0.598	2.76×10^7	4660	0.597	0.297	15.97	4.54×10^8

Table 4: Calculated operating parameters for the emitter radius 1.5μm.

I' ($\mu A/sr$)	F_{axial} (V/nm)	j (A/m^2)	U_{ex} (V)	$FWHM$ (eV)	$\Delta FWHM$ (eV)	d_{sim} (nm)	B_r (A/m^2srV)
53	0.185	1.63×10^6	2200	-	-	-	-
105	0.269	3.31×10^6	3000	0.448	0.104	22.08	9.14×10^7
212	0.373	7.05×10^6	4000	0.505	0.163	22.73	1.31×10^8
290	0.426	9.93×10^6	4500	0.522	0.199	22.17	1.67×10^8
376	0.470	1.31×10^7	4920	0.544	0.23	22.07	2.00×10^8

5.2 The CFE emitter

All parameters of the cold field emission model and simulated working points are described in section 4.3.1. Just to recall the most important parameters and working points: The simulations were performed for tip radii 50, 100 and 200nm and six angular intensity values in the range of 25 to 300μA/sr. Several screen planes were set along the z-axis behind the tip. The last screen plane was set to $z = 1$mm, i.e. to the plane of the extractor.

The results are not compared to the experimental data, because of major differences in the electron-optical configuration.

5.2.1 Angular intensity and half-opening angle

Analogous to the Schottky emitter, the dependence of the angular intensity on the potential of the extractor electrode was determined iteratively in the simulation. The Figure 53 shows plots calculated for all three tip radii covering the range of 25 to 300μA/sr.

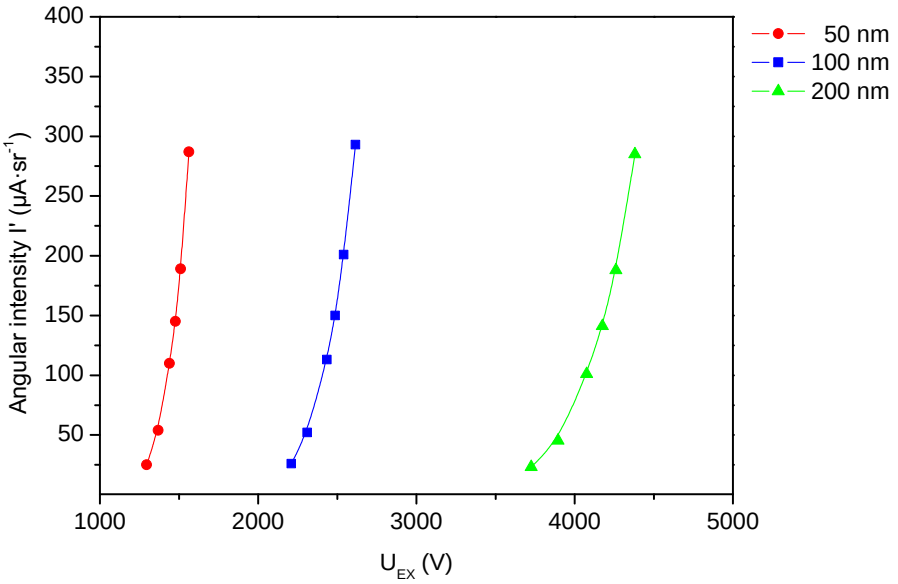

Figure 53: The dependence of the angular intensity on the potential at the extractor electrode for all three radii of the CFE emitter.

The mechanism of the field emission is more sensitive to the extraction field and to the tip radius. The angular intensity increases rapidly with a moderate change of the extractor voltage. The absence of the suppressor lens results in low potential levels needed for the operation of emitters with smaller radius. Missing faceting of the emitter tip results in a relatively stable intensity across the beam diameter. An example of several angular intensity plots for the emitter tip with radius 200nm is shown in Figure 54. The maximal half angle of the beam reaches 6°. The selection of the acceptance angle for the analysis was limited mainly by the dependence of the virtual source size on the half-opening angle. We chose a constant angle of 1.2° for all simulated tip radii and working points. Above this value the virtual source starts to grow, as will be shown in section 5.2.3.

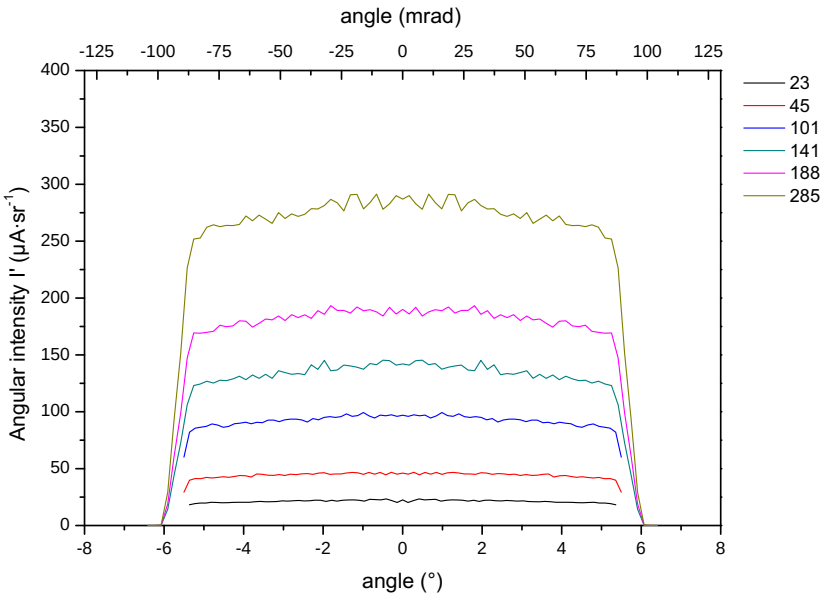

Figure 54: The dependence of the angular intensity on the distance from the axis defined by the varying half-opening angle in the screen plane $z = 1mm$ for the emitter with radius $1\mu m$.

5.2.2 The initial and total energy spread

Due to negligible differences of the electrostatic field across the emission surface there is no significant variance between the energy width of axial and all other emitted electrons. The energy spread of particles ray-traced without the calculation of interaction effects is thus equal to the initial energy width. Figure 55 shows an example of the evolution of the

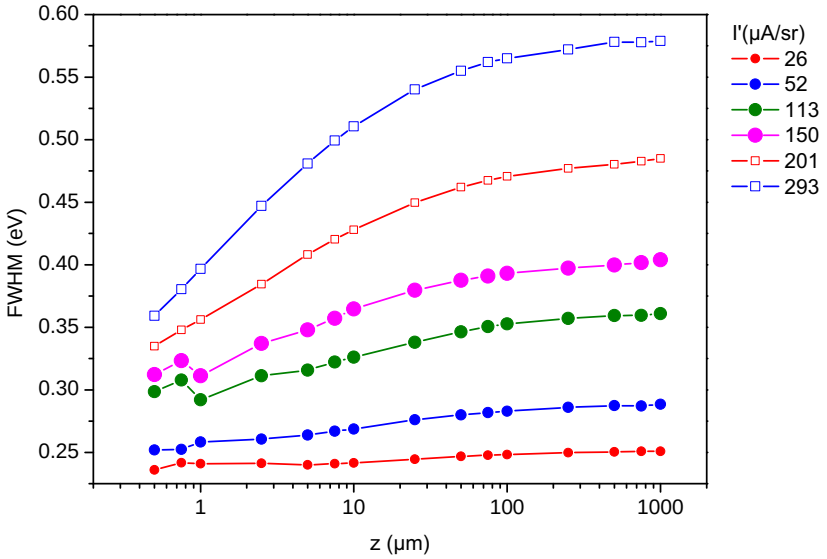

Figure 55: Example of the evolution of the energy width for the tip with radius 200nm with calculation of coulomb interactions.

energy width along the z-axis for the emitter with tip radius of 200nm. It is very similar to the evolution calculated for the Schottky emitter. Also in this case the most of the energy broadening took place in the first 50μm and all simulated working points show an increase in the energy width. The evolution is similar for all three tip radii. In comparison with the Schottky emitter the cold field emitter is usually operated at lower angular intensity values. The reason is mainly the relatively fast increase of the energy width at higher angular intensity. In dependence on the tip radius the energy spread above $I' = 150\mu$A/sr reach values, which are typical for the Schottky emitter. The relatively low I', usually in the range of 25–50μA/sr, does not present a problem for standard applications, because the probe current is still sufficient due to considerably higher brightness of CFE. The optimal working point is always a trade-off between the required current in the beam and the desired energy spread. The dependence of the total energy width on the angular intensity is shown in Figure 56.

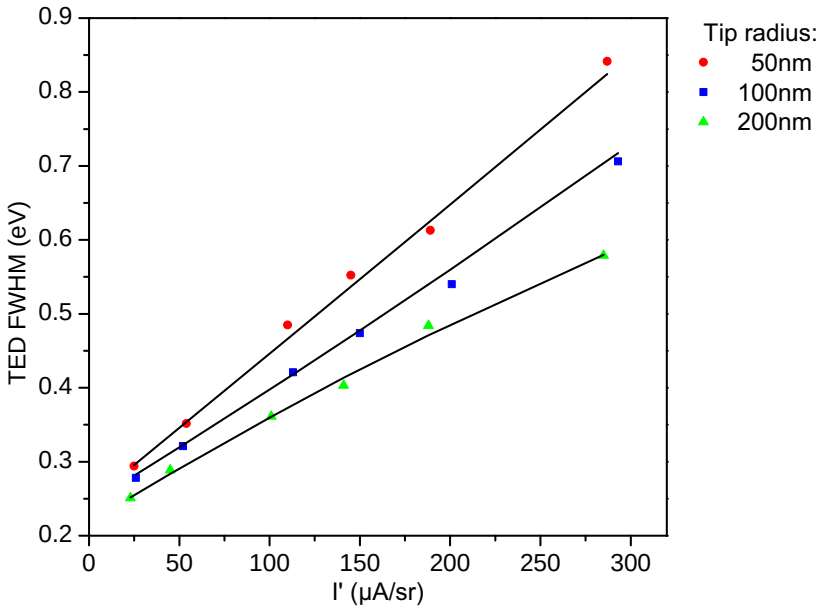

Figure 56: The dependence of FWHM TED on the angular intensity.

The emitter with the smallest tip has the highest energy spread. The increase of the TED is almost linear. A comparison of our simulation results in Figure 56 with published experimental data [16] does not have much sense due to significant differences between the real emitter and the analytical emitter model.

The contribution of the Boersch effect was calculated from the differences in the energy of individual particles, which were ray-traced with and without the calculation of the mutual interactions. The FWHM energy broadening dE(Boersch) versus I' is shown in left part of Figure 57. The right part of the figure shows the dependence of dE(Boersch) on the axial current density for all three tip radii.

The graphs in both parts show an outcome similar to the result from the case of the Schottky emitter. Although the emitter with 200nm tip radius has lower TED and dE values than the emitter with the smaller tip at particular I', the large tip suffers more from the interactions effects at the same current density level.

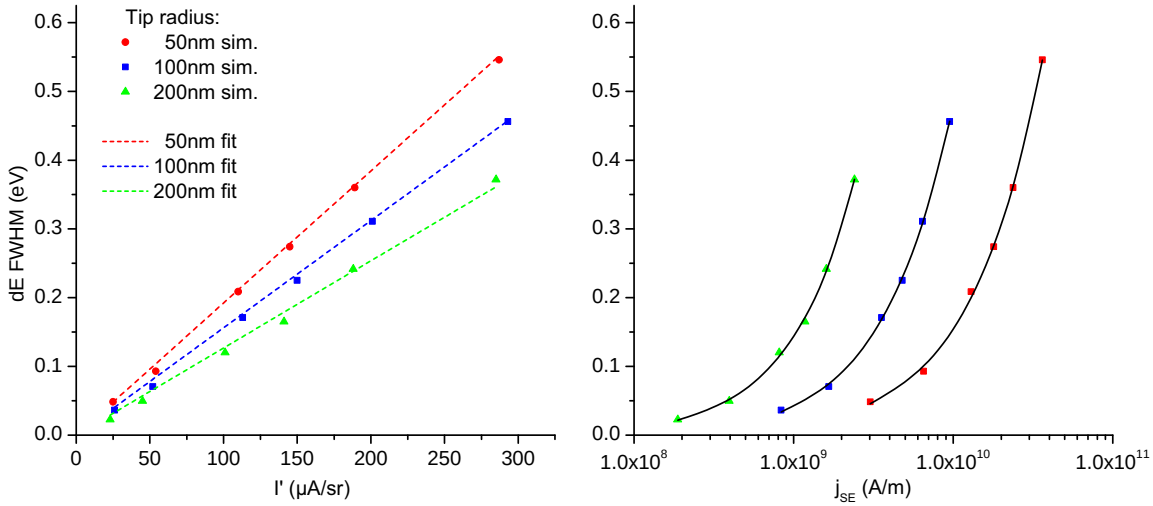

Figure 57: The dependence of dE Boersch (FWHM) on the angular intensity (left) and on the calculated axial emission current density (right).

We attempted to compare our simulation results with energy broadening values predicted by equations (37)–(40). Unfortunately, we did not find a satisfactory agreement with any of those equations (i.e. with particular beam regime) or their convolution. The predicted values followed distinctively different trends and a meaningful comparison was not possible. Similar to the Schottky emitter, the energy broadening contribution can be fitted to a simple power law function. The form of the function is equal to eq. (68). The fit was successful and a linear dependence of FWHM dE(Boersch) was obtained on following function:

$$\text{FW50 dE(Boersch)} \propto I' / r^{0.3}. \tag{70}$$

The dependence and the linear fit are shown in Figure 58.

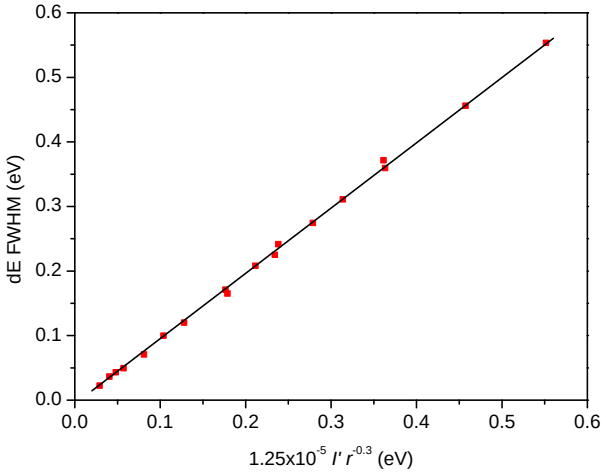

Figure 58: The Boersch FWHM versus the power function 70 shows a linear dependence..

5.2.3 The emitter brightness and the virtual source size

The next step was the evaluation of the effect of the interactions on the virtual source size d_v. The calculation was performed using the same measure (FW50) and procedure like in the case of the Schottky emitter. For the correct analysis it was necessary to determine an optimal half-opening angle α. We calculated the dependence of d_v on several values α for all three tip radii and a few angular intensity values. From the dependence we determined constant $\alpha = 1.2°$ for all working points. An example of the dependence is shown in Figure 59

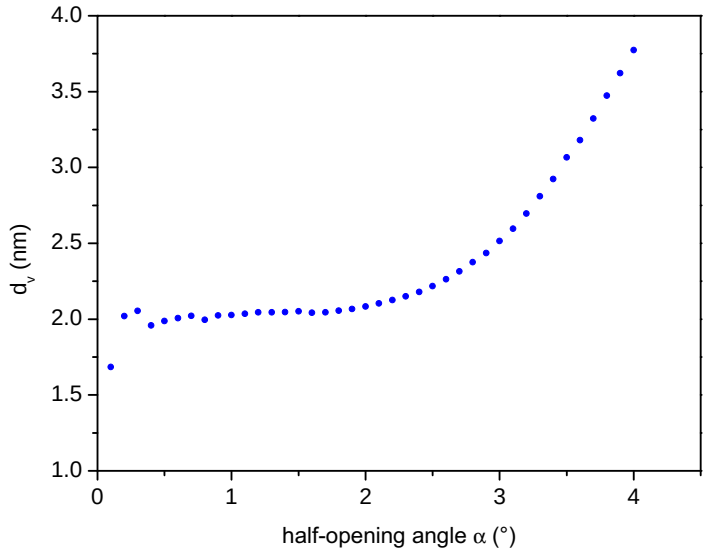

Figure 59: The virtual source size grows with increasing the half-opening angle. The data are related to the emitter with radius $r = 100$nm and $I' = 50\mu$A/sr. For small α the plot is noisy because of low number of particles in the analyzed beam. The section between 0.7°and 1.6°shows almost stabilized values of d_v. The half-opening angle α is selected here. Above $\alpha = 1.6°$ grows the virtual source size quickly.

The evolution of d_v along the whole beam path was calculated from the particle positions recorded in individual screen planes. Figure 60 shows results of the simulations with and without calculation of mutual interactions for emitter with tip radius $r = 200$nm and several values of angular intensity I'.

The d_v of the beam, in which the mutual interactions were not calculated, is along the whole trajectory on a downward trend. It starts with values, which are given by the combination of the emitter size and shape, the strength of the extraction field, the operational temperature and the size of the analyzed angle α. Especially the significantly lower tip radius r of the cold field emitter is responsible for distinctively smaller d_v in comparison with the Schottky emitter. The tangential energy of emitted electrons of CFE is significantly lower due to low operational temperature and the higher extraction field at the surface. This reduces d_v, as well. With the increased distance from the tip the d_v is further lowered by the effect of the strong acceleration field. In general, the virtual source size decreases with the increasing extraction voltage. If the interaction effects are included, d_v is strongly affected already after few micrometers. According to the simulation results the size of the virtual

source is in dependence on the emitter radius and the extractor voltage up to 20 times higher. Figure 61 shows calculated d_v versus I' for all three tip radii.

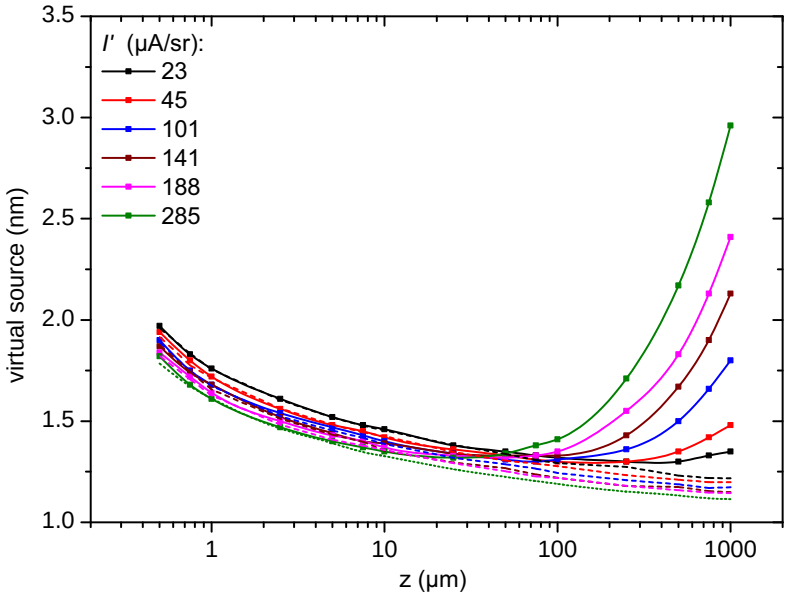

Figure 60: Example of evolution of the virtual source size along the z-axis for the emitter with $r = 200$nm and several I' values. The dashed lines are results from the simulation performed without the calculation of the interaction effects.

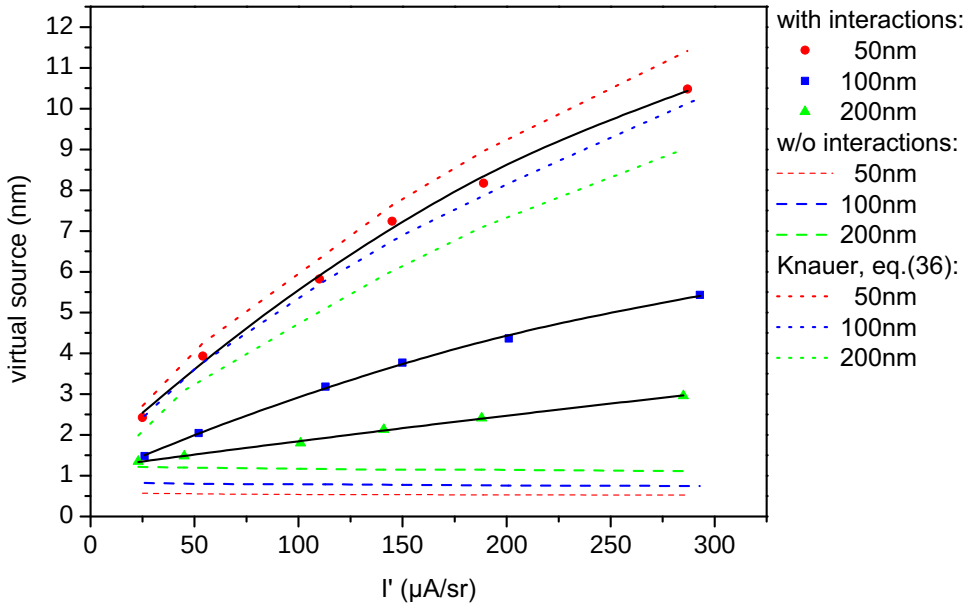

Figure 61: The calculated virtual source size d_v versus angular intensity I'. The dashed lines are values calculated without the interaction effects. The dotted lines represent values obtained from eq. (36)

The lateral broadening is more pronounced for emitters with smaller tip radius. The

dotted lines in Fig. 61 are d_v values predicted by Knauer's eq. (36). The formula shows low sensitivity to the tip radius and the extraction voltage. The trend of the predicted values is in general in a good agreement with the simulation result of the emitter with r =50nm, but the absolute values do not fit.

In practice, such a small virtual source is hard to measure, apart from the fact, that d_v measured in a real optical system contains contributions of various aberrations, which have to be subtracted. In almost all related publications the virtual source size of the cold field emitter is calculated using eq. 26). The equation does not take into account the interaction effects. For our emitter model it gives values of d_v in the range of 1.7 – 3.6 nm. In comparison with relevant simulation results (i.e. d_v of the beam without calculated interaction effects) are these values approximately 3 times higher. The reason for this difference may be in a different potential distribution within the emitter area caused by the "wehnelt-like" form of the extractor electrode and the method of mirror charges.

Neither our simulation nor eq. (26) takes into account the effect of the extractor bore on the potential distribution near the extractor plane. In the case of the Schottky emitter, it has been shown that the effect on the virtual source size is significant (see Fig. 48).

Knowing the virtual source size, the reduced brightness B_r can be calculated using eq.(30). The B_r is indirect proportional to d_v. If d_v is by virtue of lateral interaction effects enlarged, the value of B_r is accordingly reduced. Figure 62 shows the impact of the mutual interactions on the reduced brightness.

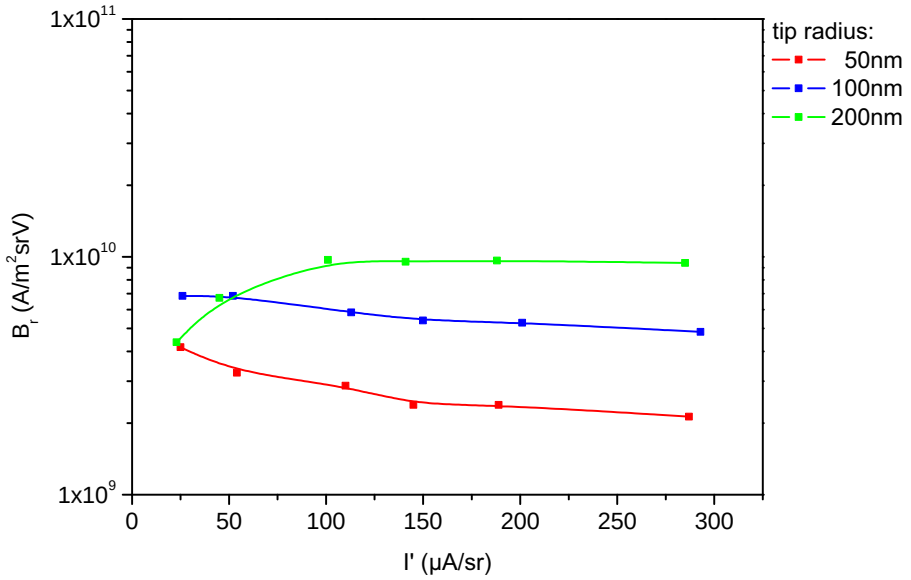

Figure 62: .

The case without coulomb interactions: The smaller tip has also the smallest d_v, which results in the higher reduced brightness B_r. The size of the virtual source is reduced with the increased extractor voltage, i.e. the B_r grows with the increased angular intensity. However, such a case is not realistic. According to our simulation results, the effect of the lateral broadening on the virtual source is relatively strong, especially for emitters with smaller tip

radii. The virtual source of the smaller emitter is significantly more affected by interaction effects and the calculated brightness is accordingly lower. The emitter with 50 and 100nm tip radius show also a continuous degradation of B_r with increasing I'. The 200nm tip has a different trend at lower intensity values. At lower emission currents is the growth of I' apparently slower than the broadening of d_v and the brightness increases. This trend breaks at $I' = 100\mu$A/sr. We must not forget the requirement of the low energy width. The dependence of TED (FWHM) on the reduced brightness is shown in Figure 63

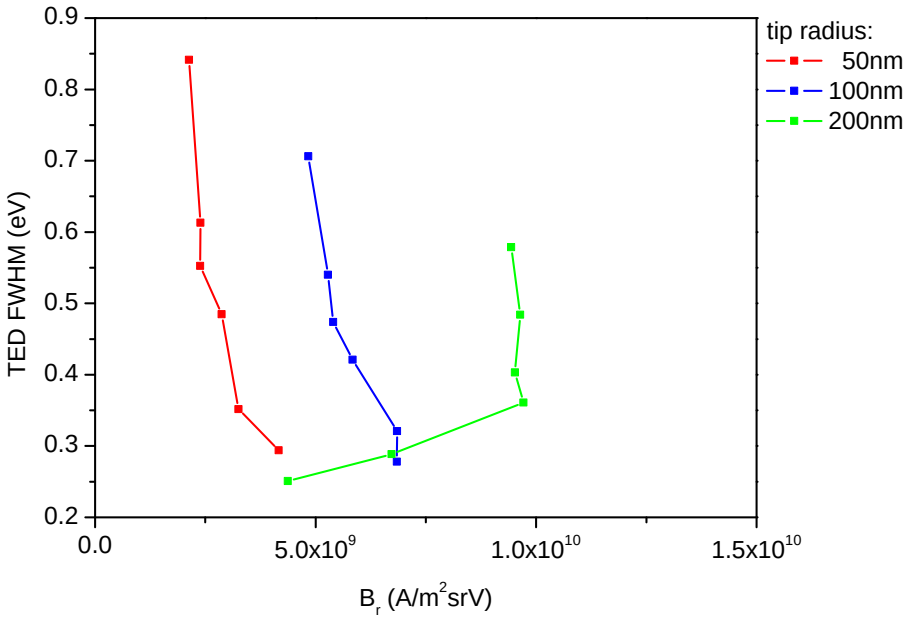

Figure 63: The total energy width versus the reduced brightness.

If the low energy spread should be preserved, the emitter should be operated at $I' \leq < 150\mu$A/sr and a tip with possibly large radius should be used. Larger radius also decreases the degradation of the virtual source by the coulomb interactions. On the other hand side, it increases the intrinsic virtual source and thus some care has to be taken in order to optimize the emitter parameters to the particular need. For practical reasons, the virtual source size below approximately 5nm is difficult to work with due to the limitations caused by the aberrations of the electron lenses. Thus the increase of the virtual source size due to larger emitter radius in majority of cases does not present practical limitations.

6 Conclusion

The aim of the thesis was to prepare and perform simulation of the coulomb interaction effects in the vicinity of the field electron emitter tip using ray tracing and Monte Carlo methods. The target was to avoid simplifications or analytical approximations and thus receive results with unprecedented accuracy and reliability. Because for such a complex task no ready-to-use software exists, several specialized tools and routines have been created.

A new method for generating initial particle conditions has been developed, which respects in more detail than usually the physical emission process. A potential barrier model was introduced into the simulation of the emission process. For particles, which are tunneling through the potential barrier, the longitudinal starting positions of electrons are determined by their initial energy and the thickness of the barrier, as seen by the particle at particular energy level. Also the other initial data were generated using realistic models. The initial angular distribution takes into account the effects of the strong surface field. The flat facet at the tip apex, typical for the Schottky emitter, was implemented. The local changes in the electrostatic field at the facet were reflected in the emission current density distribution. It has been shown that the direct effect of the facet on the initial energy width is small. However the stronger emission from the facet edge significantly contributes to the coulomb interactions.

The ray tracing was performed by the Runge-Kutta method of 5-th order with adaptive step. In each sub-step of the RK the local field was calculated including all mutual interactions. The electron-electron interactions were calculated directly without approximation for each particle pair in the system.

The accuracy of the developed tools has been tested on the analytical model of the field distribution of the emitter - extractor configuration [2]. On this model the correct functioning of all software components has been verified and adjustment of the parameters influencing accuracy has been made. Only then the simulations on the accurate numerical field model obtained by the finite element method have been started.

The investigation concentrates on the Schottky emitter in the standard suppressor - extractor configuration. The ray-tracing of the particles was performed for three tip radii and several angular intensity values, in order to cover the typical range of operational parameters. In addition simulations were done also for cold field emitter for the set of different tip radii and angular intensities. However due to the lack of the time this simulations have been done only on the analytical field distribution model and the results can be used only for judgment of the qualitative trends not for absolute accuracy.

Some of the results were similar for both emitters: The evolution of the energy width in the emitter region showed that the absolute majority of interactions take place within first 50μm, hence the effect of interactions cannot be significantly lowered by a change of the position of the extractor. It has been shown that the magnitude of the coulomb interactions depends practically only on two parameters - on the angular intensity and on the tip radius. The dependence has a character of the power law for both parameters. The effect is proportional to the certain power of the angular intensity and inversely proportional to the power of the radius. The power coefficients depend on the particular emitter type and probably also on the geometrical parameters of the suppressor - tip - extractor configuration. However they stay within a relatively narrow range.

If not angular intensity but brightness of the emitter is parameter of the interest the character of the dependence on the emitter radius changes. For constant brightness one can get better results (less Boersch energy broadening) using emitter with smaller radius. This is because of the strong implicit dependence of the brightness on the virtual source size and thus on the emitter radius.

The dependence of the calculated total energy width on the angular intensity was compared to available experimental data, showing a good agreement. Small differences observed at low angular intensity values in the measurements done by Sakawa [5] might indicate an inaccuracy of the initial energy spread predicted by the theory of the emission. Certain role can play also limitation of the accuracy of the experimental energy spread measurement. Even better agreement can be seen on the comparison with the experimental data obtained by Schwind et al.[11]. They did measurements for broad range of emitter radii and angular intensity. They concluded a power law dependence between the Boersch effect, angular intensity and emitter radius with power coefficients similar to our results. The residual differences in the coefficients can be caused by difficult extraction of the pure Boersch energy broadening from the measured total energy distribution.

The calculated contribution of the interaction effects to the energy width was compared with predictions based on analytical approximations. It has been shown that the Knauer's formula (eq.(35)) strongly overestimates the Boersch effect and therefore is not suitable for the evaluation in similar cases. The equation (67) derived by Jansen and Kruit [1] and modified by Fransen [10] predict reasonably the tendencies, however cannot be used for quantitative estimations. Following the classification of beams introduced by Jansen [24] the beam of the Schottky emitter in the simulated range of emission currents corresponds to the Holtsmark regime.

For the cold field emitter there are no reliable published data on the energy spread. According to our results the energy broadening follows similar power law as in the case of the Schottky emitter. The effect is stronger due to the smaller emitter radius and thus higher current density in the vicinity of the tip. On contrary to the Schottky emitter, the virtual source is also significantly affected by the coulomb interactions. This is due to the very small intrinsic virtual source for the typical cold field emitter. Already at moderate angular intensities the virtual source can be dominated by coulomb interactions. This is especially true for the emitter with very small radius (50nm) where the intrinsic virtual source is in the 1nm range. This can lead to the effect where the brightness reduces with increasing angular intensity due to over proportional increase of the virtual source.

References

[1] KRUIT, P. - JANSEN, G.H. Space Charge and Statistical Coulomb Effects. In *Handbook of charged particle optics*. Edited by John Orloff. New York: CRC Press LLC, 1997. 512 p. ISBN 0-8493-2513-7.

[2] HAWKES, P.W. - KASPER, E. *Principles of Electron Optics*. vol. II, New York: Academic Press, 1989. 1188 p. ISBN 0-12-333352-0.

[3] BRONSGEEST, M.S. - BARTH, J.E. - SCHWIND, G.A. - SWANSON, L.W. - KRUIT, P. Extracting the Boersch effect contribution from experimental energy spread measurements of Schottky electron emitters. *J. Vac. Sci. Technol. B*, November 2007, vol. 25, no. 6, pp.2049-2054. ISSN 1071-1023

[4] RADLIČKA, T. - LENCOVÁ, B. Coulomb interactions in Ga LMIS. *Ultramicroscopy*, 2007, vol. 108, no. 5, pp.445-454. ISSN 0304-3991.

[5] SAKAWA, S. - TSUNODA, K. - TERUI, Y. Electron emission characteristics of ZrO/W electron sources with a wide range of tip radii. *Surface and Interface Analysis*, January 2003, vol. 35, issue 1, pp.11-14. ISSN 0142-2421

[6] SWANSON, L.W. - MARTIN, N.A. Field electron cathode stability studies: Zirconium/tungsten thermal-field cathode. *Journal of Applied Physics*, May 1975, vol. 46, issue 5, pp.2029-2050. ISSN 0021-8979

[7] TUGGLE, D.W. - SWANSON, L.W. Emission characteristics of ZrO/W thermal field electron source. *J. Vac. Sci. Technol. B*, Jan/Feb 1985, vol. 3, no. 1, pp.220-223. ISSN 1071-1023

[8] SWANSON, L.W. - SCHWIND, G.A. A review of the Cold-Field Electron Cathode. In. *Advances in Imaging and Electron Physics*. Academic Press, Vol.159, November 2009, pp.63-100. ISSN 1076-5670

[9] BRONSGEEST, M.S. - BARTH, G.A. - SWANSON, L.W. - KRUIT, P. Probe current, probe size and the practical brightness for probe forming systems. *J. Vac. Sci. Technol. B*, May/June 2008, vol. 26, no. 3, pp.949-955. ISSN 1071-1023

[10] FRANSEN, M.J. - FABER, J.S. - VAN ROOY, T.L. - TIEMEIER, P.C. - OVERWIJK, M.H.F - FABER, J.S. - KRUIT, P. On the Electron-Optical Properties of the ZrO/W Schottky Electron Emitter. In. *Advances in Imaging and Electron Physics*. Academic Press, Vol.111, September 1999, 372 p. ISBN 0-12-014753-X

[11] SWANSON, L.W. - SCHWIND, G.A. Review Of Zr/O Schottky Cathode. In *Handbook of charged particle optics, 2nd ed.*. Edited by John Orloff. New York: CRC Press LLC, 2009. 665 p. ISBN 978-1-4200-45543

[12] KIM, H.S. - YU, M.L. - THOMSON, M.G.R - KRATSCHMER, E. - CHANG, T.H.P. Energy distributions of Zr/O/W Schottky electron emission. *J. Vac. Sci. Technol. B*, January 1997, vol. 81, no. 1, pp.461-465. ISSN 1071-1023

[13] ADAMEC, P. - LIŠKA, I. - GLUCHMAN, G. - ŠNÁBL, M. Arrangement for the pretreatment of the electron gun vacuum chamber. European patent application 09172942.6 - 2208. 13 Oct. 2009.

[14] BELL, A.E. - SWANSON, L.W. Total energy distribution of field emitted electrons at high current density. *Phys. Rev. B*, April 1979, vol. 19, no. 7, pp.3353-3364. DOI:10.1103/PhysRevB.19.3353

[15] BECK, S. *Niederenergie-Hochstrom-Elektronensonde mit Feldemissionskathode, Wienfiltern und Immersionsobjektivlinse* PhD Thesis. Tübingen: Eberhard-Karls-Universität zu Tübingen, 1994. 122 p.

[16] SCHWIND, G.A. - MAGERA, G. - SWANSON, L.W. Comparison of parameters for Schottky and cold field emission sources. *J. Vac. Sci. Technol. B*, Nov/Dec 2006, vol. 24, no. 6, pp.2897-2901. ISSN 1071-1023

[17] OHSHIMA, T. - NISHIYAMA, T. Study of energy distribution of Schottky emitted electrons and its theoretical analysis using effective mass approximation. *Jpn. J. Appl. Phys.*, October 2003, vol. 42, no. 10, part 1, pp.6564-6568. DOI:10.1143/JJAP.42.6564

[18] REIMER, L. *Scanning Electron Microscopy, Physics of Image Formation and Microanalysis*. 2^{nd} edition, Berlin: Springer, 1998. 527 p. ISBN 3-540-63976-4

[19] GOOD, R.H. - MÜLLER, E.W. Field Emission. In *Handbuch der Physik*. Edited by S. Flügge. Band 21. Berlin: Springer-Verlag, 1956. 683 p. ISBN 978-3-540-06638-5

[20] FORBES, R.G. Simple good approximations for the special elliptic functions in standard Fowler-Nordheim tunneling theory for a Schottky-Nordheim Barrier. *Appl. Phys. Lett.*, 2006, vol.89, no. 113122. DOI:10.1063/1.2354582

[21] ZIMMERMANN, B. *Advances in Electronics and Electron Physics*, New York: Academic, 1970, vol.29, p.257. ISSN 0065-2539

[22] KNAUER, W. Energy Broadening in Field emitted Electron and Ion Beams. *Optik*, 1981, vol. 59, issue 4, pp.335-354. ISSN 0030-4026

[23] LOEFFLER, K.H. Energy Spread Generation in Electron-Optical Instruments. *Zeitschr. Angew. Phys.*, 1969, vol.27, p.257.

[24] JANSEN, G.H. Coulomb Interactions in Particle Beams. In *Advances in Electronics and Electron Physics, Suppl.21* Academic Press, 1990. 546 p. ISBN 0-12-014583-9

[25] JIANG, X.R. *Coulomb interactions in charged particle optical columns.* PhD Thesis. Delft: Delft University of Technology, 1996. 156 p. ISBN 90-407-1369-3

[26] Munro's Electron Beam Software Ltd. [online]. last modified 13 February 2008. [cit. 2004-04-20]. URL:<http://www.mebs.co.uk/>

[27] CPO Ltd.: Help for CPO Programs. CPO Ltd, UK, Feb 2001, Version 3.1e. URL:<http://www.electronoptics.com/>.

[28] LENCOVÁ, B. - ZLÁMAL, J. The Development of EOD Program for the Design of Electron-Optical Devices. *Microscopy and Microanalysis*, 2007, vol. 13, suppl. 3, pp. 2-3. ISSS 1431-9276

[29] MUNRO, E. Computational Techniques for Design of Charged Particle Optical Systems. In *Handbook of charged particle optics*. Edited by John Orloff. New York: CRC Press LLC, 1997. 512 p. ISBN 0-8493-2513-7.

[30] Caneval BV - Montec.: Manual for MONTEC and INTERAC. Caneval BV, Netherlands, Jan 2004, Version 1.7.
URL:<http://www.caneval.com/montec/downloads/MonTec_Manuals.pdf>.

[31] CASH, J.R. - KARP, A.H. A variable order Runge-Kutta method for initial value problems with rapidly varying right-hand sides. *ACM Transactions on Mathematical Software*, September 1990, vol. 16, issue 3, pp.201-222. ISSN:0098-3500

[32] EL-KAREH, A.B. - WOLFE, J.C. - WOLFE J.E. Contribution to the general analysis of field emission *J.Appl.Phys.*, November 1977, vol. 48, issue 11, pp.4749-4753. ISSN 0021-8979

[33] JANSEN, G.H. - GROVES, T.R. - STICKEL, W. Energy broadening in electron beams: A comparison of existing theories and Monte Carlo simulations. *J. Vac. Sci. Technol. B*, Jan/Feb 1985, vol. 3, no. 1, pp.190-193. ISSN ISSN 0734-211X

[34] ELSWIJK, H.B. - VAN ROOY, T. - SCHILLER, C. Energy broadening by Coulomb interactions of an electron beam emitted from a point source. *J. Vac. Sci. Technol. B*, May/Jun 1995, vol. 13, no. 3, pp.1037-1043. ISSN 1071-1023

[35] SHIMOYAMA, H. - SHIMAZAKI, Y. - TANAKA, A. Computer simulation of energetic Boersch effect in the diode region of the field emission gun. In *SPIE - Charged Particle Optics*, September 1993, vol. 2014, pp.99-103. ISBN 0-8194-1263-5

[36] THOMSON, M.G.R. Electron-electron scattering in microcolumns. *J. Vac. Sci. Technol. B*, Nov/Dec 1994, vol. 12, no. 6, pp.3498-3502. ISSN 0734-211X

[37] READ, F.H. - BOWRING, N.J. Monte Carlo calculation of Boersch energy spreading. *Nuclear Instruments and Methods in Physics Research Section A - Accelerators Spectrometers Detectors and Associated Equipment*, February 21. 2004, vol.519, issue 1-2, pp.196-204. ISSN 0168-9002

[38] LIŠKA, I. - ADAMEC, P. - LENCOVÁ, B. Coulombovské interakce elektronů v blízkosti Schottkyho katody. *Jemná mechanika a optika*, Nov/Dec 2009, vol. 54, no. 11-12, pp.315-317. ISSN 0447-6441

[39] FUJITA, S. - SHIMOYAMA, H. Thermal-field treatment for creating single-crystal tungsten tips with ultimate sharpness. *J. Vac. Sci. Technol. B*, Mar/Apr 2008, vol. 26, no. 2, pp.738-744. ISSN 1071-1023

[40] SASAKI, T. Upper bound of the beam energy broadening in acceleration region. *J. Vac. Sci. Technol. B*, Jan/Feb 1986, vol. 4, no. 1, pp.135-139. ISSN 1071-1023

[41] WIESNER, J.C. - EVERHART, T.E. Point-cathode electron sources - electron optics of the initial diode region. *J. Appl. Phys*, May 1974, vol.44, no. 5, pp.2140-2148. ISSN 0021-8979